Bottom-up design of calcium channels from selectivity filters

Yulai Liu

A dissertation

submitted in partial fulfillment of the

requirements for the degree of

Doctor of Philosophy

University of Washington

2024

Reading Committee:

David Baker, Chair

Frank DiMaio

Tamer M. Gamal El-Din

Program authorized to Offer Degree:

Molecular Engineering

University of Washington

Abstract

Bottom-up design of calcium channels from selectivity filters

Yulai Liu

Chair of the Supervisory Committee:

David Baker

Department of Biochemistry

Native ion channels play key roles in biological systems, and engineered versions are widely used as chemogenetic tools and in sensing devices. Protein design has been harnessed to generate pore-containing transmembrane proteins, but the capability to design ion selectivity based on the interactions between ions and selectivity filter residues has been constrained by the lack of methods to place the metal-coordinating residues with atomic-level precision. Here we develop a bottom-up approach to construct Ca^{2+} channels from selectivity filters with different coordination numbers and different geometries. Patch-clamp experiments show that the designed channels have higher conductance for Ca^{2+} than for Na^{+} and other divalent ions (Sr^{2+} and Mg^{2+}). Cryo-electron microscopy shows that the structure of a designed Ca^{2+} channel is nearly identical to the design model. Our bottom-up design approach now enables the testing of hypotheses relating filter geometry to ion selectivity and provides a roadmap for creating selective ion channels for a wide range of applications.

Table of Contents

1. Background and motivation

Ion channels play key roles in biological systems. Engineered versions of these ion-permeable proteins are widely used as chemogenetic tools and in sensing devices[1,2]. An essential property of ion channels is their ability to selectively transport specific ions. The origin of the ion selectivity of natural channels has been of great interest since the characterization of the first native channels. It is generally accepted that ion selectivity is achieved as the effects of both the physical dimensions of the pore (pore radius versus ion radius) and the chemical processes (hydration/dehydration of the ions and the ion-channel interactions) enabled by the pore-lining atoms of ion channels. However, experimental approaches for investigating the molecular basis for the selectivity of ion channels to date have been limited to examining the effects of amino acid substitutions[3–8] or domain grafting among homologs that creates channel chimeras[9–11]. Systematic probing of pore geometry and chemical identities of the pore-lining amino acids have not been achieved. This is probably due to the fact that native ion channels share similar protein architectures[12], especially the channels within a superfamily (for example, the P-loop superfamily[13] and the Cys-loop superfamily[14]), and their functions are well-tuned towards specific physiological functions by evolution, both resulting in limited extent to which traditional protein engineering (mutagenesis approach) can be used to systematically investigate how the arrangement of selectivity filter residues affects ion permeation and selectivity of ion channels.

A fundamental way to overcome this limitation is to design ion channels from scratch. *De novo* protein design provides a much wider sampling space both in protein structure and protein sequence[15], enabling a combinatorial exploration of physical arrangements of selectivity filter residues and amino acid identities in the way that is not constrained by the protein fold of native ion channels. *De novo* designed proteins tend to be very stable (e.g., they usually remain folded at 95 °C whereas most natural proteins unfold at such a high temperature[16]), enabling these proteins to tolerate extensive modifications. Progress has been made in *de novo* design of pore-containing transmembrane proteins and channels, including assembly of synthetic peptides into barrels[17–21], conversion of water-soluble helical bundles into transmembrane pores[22,23], and the design of transmembrane β-barrels from 2D blueprints[24,25]. However, these approaches do not enable precisely placing ion-interacting residues along the ion permeation pathway at angstrom level, and hence designed conducting channels to date have had little ion selectivity. By contrast, the interaction between ions and selectivity filter residues is a crucial feature of native ion channels to achieve ion selectivity[26]. This limitation is particularly significant in the context of designing a Ca^{2+} channel since Ca^{2+} has a nearly identical bare ion radius (~1 Å) compared to Na^{+} and a hydrated ion radius (~4 Å) similar to Mg^{2+} [27–29]. Native Ca^{2+} channels utilize carboxylate groups to bind Ca^{2+} ions with high affinity, potentially in a partially dehydrated manner contingent on the geometry of the carboxylate groups[4,30–34], which prevents permeation of other ions. Such stringent requirements on the geometry of the selectivity filter are not readily achievable using previous design methods, for which the positions of pore-lining residues are largely determined by the protein folds.

Despite the diverse mechanisms of how channels are regulated and gated by various molecules, the architecture of an ion channel can be simply viewed as protein domains wrapping around an ion-permeating pore. Inside the pore ions briefly interact with the pore-lining residues in the narrowest constriction, usually polar or charged, overcome the energetic barrier to squeeze through the narrow constriction, and quickly travel through the pore across the lipid membrane just like water flowing through the tubing. With the above scenario in mind, the pore domain of an ion channel can be viewed as comprising two important functional motifs: a selectivity filter to achieve selectivity, and a water-filled chamber/vestibule that facilitates regain of water shells around an ion for fast passage through the pore. Following this reasoning, the task of designing an ion channel can be treated as a motif-scaffolding problem – that is to create new proteins that scaffold these motifs into a protein fold, which resembles an enzyme design task. In fact, ion channel has also been described in terms of enzymology – ion channel catalyzes the reaction of ion transportation through the hydrophobic lipid bilayer membrane with a high "turnover rate (one picoampere is roughly 6 x 10^{6} electrons per second, which is equivalent to the V_{max} value for an enzyme[35])". The bottom-up construction of ion channels from specified motifs used to be a challenging design problem using previous design methods where helical bundles were parametrically generated beforehand based on Crick parameters.

For a given geometry of a ring of residues forming the selectivity filter, it is hard to find a corresponding Crick parameter to accommodate these residues without knowledge of backbone information of the filter motifs to be scaffolded. Modern deep learning-based protein design tools provide a solution for this task. RFdiffusion is capable of generating protein backbones from random noise around custom specified motifs in both single chain and symmetrical manners[36]. ProteinMPNN can design amino acid sequences on input protein backbones[37]. AlphaFold can predict if the protein sequence (primary structure) can fold into three dimensional structures as desired and return a confidence level of whether this prediction is trustable[38]. With a combinatorial utilization of these computational tools, it is possible nowadays to design ion channels with defined pore geometries.

The primary motivation for this study is to investigate the possibilities to construct ion channels from scratch with pre-defined selectivity filters and pore geometries as mentioned above, characterize the designed channels experimentally to verify the design approach, and study the new properties of these newly created ion channels – will they manifest similar properties as native ion channels regarding ion permeation? This would enable direct testing of hypotheses relating pore structure to conductance, a basic science question – a systematic study of the structural basis for ion selectivity of ion channels. We chose to focus on Ca^{2+} channels as the mechanism of Ca^{2+} selectivity is relatively well understood. With the hypothesis that the proper spatial arrangement of the carboxyl groups at the pore entrance followed by a wide and well-hydrated pore comprised of residues distant from the axis of the pore would confer both Ca^{2+} permeability and selectivity, we reasoned that Ca^{2+} channels could in principle be constructed by (1) generating the selectivity filter with systematically sampled geometric parameters, including distance and coordinations of protein sidechains to the Ca^{2+} ion, (2) scaffolding the selectivity filter onto helices defining the pore shape, and (3) buttressing the pore by multiple transmembrane helices. This procedure could in principle create channels with custom-defined selectivity filter geometry with angstrom-level precision, with the overall topology of the protein optimal for supporting the selectivity filter and conducting pore rather than being defined in advance.

A secondary motivation is to provide additional biological tools for biological studies, such as for chemogenetics and sensing applications[1,2,39,40]. Among all types of ion channels, Ca^{2+} channel is of great interest due to its ability to mediate influx of Ca^{2+} into the cells given the critical role of Ca^{2+} as a second messenger. Some specific G protein-coupled receptors (GPCRs) and ligand-gated ion channels have been engineered to study the downstream effects of Ca^{2+} influx upon administration of an agonist of those GPCRs or channels[1,41]. However, the agonists used for those studies tend to cross-interact with other subtypes of receptors or channels, and other side effects caused by activation of GPCRs or influx of other ions through the channels may also result in unintended outcomes. *De novo* designed Ca^{2+} channels will provide novel genetically encodable and biorthogonal tools for selectively introducing Ca^{2+} influx in specific cell types.

2. Methods

2.1. Computational methods: Backbone design

2.1.1. Generation of pore helices

The pore helices can be generated in three steps: (1) placement of Ca^{2+}-coordinating residues as the selectivity filter, (2) placement of pore exit residues, and (3) generation of protein backbones to hold these pore-defining residues.

In theory any structural element containing carboxylates and Ca^{2+} ions can be used to define the filter. We extracted the six Glu residues from the open-state structure of Orai channel as the template Ca^{2+}-coordinating motif to start from. The coordinates of the motif were changed simultaneously such that the motif was placed in the x-y plane with the Ca^{2+} ion on the Z-axis using PyMOL. Then five copies of the Glu/Asp residues were deleted, and the X and Y coordinates of the remaining Glu/Asp residue were sampled using PyRosetta through rigid-body moves to generate ion-residue pairs with different distances. These ion-residue pairs were symmetrized using the SetupForSymmetry

Mover in RosettaScripts with applied C4 or C6 symmetry to generate selectivity filters with different geometric parameters.

The pore exit residues were generated by positioning a set copy of the Ca^{2+}-coordinating residues at specific distances (h) along the Z-axis away from the original X-Y plane. This positioning was applied as rigid body transformation in Pyrosetta. The Z-distance between the two layers of residues defined the length of the pore. The ideal Z-distance was determined to be 43.2 Å in our case mainly based on three considerations: (1) the vertical distance between residue i and i+8 that have the same sidechain orientation (i.e., two consecutive helical turns) is 10.8 Å, (2) the membrane thickness in eukaryotic cells is usually greater than 30 Å[42,43], and (3) we want the pore helices to extend beyond the lipid bilayer, which can reduce the overall hydrophobicity of these helices, and in turn reduce the trend of protein aggregation and non-specific interhelical packing interactions driven by large patches of hydrophobic residues. So the pore length is determined to be 4 x 10.8 Å = 43.2 Å. At this stage the specific amino acid identities of the pore exit residues are inconsequential, as the sequence will be redesigned by ProteinMPNN[37] at a later sequence design step. The X and Y coordinates of these pore exit residues were sampled using the rigid body transformation function of Pyrosetta to generate pores with different geometries.

To form the lining of the pore, RFdiffusion[36] was used to symmetrically generate helices that connected the selectivity filter and pore exit residues. The number of the helical linker residues was sampled in order to generate straight alpha helices as the optimal secondary structure. Typically 25-29 residues were sufficient to position the pore entrance and exit residues on a straight helix, depending on the tilt angle of the pore helix relative to the Z-axis.

2.1.2. Generation of supporting protein backbones

Once the pore helices were obtained, RFdiffusion was subsequently used to symmetrically generate protein backbones for extending the pore helices into homo-oligomeric subunits with L residues in each monomer. The overall length of the monomer

(L) largely depends on the number of times it passes through the membrane and relative distances between neighboring chains. In particular, the number of residues before (at N-terminal of) and after (at C-terminal of) the pore helices were sampled to ensure adequate buttressing of protein backbones within each monomer and extensive interface areas between neighboring subunits. In general, we found that 30-40 residues were sufficient to form a straight single pass helix, and could be used as the repeating unit to estimate a rough range of the residue numbers needed to generate. The backbone outputs were examined by eye, and those with well-buttressed helices and open pores were selected for the subsequent protein sequence design.

We separated the processes of the generation of pore helices and the scaffolding of pore helices although both steps were done by RFdiffusion. This appeared to be more effective in guiding RFdiffusion to make more compact ion channel-like helical structures than only scaffolding the selectivity filter and pore exit residues. In the latter case, the output backbones mostly contained fiber-like helical coiled-coil assemblies extending far away from the selectivity filter.

2.1.3. Resampling and optimization of protein backbones

In some cases, very few designed sequences were predicted to fold with high confidences for some specific protein backbones with very tilted pore geometries. We hypothesized that the low in silico success rate was due to non-ideality of the protein backbones, which resulted in a low “designability” by ProteinMPNN. To refine the protein backbones, we applied partial noising and denoising processes using RFdiffusion partial diffusion to sample for more reasonable structures around the original backbone. This resampling process was not applied on the pore helices to maintain the pore geometry. The newly generated backbones were then subjected to another round of backbone selection, sequence design, and structural prediction as described above.

2.1.4. Connecting DHR to designed oligomeric channel for Cryo-EM analysis

To connect DHR proteins as the soluble domain to CalC6_3 for structural determination, the main objective is to avoid potential steric clashes between the subunits after addition of multiple copies of DHR proteins. This was achieved by precisely adjusting the relative position of the DHR proteins to CalC6_3, and this positioning operation was primarily done in PyMOL. The N-termini of experimentally-validated DHR proteins with different twisted geometries were aligned to the C-terminus of the CalC6-3 monomer and were oriented to face away from the pore. Then the DHRs were moved in the direction parallel to the aligned helix away from CalC6_3 to a point where the DHRs were unlikely to clash with the neighboring subunits. RFdiffusion was subsequently used to generate straight helices to fuse DHRs to the CalC6_3 monomer. The linked structure was symmetrized using the Rosetta SetupForSymmetry Mover by generating five extra copies. The residues that might potentially interact with neighboring subunits were manually selected and redesigned by ProteinMPNN as homo-hexamer. The sequence of the redesigned monomer was predicted by AlphaFold2[38] (the whole complex was too large for AlphaFold2 to predict). Designs with lowest Cα RMSDs to the CalC6_3 model in regard to the channel region were selected for experimental characterization.

2.2. Computational methods: Sequence design on protein backbones

The selected protein backbones of the channels were sequence-designed with ProteinMPNN. The --tied_positions argument was used to restrict sequences to be identical on each monomer. The residues forming the selectivity filter were kept undesigned using the --fixed_positions argument. Position-specific amino acid constraints were applied using the --omit_AAs argument. The pore-lining residues were selected based on the distance between the Cα atom of the residue and the central Z-axis (the square root of the sum of the squares of X and Y coordinates of that Cα atom in the PDB file). Charged and bulky aromatic amino acids (tyrosine and tryptophan) were excluded from the selected pore residues to prevent interference with ion permeation through the pore, particularly through sites that might form narrow constrictions. Residues that were defined as being embedded in the lipid bilayer were selected based on their relative vertical (Z) distances to the selectivity filter. The selectivity filter residues were arbitrarily designated as the initial point of the lipid bilayer on the extracellular side. Residues that are within a certain range on the Z-distance (e.g., 30 Å) were all defined to be embedded in the lipid bilayer. The lipid-facing residues were selected combinatorially by (1) the Rosetta LayerSelector using the sidechain neighbor algorithm, (2) not being among the pore-lining residues, and (3) being among the lipid-embedded residues. Tyrosine (Tyr) and tryptophan (Trp) residues were placed at the first and final residues of the surface residues on a consecutive helix, respectively, interfacing the aqueous phase and lipid phase.

It is optional to use the ProteinMPNN model trained with extra input per residues specifying buried and interface residues[44] using the argument --model_type "per_residue_label_membrane_mpnn". In this case the lipid-facing residues were parsed into ProteinMPNN using the --transmembrane_buried argument. Other constraints were applied in the same way as described above.

2.3. Computational methods: Structure prediction on designed sequences

AlphaFold2 was primarily used to judge if the designed sequences would fold and assemble into homo-oligomers as designed. Model 4 seemed to be most predictive of the designed alpha-helical transmembrane proteins and was the only model used. Designs were first filtered by confidence scores (typically pTM > 0.85 and mean PAE scores < 10 for all residue pairs corresponding to different chains) and then manually inspected to exclude designs with clusters of hydrophobic residues outside the defined lipid-embedding regions.

For estimating ion binding at the selectivity filters, AlphaFold3[45] was used to predict the formation of protein-metal complexes. Note that there could be clusters of negatively charged residues on the surface of the designed proteins forming potential ion binding sites. Therefore, multiple copies of ions were often included as the input rather than a single ion.

2.4. Experimental methods: Construction of synthetic genes

The amino acid sequences of the designs were reverse translated to DNA sequences using DNAworks (Hoover, D. and Lubkowski, J., 2002, https://github.com/davidhoover/DNAWorks). Synthetic genes encoding the designs were ordered from Genscript Inc. (Piscataway, N.J., USA) or Integrated DNA Technologies, Inc. (IDT, Coralville, Iowa, USA). The genes encoding the designs for protein expression and purification were cloned into pET29b+ vector between NdeI and XhoI sites with a C-terminal hexahistidine tag. The genes encoding the designs for expression in HEK293T cells were cloned into the LentiGuide-BC-EF1a vector between XbaI and EcoRI sites with a C-terminal FLAG tag (DYKDDDDK). The genes encoding the designs for expression in insect cells were cloned into the MCS-1 of pFastBac-Dual vector between BamHI and XbaI sites with a C-terminal hexahistidine tag.

2.5. Experimental methods: Expression of designed channels in HEK cells

HEK293T cells were maintained at 37 °C with 5% CO_2 and cultured in Dulbecco's Modified Eagle's Medium (DMEM, Gibco) supplemented with 10% FetalClone II serum (FC-II, Cytiva HyClone) and 1% penicillin-streptomycin (Gibco). To favor a more homogeneous expression level for more consistent flux assay results, we expressed the designed channels in HEK293T cells by lentivirus transduction based on a published protocol with some minor modifications[46].

To prepare the lentivirus, cells were transfected with the design plasmid, the envelope plasmid pMD2.G (Addgene #12259) and the packaging plasmid psPAX2 (Addgene #12260) at a 3:4:5 mass ratio using Lipofectamine 3000 (Thermo Fisher L300015). Media was exchanged after 4 hours. At 24 hours post-transfection, caffeine was supplemented to a final concentration of 2 mM to generate virus with higher titer. The virus-containing supernatant was harvested 72 hours after transfection and filtered through 0.45 µm surfactant-free cellulose acetate (SFCA) filters (Corning 431220). The prepared viruses were used immediately or stored at –80 °C.

For lentiviral transduction, cells were dissociated from the culture flask using 0.05% trypsin-EDTA (Gibco) and resuspended in DMEM-10% FC-II medium supplemented with polybrene (8 µg/mL, Santa Cruz Biotechnology) at a cell density of 1,000,000 cells/mL. Viral supernatant was added to this cell suspension (typically 200 µL viral supernatant was used to transduce 1 mL of the above cell suspension). The cells-virus mixture was centrifuged at 1000 g for 2 hours at 33 °C. Media was exchanged 24 hours after infection.

2.6. Experimental methods: Flux assay of designed channels in HEK cells

At 48 hours post-infection, transduced cells were seeded into glass-bottom 96-well plates (Cellvis P96-1.5H-N) pretreated with 0.05% poly-D-lysine hydrobromide (Sigma, dissolved in sterile-filtered Milli-Q water) at a density of 60,000 cells per well. A Ca^{2+}-free HEPES-buffered solution (20 mM HEPES pH 7.4, 150 mM NaCl, 5 mM KCl, 2 mM $MgCl_2$, 10 mM glucose, osmolarity adjusted to 330 mmol/kg using sucrose) was used as the assay buffer. To prepare the dye-loading solution, a vial of Fura-2 AM dye (Invitrogen F1221, 50 µg) was thawed, resuspended in 10 µL DMSO, and added to the assay buffer supplemented with Powerload (Invitrogen P10020) and probenecid (Invitrogen P36400) to a final dye concentration of 5 µM. Cell culture media was replaced with this dye-loading solution and incubated for 1 hour at room temperature. After the dye loading step, the cells were washed with the assay buffer twice, incubated in the assay buffer, and measured for fluorescence at 510 nm with excitations at 340 nm and 380 nm (F340/F380) using the Neo2 plate reader. The measurement was performed for 15 minutes to obtain the baseline fluorescence. Subsequently, Ba^{2+} was added to the cells to a final concentration of 2 mM and the fluorescence was measured for 15 minutes to obtain the change of fluorescence ratio over time. Data were exported as Excel tables, processed and plotted using Python.

2.7. Experimental methods: Immunofluorescence

HEK293T cells expressing the designs were pre-seeded into glass-bottom 96-well plates (treated with poly-D-lysine) as were done for the flux assay. All the following steps were performed at room temperature. Cells were washed twice with Dulbecco's phosphate buffered saline (PBS, Gibco) and fixed with 4% formaldehyde (diluted from Pierce 16% formaldehyde ampules with PBS) for 10 minutes. The fixation solution was washed twice with PBS. Subsequently, cells were permeabilized using 0.2% saponin in PBS for 20 minutes, followed by washing with PBST (0.1% Tween-20 in PBS) three times. Cells were then blocked with 5% BSA in PBST for 1 hour, followed by washing with PBST for three times. Cells were then incubated with the primary antibody (Sigma monoclonal anti-FLAG M2 antibody, mouse, 1:1000 dilution in PBST) for 1 hour, washed three times with PBST, incubated with the secondary antibody (Invitrogen goat anti-mouse IgG conjugated with Alexa Fluor 488, 1:1000 dilution in PBST) for 1 hour, and washed three times with PBST. After the final washing step, the 96-well plate was loaded onto the IN Cell analyzer 2500HS microscope for imaging. Images were processed using the Fiji distribution of ImageJ.

2.8. Experimental methods: Protein production

The designs in pET29b+ vector were transformed into *Escherichia coli* (E. coli) expression strain BL21(DE3*) (New England Biolabs, MA, USA). The transformed cells were grown in 50 mL Terrific Broth II (TB-II, MP Biomedicals) medium with a final concentration of 50 µg/ml kanamycin in 250 mL baffled flasks overnight. The 50 mL cultures were inoculated into 500 mL TB-II medium in 2 L baffled flasks and incubated at 37 °C. After 3 hours, isopropyl β-D-1-thiogalactopyranoside (IPTG) was added to a final concentration of 0.5 mM. The cultures were incubated at 18 °C following the addition of IPTG and were harvested after 3 hours by centrifuging at 4000 g for 10 minutes at 12 °C. The cell pellets can be stored at –80 °C.

2.9. Experimental methods: Buffer recipe for protein purification

Lysis buffer: 20 mM Tris-HCl, 150 mM NaCl, pH 8.0, supplemented with Pierce Protease Inhibitor Tablets (Thermo Scientific A32963, 1 tablet per 100 mL solution)

Solubilization buffer: 20 mM Tris-HCl, 150 mM NaCl, pH 8.0, supplemented with 2% w/v n-Decyl-β-D-Maltopyranoside (DM, Anatrace D322)

Wash buffer 1: 50 mM Tris-HCl, 300 mM NaCl, 30 mM imidazole, pH 8.0, supplemented with 0.06% w/v glyco-diosgenin (GDN, Anatrace GDN101)

Wash buffer 2: 50 mM Tris-HCl, 1 M NaCl, 30 mM imidazole, pH 8.0, 0.06% GDN

Wash buffer 3: 50 mM Tris-HCl, 300 mM NaCl, 60 mM imidazole, pH 8.0, 0.06% GDN

Elution buffer: 50 mM Tris-HCl, 300 mM NaCl, 500 mM imidazole, pH 8.0, 0.06% GDN

SEC buffer 1: 20 mM Tris-HCl, 150 mM NaCl, pH 8.0, 0.06% GDN

SEC buffer 2: 20 mM Tris-HCl, 150 mM NaCl, pH 8.0, 0.006% GDN

2.10. Experimental methods: Purification of designed calcium channels

The cell pellets were resuspended in 30 mL lysis buffer. The suspension was placed on ice and lysed by sonication (QSonica Sonicators, CT, USA) for 4 minutes (15 seconds on/15 seconds off, 8 minutes total run time) at 65% power with ¾” Dia replaceable tips.

The lysates were centrifuged at 10,000 g for 15 min to remove the cell debris. The supernatant was collected and ultracentrifuged at 170,000 g for 1 hour at 12 °C using Beckman Optima XE-90 Ultracentrifuge to pellet down the membrane fraction. 8 mL solubilization buffer was added to the pellet and incubated at 4 °C overnight on a rocker. The homogenate was centrifuged at 30,000 g for 30 minutes to pellet down the materials that could not be solubilized by DM. The supernatant was collected and applied to chromatography columns (BIO-RAD Econo-Pac gravity flow columns) containing Ni-NTA resin (Qiagen, MA, USA). The resin was washed with 5x column volume (CV) of wash buffer 1, 5x CV of wash buffer 2 and 3x CV of wash buffer 3. The proteins were eluted with 4x CV of elution buffer, concentrated in 100 kDa molecular weight cutoff spin concentrator (Millipore), and further purified by size exclusion chromatography (SEC) in SEC buffer 1. Normally a Superdex 200 Increase 10/300 GL column was used. For designed proteins connected with DHR, a Superose 6 increase 10/300 column was used. Both types of columns were from Cytiva, MA, USA. The target elution volume containing the desired oligomeric states of the designs was compared with validated *de novo* designed transmembrane proteins with similar molecular weight (for example, TMH4C4, which approximated a molecular weight of around 100 kDa, and TMHC6, which approximated a molecular weight of around 60 kDa).

In many cases, there seemed to be an evident aggregation peak when samples were applied on the SEC column after Ni-NTA purification. This is a well-known issue for the purification of membrane proteins, whereby the behavior of membrane proteins in vitro is largely dependent on the detergent or lipids utilized. We took a similar purification strategy as for purifying mammalian voltage-gated sodium channels[47–51]: we took the latter portion of the elution peak containing the proteins that were estimated to be in the desired oligomeric states, and subjected this portion to the a second SEC run in a buffer with ten 10 times less detergent (SEC buffer 2). The second SEC yielded a more distinct peak corresponding to the protein in the desired oligomeric states, which enabled us to separate the species of interest. 0.006 % GDN was used in the final buffer, as this consistently gave the optimal EM results.

2.11. Experimental methods: Circular dichroism (CD) measurements

CD spectra were measured on J-1500 Circular Dichroism Spectrophotometer (Jasco). Proteins were prepared at ~0.2 mg/mL in SEC buffer 2. Wavelength-scan spectra were recorded from 190 nm to 260 nm (0.1 nm increments). Temperature melting experiments were conducted from 25 °C to 95 °C (heating rate 1 °C/min), with wavelength-scan spectra recorded at every 10 °C increment. The full spectra were measured again after the samples were cooled down to 25 °C.

2.12. Experimental methods: Negative-stain electron microscopy

Proteins were prepared at ~0.05 mg/mL in SEC buffer 2 for ns-EM. 6 μL of the protein sample was applied on glow discharged, carbon-coated 400-mesh copper grids (Electron Microscopy Sciences). The samples were allowed to adhere to the grids for 1 min before being wicked away. Then each grid was stained with 3 μl of 2% uranyl formate for four times, each time 20 seconds. The grids were air-dried and were imaged on a FEI Talos L120C TEM (FEI Thermo Scientific, Hillsboro, OR) equipped with a Ceta 4K CCD camera at a magnification of 73,000x at 120 kV. Micrographs collection was automated using the EPU software (FEI Thermo Scientific). Collected datasets were imported into CryoSPARC software (v4.6.0) for 2D class averaging. Micrographs were motion-corrected and CTFs were estimated using Patch CTF estimation function. For each dataset, ~200 particles were selected using the manual particle picker function to generate initial 2D class averages using the 2D classification program in CryoSPARC. The 2D class averages were used as templates for automated particle picking using the template particle picking function after which 50 classes of 2D class averaging were generated for analysis.

2.13. Experimental methods: Cryogenic electron microscopy

This experimental section was a collaborative effort involving myself and my colleagues, Connor Weidle, Andrew Borst, and Kenneth Carr at UW IPD Electron Microscopy Research Core (EMRC). I prepared the protein sample solution. My colleagues prepared the cryo-EM grids, operated the microscope, collected the images and performed data processing. The parameters for cryo-EM data collection and processing were concluded in a table at the end of this section.

2.13.1. Experimental methods: Sample preparation

For CalC6_3, 3 µL of protein at ~ 1 mg/mL in SEC buffer 2 (20 mM Tris-HCl pH 8, 150 mM NaCl, 0.006% GDN) was applied to glow-discharged (25 seconds at 15 mA) 3 nm lacey carbon Cu 400 mesh grids (Electron Microscopy Sciences).

For CalC6_3 with DHR extensions, protein was prepared at ~1 mg/mL in SEC buffer 2 (20 mM Tris-HCl pH 8, 150 mM NaCl, 0.006% GDN). 2 µL of protein sample was applied to glow-discharged (25 seconds at 15 mA) C-flat R 2.0/2.0 300 mesh holey carbon grids (Electron Microscopy Sciences), and 3 µL of protein sample was applied to glow-discharged (16 seconds at 5 mA) Quantifoil 2 nm thin carbon R 2.0/2.0 300 mesh grids.

Vitrification was performed using a Mark IV Vitrobot at 22 °C and 100% humidity for all grids. Blotting was done before immediately plunge-frozen into liquid ethane. A blot time of 0.5 second, a blot force of 0 and a wait time of 7.5 second were used for lacey carbon grids and Quantifoil thin carbon grids. A blot time of 6.5 second, a blot force of 0, and a wait time of 7.5 second were used for holey carbon grids. The grids were then clipped and stored in liquid nitrogen for collection on the Titan Krios.

2.13.2. Experimental methods: Cryo-EM data collection

Samples were collected automatically on a ThermoFisher Titan Krios 300 kV microscope equipped with a K3 Summit direct electron detector and BioQuantum Gif energy filter. For CalC6_3 with DHR extensions (thin carbon and holey carbon grids) the microscope was operated in counting mode. For CalC6_3 (lacey carbon grids) super resolution mode was used. Data were collected with random defocus ranges spanning between −0.8 and −1.8 μm using beam-image shift five shots per hole and nine holes per stage move were collected for CalC6_3 with DHR extensions (thin and holey carbon grids) and 27 shots per stage movement (3 x 9) for CalC6_3. Altogether 6,893, 7,376, and 4,644 movies with pixel sizes of 0.843, 0.843, and 0.4135 and doses of 47.32, 47.32, and 60 e-/Å^2 were recorded for CalC6_3 with DHR extensions on thin carbon grid, holey carbon grid, and CalC6_3 on a lacey carbon grid, respectively.

2.13.3. Experimental methods: Cryo-EM data processing

All data processing was carried out in CryoSPARC v4.4. For all movies Patch Motion then Patch CTF data processing was carried out as an initial processing step. Custom settings are mentioned for refinement jobs in the protocol, otherwise default settings were used.

For CalC6_3: Curate Exposures was used to remove 1,078 micrographs, leaving 3,566 good micrographs. Blob Picking was used with a minimum particle diameter of 80 Å and a maximum particle diameter of 120 Å. An extraction box size of 300 pixels, and 680 pixels fourier cropped to 340 pixels was used. Following an Inspect Picks job 1,311,993, and 1,094,418 particles were extracted for 300- and 680-pixel sizes, respectively. Extensive 2D classification was performed on the 300-pixel size particles, however particles could not be effectively classified. The larger extraction box size of 680 yielded some low-resolution top views showing the pore. Further 2D classification and possible 3D refinement was abandoned in favor of the CalC6_3 with DHR extensions.

For CalC6_3 with DHR extensions: Curate Exposures was used to remove 172 and 1,217 bad micrographs, leaving 6,721 and 6,161 micrographs for thin and holey carbon grids respectively. Blob picking was used with a minimum particle diameter of 80 Å and maximum particle diameter of 160 Å. Particles were extracted at 340 pixels. Following an Inspect Picks job 8,115,000 and 7,293,711 particles were extracted for thin and holey carbon respectively. For thin carbon particles an initial round of 2D classification, 150 classes with a circular mask of 220 Å was used. From these 886,110 particles representing top and side views were further 2D classified with: 150 classes, batch size per class of 400, 50 online-EM iterations, min over scale after first iteration set to true, with 3 final iterations using all particles. For holey carbon particles an initial round of 2D classification with: 400 classes, and number of final iterations set to 5 was used. From these 185,009 particles representing top and side views were further 2D classified: 50 classes, and 5 final iterations with all particles. Top view classification was abandoned for holey carbon as no secondary structure could be resolved. From the holey carbon 142,660 particles were identified as side views by the visible DHR extensions.

For the hexamer structure only the thin carbon data were used. 115,880 particles of top/tilted views were selected from the previous 2D classification job. 110,256 particles with side views were further 2D classified separately using: A maximum resolution and a maximum alignment resolution of 3 Å, circular mask diameter and circular mask diameter outer set to 100 Å and 120 Å respectively (to mask out the flexible DHR extension), a batch size per class of 400, and number of online-EM iterations set to 40 was used. Of these true side views 13,304 particles were selected where clear secondary structure was visible. These final 129,184 particles with side and top/tilted views were further classified by generating 2 ab initio classes with: C6 symmetry, initial lowpass resolution set to 15 Å, GSFSC split resolution set to 10 Å, and optimize per-particle defocus set to true. The best ab initio volume and 85,292 particles were used to generate a 4.19 Å volume using Non-Uniform refinement with: C6 symmetry, initial lowpass resolution set to 15 Å, GSFSC split resolution set to 10 Å, and optimize per-particle defocus set to true. To correct for any aberrations introduced from the beam-image shift collection strategy, Exposure Group Utilities was used to split the data into 101 exposure groups, using Global CTF Refinement with settings: Fit spherical aberration set to true, fit tetrafoil set to true. The subsequent Non-Uniform refinement job improved the resolution of the map to 3.79 Å using: C6 symmetry, initial lowpass resolution set to 15 Å, GSFSC split resolution set to 10 Å, and optimize per-particle defocus set to true. This 3.79 Å map was used as an input for Reference Based Motion Correction, followed by another Non-Uniform Refinement which further improved the map resolution to 3.60 Å using the following custom settings: symmetry C6, number of extra final passes 5, initial lowpass resolution set to 15 Å, GSFSC split resolution set to 10 Å, and optimize per-particle defocus set to true. Using the remaining 83,766 particles and the 3.60 Å map as the input, a round of heterogeneous refinement was performed in C1 with 8 volumes. The particles from the 4 best volumes with clearly defined secondary structure were kept. 67,181 particles were used to generate the final volumes with No Uniform Refinement in C1 and C6 symmetry with: initial lowpass resolution set to 15 Å, GSFSC split resolution set to 10 Å, and optimize per-particle defocus set to true. Final resolutions were 3.75 Å and 3.98 Å for C6 and C1 maps respectively. While a slight drop in resolution was observed the map quality was much higher when visually inspected. The final C6 map used for model building was sharpened with DeepEMhancer.

For the heptamer structure the thin and holey carbon data was used, utilizing top and tilted views from the thin carbon and side views from both the thin and holey carbon data. From the second 2D classification of the particles on the thin carbon grid, 8 classes of 89,183 particles were selected with top and tilted views that appeared to be larger than hexamers by visual inspection. 110,256 particle side views from the thin carbon grid and 142,660 particle side views from the holey carbon grid were combined and an initial 2D classification was performed with settings: maximum resolution and maximum alignment resolution of 3 Å, circular mask diameter and circular mask diameter outer of 130 Å and 150 Å respectively, batch size of 400, force max over poses/shifts set to false, number of online-EM interactions set to 40. Subsequent 2D class averages were removed that appeared to be hexamer. 66,778 particles were further 2D classified using: maximum resolution and maximum alignment resolution of 3 Å, circular mask diameter and circular mask diameter outer of 100 Å and 120 Å respectively, batch size of 400, force max over poses/shifts set to false, number of online-EM interactions set to 40. 46,550 particles were selected where any secondary structure was visible and an additional 2D classification was performed using: maximum resolution and maximum alignment resolution of 3 Å, circular mask diameter and circular mask diameter outer of 100 Å and 120 Å respectively, batch size of 400, force max over poses/shifts set to false, number of online-EM interactions set to 40. 20,173 particles with clear secondary structure were selected. Using the 89,183 particles of heptameric top/tilted views and the 20,173 particles from extensive 2D classification of side views additional sorting was done with an Ab Initio job using: 3 ab initio classes, C7 symmetry, maximum resolution of 6 Å, Initial resolution of

25 Å. The best ab initio volume was selected containing 45,077 particles, and used for a Non-Uniform Refinement job both in C7 and C1 symmetry with: number of extra final passes set to 5, initial lowpass resolution set to 15 Å, GSFSC split resolution set to 10 Å, and optimize per-particle defocus set to true. For the C7 and C1 map a resolution of 4.62 Å and 5.13 Å was achieved respectively. The final C7 map used for model building was sharpened with DeepEMhancer.

2.13.4. Experimental methods: Cryo-EM structure model refinement

For all structures, the design models were used as an initial reference for building the final cryo-EM structures. For the hexamer the design model of the CalC6_3 was used as an initial reference model. For the heptamer, CalC6_3 with DHR extension was used as a starting model, as more of the DHR extension was visible in this map. A single chain for the heptamer was isolated in PyMOL and 7 copies of this chain were fitted to the map in UCSF Chimera to reform the channel. Hexamer and heptamer were refined using several rounds of relaxation and minimization, performed on the complete structures, which were manually inspected for errors each time using Isolde[52], Coot[53], and Phenix[54] real-space refinement. The final model quality was analyzed using MolProbity[55]. Figures were generated using UCSF ChimeraX.

Table 1: Cryo-EM data collection and processing parameters for CalC6_3 with DHR extension.

Data Collection		
Microscope	Titan Krios	
Voltage (kV)	300	
Detector	Gatan K3	
Energy Filter	Gatan BioQuantum Gif	
Recording mode	Counting	
Magnification	105,000 X	
Movie micrograph pixel size (Å)	0.843	
Dose rate (e^-/Å^2/s)	11.83	
No. of frames per movie micrograph	79	
Frame exposure time (s)	0.0506	
Movie micrograph exposure time (s)	4.0	
Total dose (e^-/Å^2)	47.32	
Under focus range (µm)	0.8-1.8	
Number of movie micrographs	14,269	
Map Processing	Hexamer	Heptamer
Extraction Box Size (pix)	340	340
Initial particle images (no.)	886,110	886,110
Final particle images (no.)	67,181	45,077
Map resolution (Å)	3.75	4.62
FCS threshold	0.143	0.143
Map resolution range (Å)	3.38-4.56	4.20-8.80
Refinement		
Initial model used	Design Model	Design Model
Map resolution (Å)	3.75	4.62
FCS threshold	0.143	0.143
Model resolution range	3.38-4.56	4.20-6.5
Map sharpening B factor	Na	343.8
Model composition		
Non-hydrogen atoms	6,215	6,069
Protein Residues	846	1,057
Ligands	0	0
B factors (Å)		
Protein	Na	249.89
Ligands	Na	–
R.M.S. deviations		
Bond lengths (Å)	0.012	0.001
Bond angles (°)	1.795	0.369
Validation		
MolProbity score	1.00	0.69
Clashscore	0.78	0.57
Rotamer Outliers (%)	2.13	0.00
Ramachandran plot		
Favored (%)	98.32	99.33
Allowed (%)	1.68	0.67
Disallowed (%)	0.00	0.00

2.14. Experimental methods: Characterize the conductance of designed channels

We use the Bac-to-Bac system (Gibco) to express the designed channels in *Trichoplusia ni* insect cells (Hi5) for whole-cell patch-clamp experiments. The main advantage of this expression system is that cells expressing the designed proteins can be readily identified based on the morphological changes of Hi5 cells after being infected (characteristic features include an expansion of cell nuclei and an increase in cell granularity).

2.14.1. Insect cell culture

SF9 cells and Hi5 cells were maintained at 27 °C and cultured in Grace's Insect Medium supplemented with 10% fetal bovine serum (Avantor Seradigm 89510-186) and 1% penicillin-streptomycin-glutamine (Cytiva Hyclone). This medium was referred to as "supplemented medium" in the following sections.

2.14.2. Baculovirus generation

The preparation of bacmid and baculovirus can also follow Invitrogen's manual of Bac-to-Bac Baculovirus Expression System available online. We used a protocol that has been developed in the lab and previously used in published research. Designs in pFastBac-Dual vector were transformed into MAX Efficiency™ DH10Bac Competent Cells (Gibco). The transformed E. coli cells were then plated on LB agar plates supplemented with 50 µg/mL kanamycin, 7 µg/ml gentamicin, 10 µg/mL tetracycline, 100 µg/mL Bluo-Gal and 40 µg/ml IPTG and incubated at 37 °C for 48 hours. White colony was picked and transferred to 2 mL LB media supplemented with 50 µg/mL kanamycin, 7 µg/mL gentamicin and 10 µg/mL tetracycline to grow overnight. The cells were harvested by centrifugation at 14,000 g for 2 minutes and resuspended in 300 µL Solution 1 (15 mM Tris-HCl pH 8.0, 10 mM EDTA, 100 µg/ml RNaseA). 300 µL Solution 2 (0.2 M NaOH, 1% SDS) was added to this suspension, followed by gentle inversions several times and incubation at room temperature for 5 minutes to form clear lysates. 300 µL Solution 3 (potassium acetate, pH 5.5) was added to the lysate, followed by incubation on ice for 5 minutes. Cell debris was removed by centrifugation at 14,000 g for 10 minutes. 700 µL supernatant was mixed with 800 µL isopropanol and incubated on ice for 10 minutes. The mixture was centrifuged at 14,000 g for 10 minutes to pellet down the bacmid DNA. After the supernatant was discarded, the pellet was washed with 500 µL 70% ethanol, air dried at room temperature, and resuspended in 40 µL dH_2O.

SF9 cells were seeded into 6-well tissue culture dishes at 50% confluency. Grace's Insect Medium without serum or antibiotics (unsupplemented media) was used for transfection at this step. 10 µg bacmid DNA was added into 100 µL unsupplemented medium. 6 µL of Cellfectin II Reagent (Gibco) was diluted by 100 µl of unsupplemented medium and mixed with the bacmid DNA. The mixture was incubated at room temperature for 30 minutes. Pre-seeded SF9 cells were washed once with 2 mL unsupplemented medium. 800 µl of unsupplemented medium was added to the DNA-Cellfectin mixture and added to the cells. Media was exchanged to supplemented medium after incubation at 27 °C for 5 hours. The virus-containing supernatant was harvested 72 hours after transfection and was centrifuged at 500 g for 5 minutes to remove cell debris.

The virus (P1) was amplified once to generate a stable stock by addition to the SF9 cells cultured in the 150-mm tissue culture dish (at ~70% confluency). From the culture dish medium was aspirated, and virus suspension was gently added to the cells. The tissue culture dish was put on a rocker at room temperature for 1 hour, and incubated at 27 °C after addition of 25 mL medium. 48 hours after infection the virus-containing supernatant was harvested by centrifugation at 500 g for minutes and was stored at 4 °C (P2 virus).

2.14.3. Western blot analysis

Western blot was used to confirm the expressions of designed channels. Hi5 cells were seeded into a 6-well tissue culture dish at 50% confluency. To infect the cells, medium was aspirated, and 5 µL of the P2 virus was added to the cells. The dish was put on a rocker at room temperature for 1 hour, and incubated at 27 °C after addition of 2 mL medium. Cells were harvested 48 hours after transfection, washed with 1 mL TBS buffer

(20 mM Tris-HCl pH 8, 150 mM NaCl) supplemented with pierce protease inhibitor, and resuspended in 60 µl TBS buffer. 5 µL of the cell suspension was added to 50 µL of the 2x Laemmli Sample Buffer (BIO-RAD) supplemented with 2-mercaptoethanol and loaded on gel. Proteins were transferred to the nitrocellulose membrane using the BIO-RAD Trans-Blot Turbo Transfer system. The membrane was incubated with 5% blotting grade blocker nonfat milk (BIO-RAD) in TBST (20 mM Tris-HCl, pH 8, 150 mM NaCl, 0.05% Tween 20) at 4°C overnight. On the following day the membrane was washed three times with TBST and incubated with anti-His tag antibody conjugated with Horseradish Peroxidase (Jackson ImmunoResearch 300-035-240) in TBST (1:5000 dilution) for 1 hour. After antibody binding, the membrane was washed four times with TBST. Chemiluminescence was activated by BIO-RAD Clarity Western ECL Substrate and imaged using LI-COR Odyssey M Imager.

2.14.4. Solution recipe for electrophysiology

All solutions used for electrophysiology were prepared from the stock solutions below:

NMDG-$MeSO_3$ stock solution: 1.4 M NMDG, 200 mM HEPES, pH adjusted to 7.2 by methanesulfonic acid (~1.3 M)

NMDG-Cl stock solution: 1.4 M NMDG, 200 mM HEPES, pH adjusted to 7.2 by HCl (estimated Cl^- concentration of 1.3 M based on the added HCl volume)

$NaMeSO_3$ stock solution: 1.4 M NaOH, 200 mM HEPES, pH adjusted to 7.2 by methanesulfonic acid (~1.3 M)

Stock solutions of divalent ions (Mg^{2+}, Ca^{2+}, and Sr^{2+}) were prepared by mixing the corresponding hydroxides with $MeSO_3$ to a final concentration of 100 mM for the metal ions. A little excess of $MeSO_3$ was usually required to ensure complete dissolving of the metal hydroxides to a final pH of 3~5.

EGTA stock solution: 100 mM EGTA, 200 mM NMDG.

Extracellular solution: 140 mM NMDG, ~130 mM $MeSO_3$, 20 mM HEPES, ~4 mM Cl^-, x mM metal ions of interest, pH 7.2, osmolarity adjusted to 355 mmol/kg.

Intracellular solution: 160 mM NMDG, ~110 mM $MeSO_3$, 20 mM EGTA, 20 mM HEPES, ~10 mM Cl^-, 4 mM MgATP, pH 7.2, osmolarity adjusted to 345 mmol/kg.

pH was adjusted using 1 M NMDG solution. Osmolarity was measured on a vapor pressure osmometer (VAPRO).

2.14.5. Electrophysiology recording

Hi5 cells were seeded onto 10 mm glass coverslips (Ted-Pella, pre-cleaned with 70% ethanol) in 35 mm tissue culture dishes (GenClone 25-200). To express the designs in Hi5 cells, medium was aspirated, and 2 µl of the P2 virus was added to the cells. The dish was put on a rocker at room temperature for 1 hour, and incubated at 27 °C after addition of 2 mL medium. Whole-cell patch-clamp experiments were performed at 18-24 hours after infection. Patch pipettes were pulled from 4 mm thin-wall borosilicate glass capillaries (World Precision Instrument TW150F-4) using Sutter Model P-1000 micropipette puller and had a resistance of 4-6 MΩ when filled with the intracellular solution. Extracellular solutions were applied using a gravity-fed perfusion system equipped with a 8-channel perfusion manifold (Warner Instruments MPP-8), a flow regulating valve (Warner Instruments FR-50), and a cell-bathing chamber (Warner Instruments RC-25). The recording electrode was prepared from silver wires (A-M Systems, 0.008 inch, bare) through electrical chloriding in 3 M KCl solution. A pellet Ag/AgCl electrode (World Precision Instruments, EP2) was used as the reference electrode. Whole-cell currents were recorded using an EPC10 amplifier and PatchMaster Next software (Harvard Biosciences, version 1.2). Current signals were filtered at 2.9 kHz. Cells were patched in the 2 mM [Ca^{2+}] extracellular solution. After breaking the patched cell membrane to establish the whole-cell configuration, the bath solution was changed to the 0.02 mM [Ca^{2+}] solution. A –100 mV to +100 mV voltage-ramp protocol was applied every 5 seconds with a holding potential of 0 mV. In most cases the recorded currents using this ramp protocol were used to generate the I-V curves. The I-V curve obtained in the 0.02 mM [Ca^{2+}] solution was used as the baseline for subtraction of leak current. The currents measured at –100 mV were used for generating the time courses. After the currents elicited by the voltage-ramp protocol became stable, the bath solution was changed to the one containing the ions of interest (for example, a solution containing 10 mM [Ca^{2+}] was used to determine the Ca^{2+} conductance). For measurement of channel conductance for different ions, the 0.02 mM [Ca^{2+}] solution was used between the solution exchange to remove the previous ion. Liquid junction potentials between the extracellular and intracellular solutions were calculated to be less than 1 mV (https://swharden.com/LJPcalc/) and therefore was not corrected for the command voltage. The cell capacitance was measured using the automated capacitance correction function of EPC10/Patchmaster Next. Data was exported as ASCII files and analyzed using Python.

2.14.6. Determination of ion concentrations for comparing relative conductances of designed channels for different ions

We use Goldman–Hodgkin–Katz (GHK) flux equation to determine the equivalent ion concentrations for comparing relative conductances of designed channels to different ions:

$$\Phi_s = P_s \cdot z_s^2 \cdot \frac{V_m F^2}{RT} \cdot \frac{[S]_i - [S]_o exp(-z_s V_m F/RT)}{1 - exp(-z_s V_m F/RT)} \qquad (1)$$

where Φ_s is the ion flux (i.e., the measured current or current density), P_s is the permeability for ion S, z_s is the valence of ion S, V_m is the membrane potential, F is the Faraday constant, R is the gas constant, T is the absolute temperature, and $[S]_i$ and $[S]_o$ are the intracellular and extracellular concentrations of ion S, respectively.

Given that we are comparing the inward currents and assume that there is no ion of interest inside the cell ($[S]_i = 0$), equation (1) is then simplified to:

$$\Phi_s = -P_s \cdot z_s^2 \cdot \frac{V_m F^2}{RT} \cdot \frac{[S]_o exp(-z_s V_m F/RT)}{1 - exp(-z_s V_m F/RT)} \tag{2}$$

To compare the permeability of two different ions (S_1 and S_2), Equation (2) can be rewritten as:

$$\frac{P_{s,1}}{P_{s,2}} = \frac{\Phi_{s,1}}{\Phi_{s,2}} \cdot \frac{z_{s,2}^2}{z_{s,1}^2} \cdot \frac{1 - exp(-z_{s,1} V_m F/RT)}{1 - exp(-z_{s,2} V_m F/RT)} \cdot \frac{[S_2]_o exp(-z_{s,2} V_m F/RT)}{[S_1]_o exp(-z_{s,1} V_m F/RT)} \tag{3}$$

Since in most cases the currents at –100 mV are compared ($V_m \ll 0$), equation (3) can be simplified to:

$$\frac{P_{s,1}}{P_{s,2}} = \frac{\Phi_{s,1}}{\Phi_{s,2}} \cdot \frac{z_{s,2}^2}{z_{s,1}^2} \cdot \frac{[S_2]_o}{[S_1]_o} \tag{4}$$

To directly compare the relative conductance of the channels for each individual ion using the measured current or current density, the following condition needs to be satisfied:

$$\frac{z_{s,2}^2}{z_{s,1}^2} \cdot \frac{[S_2]_o}{[S_1]_o} = 1 \tag{5}$$

Equation (5) can be written as:

$$\frac{[S_1]_o}{[S_2]_o} = \frac{z_{s,2}^2}{z_{s,1}^2} \tag{6}$$

Therefore, the ion concentration used for determining the relative conductances for different ions was inversely proportional to the square of valence of the particular ion. As a result, the concentration of divalent ions was determined to be 10 mM, and the concentration of Na^+ was determined to be 40 mM.

3. Results

3.1. Design pipeline and in silico validation of designed channels

All known native Ca^{2+} channels utilize negatively charged Glu or Asp residues in the selectivity filter, but in different configurations. For example, in Ca^{2+} channels within the superfamily P-loop channels, $Ca_v1.1$ has the selectivity filter asymmetrically formed by 4 glutamate residues with neighboring oxygen atom distances ranging from 3.3 Å to 5.4 Å[56], the homotetrameric TRPV6 channel has four Asp residues with diagonal oxygen atom distances of 4.6 Å[57], while this same diagonal distance in the Ca_vab channel (engineered from bacterial Na_vab channel) is 8 Å[4], and the Orai channel (which does not have a P-loop) has six Glu residues with a diagonal oxygen distance of 8 Å (in the solved open-state structure)[58].

Considering this ambiguity as well as the commonly observed flexibility of the Glu/Asp sidechains in those native channels, to simplify conformational sampling, we focused on the distance (R_s) between the Ca^{2+} ion and the C alpha (Cα) atom of the Glu (or Asp) regardless of rotamer which we refer to below as the radius of the selectivity filter. The Glu/Asp residue was placed in the x-y plane with the Ca^{2+} ion). In addition to this parameter of distance R_s, the pore was defined along with the following parameters: (1) the distance (R_B) from the Cα atom of a pore exit defining residue (with unspecified amino acid identity) to the z axis, which was used to define the radius of the pore exit; (2), the displacement along the z axis (h) between the selectivity filer residues and the pore exit residues; and (3) the symmetry group (in this case fourfold or sixfold symmetry were applied based on the commonly observed coordination states for the Ca^{2+} ion (we focused on C4 and C6 symmetries as these are the commonly observed Ca^{2+} coordination states[28]). Using RFdiffusion, the selectivity filter and exit pore defining residues were connected using helices to form the lining of the homooligomeric pore, and these helices were then extended into multi-secondary structure interacting subunits with L residues in each monomer. As the topology of the subunits is completely unspecified other than the pore lining helix, the diffusion process generates a wide diversity of solutions. Together, the selectivity filter generation and RFdiffusion scaffolding calculations generate multipass transmembrane protein backbones with central channels and different filter geometries (**Fig. 1**). Sequences were designed using ProteinMPNN[37] with position-specific amino acid constraints: the selectivity filter residues were fixed at Glu or Asp, the lipid-facing surface residues were constrained to be hydrophobic, and the remaining pore-lining residues were disfavored to be charged to avoid interference with ion permeation through the pore.

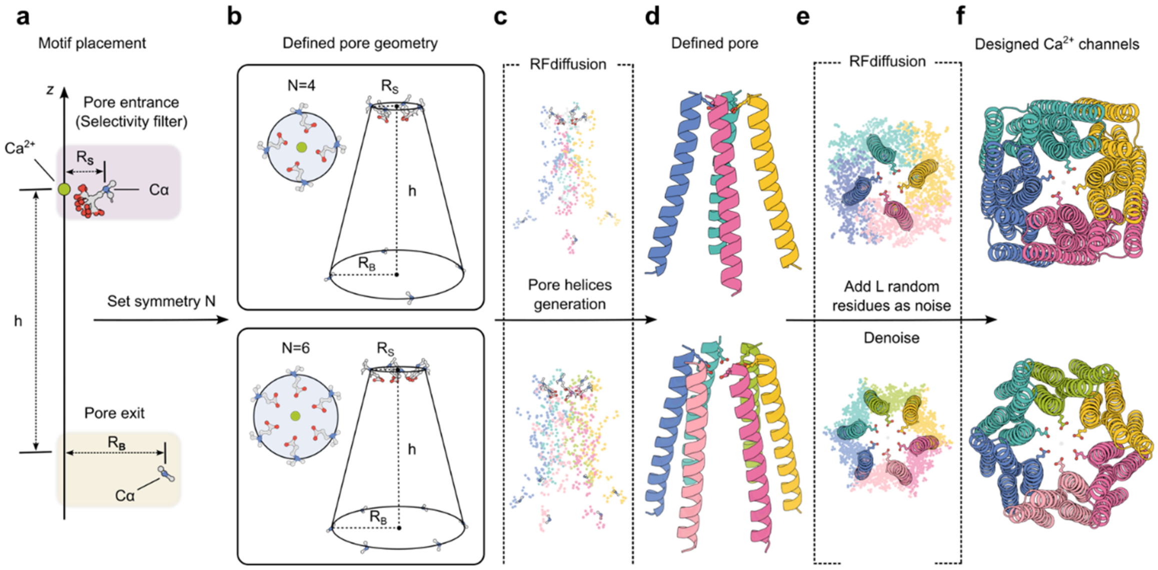

Fig. 1: A general approach for designing Ca^{2+} channels from selectivity filter geometry. a, A pair of Ca^{2+} ion (green sphere) and an acidic amino acid (Glu in this case, with the C-alpha atom colored in blue) and an additional pore exit defining residue (only backbone atoms shown) are used as the initial structural motifs. The distance between the Ca^{2+} ion and the C-alpha atom (R_S) defines the size of the selectivity filter regardless of the specific rotamer conformations of the Glu residue. The pore exit defining residue is positioned at a distance (h) along the z-axis from the Glu residue; the distance from the C-alpha atom of this residue to the z-axis (R_B) defines the radius of the pore exit. **b,** Application of N-fold cyclic symmetry generates the framework of the pore defined by R_S, R_B, h and symmetry (N), and the selectivity filter coordinating the Ca^{2+} ion. **c and d,** The selectivity filter and pore exit defining residues are connected by helices using RFdiffusion. **e and f,** The pore-lining helices are extended to form channel proteins using RFdiffusion by adding noise consisting of L residues in each monomer followed by a denoising trajectory.

A diverse set of designed channels with varying selectivity filter geometries (the tetramers are denoted CalC4, and the hexamers CalC6) were predicted by AlphaFold2-Multimer[38,59] to assemble into structures that closely resembled the design models (predicted templating modeling (pTM) score greater than 0.85 and Cα root-mean-square-deviation

(RMSD) less than 1 Å). Designs with many hydrophobic residues extending beyond the defined lipid-embedded regions were discarded. Four design examples with increasing radius of the selectivity filter orifice were shown in **Fig. 2**. More examples with pTM scores higher than 0.85 were shown in **Fig. 3**. Overall, 23 designs in the CalC4 series, 24 designs in the CalC6 series, and 24 designs in the CalC6_H featuring expanded selectivity filter sizes (H referred to as 'hollow') were selected for experimental characterizations.

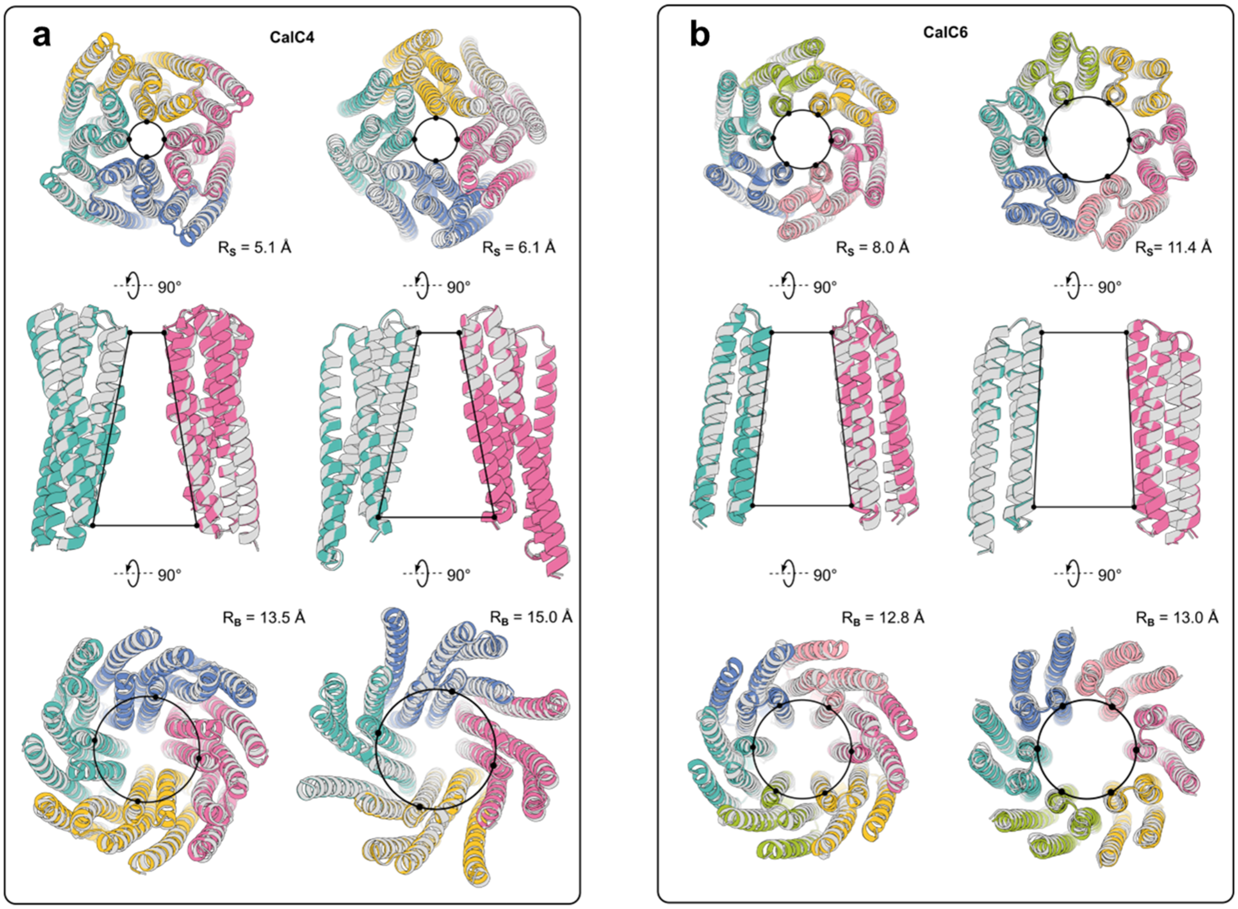

Fig. 2: Examples of designed channels. Design models (rendered by chains with colors) are aligned with AlphaFold2-predicted models (in gray) from the top view (top), side view (middle) and bottom view (bottom). For side views only the opposing two chains are shown for clarity. **a**, Two designs with C4 symmetry (CalC4), with backbone RMSD values of 0.8 Å and 0.2 Å to AlphaFold2 predictions, respectively. **b,** Two designs with C6 symmetry (CalC6), with backbone RMSD values of 0.8 Å and 0.5 Å to AlphaFold2 predictions, respectively.

Fig. 3: More examples of AlphaFold2-predicted structures of designed Ca^{2+}channels with pTM scores higher than 0.85. a, Designs with C4 symmetry. **b,** Designs with C6 symmetry.

3.2. Screen for putative functional designed channels

To experimentally validate that the designed proteins fold and function as desired, a cell-based flux assay was used with Fura-2 AM as the ion-responsive dye to screen for designs showing divalent ion permeability in cells. The designs were screened by function rather than by biochemical properties (protein folding and assembly) in this case. This is because (1) purification of transmembrane proteins is low-throughput and labor-intensive, and (2) the folding and assembly of designed proteins into oligomers does not necessarily guarantee the formation of a functional channel due to potential off-target hydrophobic interactions across different protein chains – residues at the helix-helix interfaces tend to be hydrophobic in favor of the packing of multiple helices, and residues on the surface of transmembrane proteins are hydrophobic as well for interactions with the lipid acyl tail. The Fura-2 AM dye[60] was chosen due to its ratiometric readout property, which reduces impacts caused by uneven dye loading into the cells through self-calibration, thereby facilitating measurement of multiple constructs in parallel using a plate reader (**Fig. 4**).

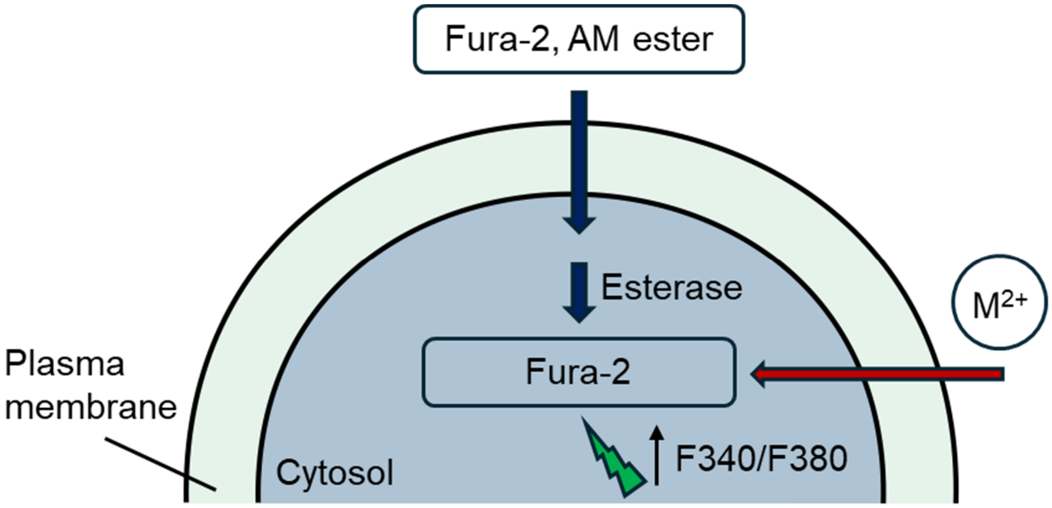

Fig. 4: Diagram of the flux assay using the Fura-2 AM dye for identifying functional designs. M^{2+} represents a divalent ion. F340/F380 represents ratio of fluorescence emission at 510 nm using 340 nm and 380 nm as the excitation source, respectively.

The genes encoding the designs were inserted after the EF1α promoter for expression in HEK293T cells. 24 designs with C6 symmetry (CalC6 series) were tested in the first round. The genes were first delivered into the cells by lipofection (using Lipofectamine 3000) and tested for Ca^{2+} influx using the Fura-2 dye. However, slight changes in the Fura-2 fluorescence were observed for all wells, including the negative control (cells treated with the transfection reagent without plasmids). The expressions of designed proteins were examined by immunofluorescence following cell fixation and permeation (using anti-FLAG antibody). All 24 designs expressed in the cells, despite variation in expression levels (**Fig. 5**). These results led to two hypotheses about the failure mode of the previous flux assay: 1) the Fura-2 dye response observed in the previous flux assay might result from both endogenously existing Ca^{2+}-permeating pathways and non-specific entry due to cell deaths, and 2) heterogeneous expression of designs by lipofection would result in large variations in the plate reader-based assay.

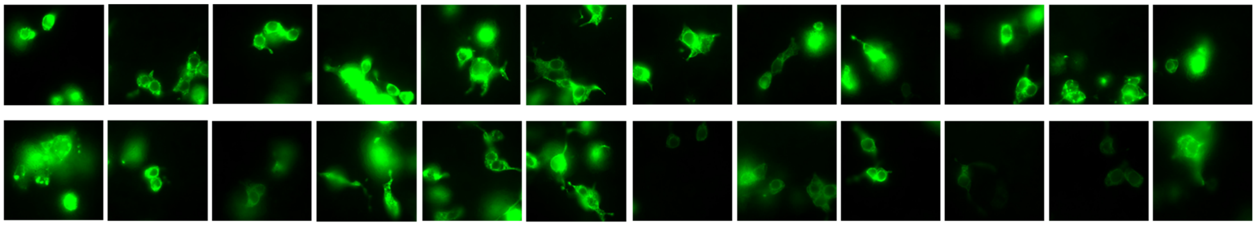

Fig. 5: Immunofluoresence imaging of HEK293T cells transiently transfected with plasmids encoding designed channels. Each sub image represents the result of an individual design. The fluorescence intensities for all images have been scaled to have the same maximum and minimum values.

Based on these hypotheses, we decided to express the designs by lentiviral transduction to generate a relatively more homogeneous expression level for the designed proteins. The LentiGuide-BC vector was compatible to serve as the transfer plasmid with the 2nd generation lentivirus packaging system. Both the transfection efficiency and the homogeneity of protein expression levels were both improved significantly as characterized by immunofluorescence in fixed HEK293T cells (**Fig. 6**).

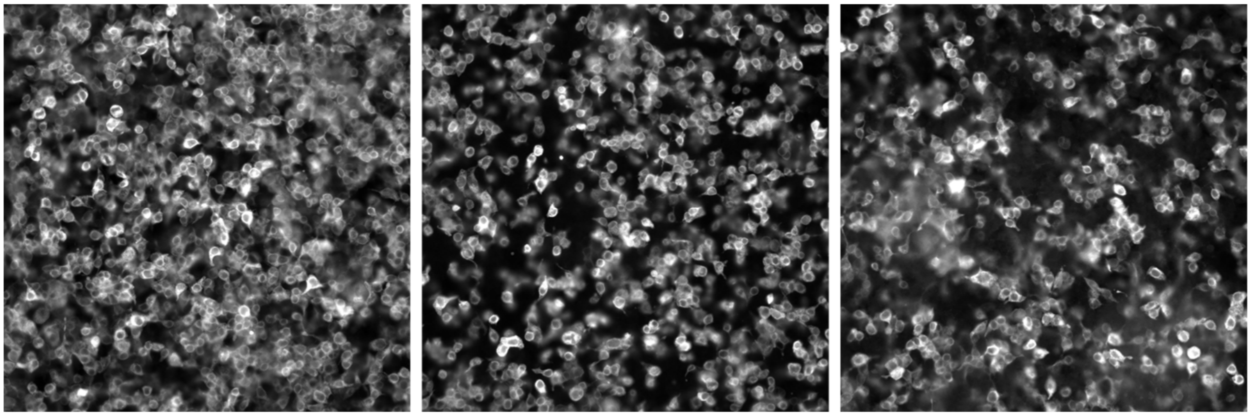

Fig. 6: Three representative immunofluorescence images of HEK293T cells expressing the designed proteins after lentiviral transduction. Each figure represents cells expressing a design.

Using this transfection approach, cells expressing the designed protein were subject to flux assay. Initially Ca^{2+} was added to a final concentration of 2 mM for measurement of Fura-2 fluorescence change after the cells were bathed and recorded in Ca^{2+}-free HEPES-buffered solutions; however, slight changes in fluorescence response were observed. Considering that cells may have a robust Ca^{2+}-buffering system (for example, the abundant calmodulin molecules[61] and the Ca^{2+} pumps), we instead used Ba^{2+} as the surrogate ion for Ca^{2+} to trigger the response of Fura-2, since the Fura-2 dye responds to Ba^{2+} in a similar manner as to Ca^{2+}. The addition of 2 mM Ba^{2+} indeed resulted in a larger change and less fluctuation in the Fura-2 fluorescence than 2 mM Ca^{2+}. Although the fluorescence response in the negative controls (cells only) was also larger in 2 mM $[Ba^{2+}]$ than in 2 mM $[Ca^{2+}]$, which probably resulted from endogenous divalent ion-permeable channels and was hard to eliminate, we were able to identify a few designs that exhibited significantly higher change in Fura-2 fluorescence than the negative control as well as than the other designs, and were marked as putative functional designed channels (**Fig. 7**).

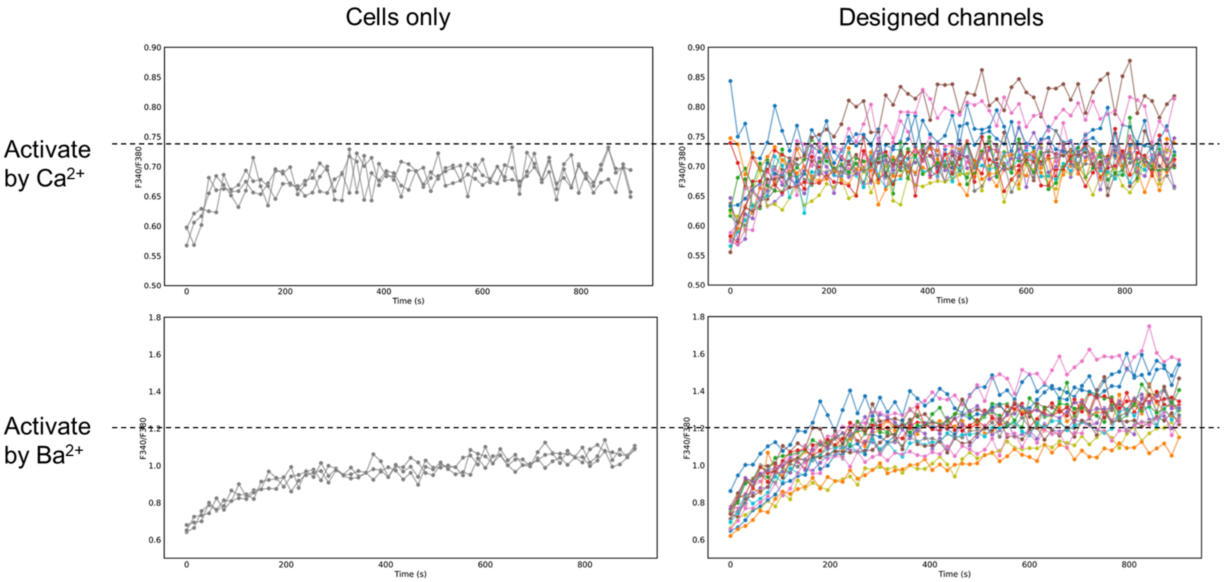

Fig. 7: Time courses of fluorescence change of Fura-2 after addition of divalent ions. Each line represents one measurement from an individual well in the microplate. Gray lines represent measurements from cells only. Colored lines represent measurements cells expressing the designed channels, each line representing one individual design. The top two figures represent time courses after addition of Ca^{2+}. The bottom two figures represent time courses after addition of Ba^{2+}. The dashed lines indicate the threshold F340/F380 values used for identifying functional channels.

The same experimental screening process was conducted on designs in CalC4 and CalC6_H series as well. Overall, 5 of 23, 6 of 24, and 9 of 24 designs in the CalC4, CalC6 and CalC6_H series, respectively, were produced with a higher change in the fluorescence ratio of the Fura-2 dye at 340/380 nm excitation in response to 2 mM Ba^{2+} than the baseline when expressed in cells (**Fig. 8**). These identified hits were cloned into pET29b+ vector for protein purification from E. coli and assessment of biophysical properties in vitro.

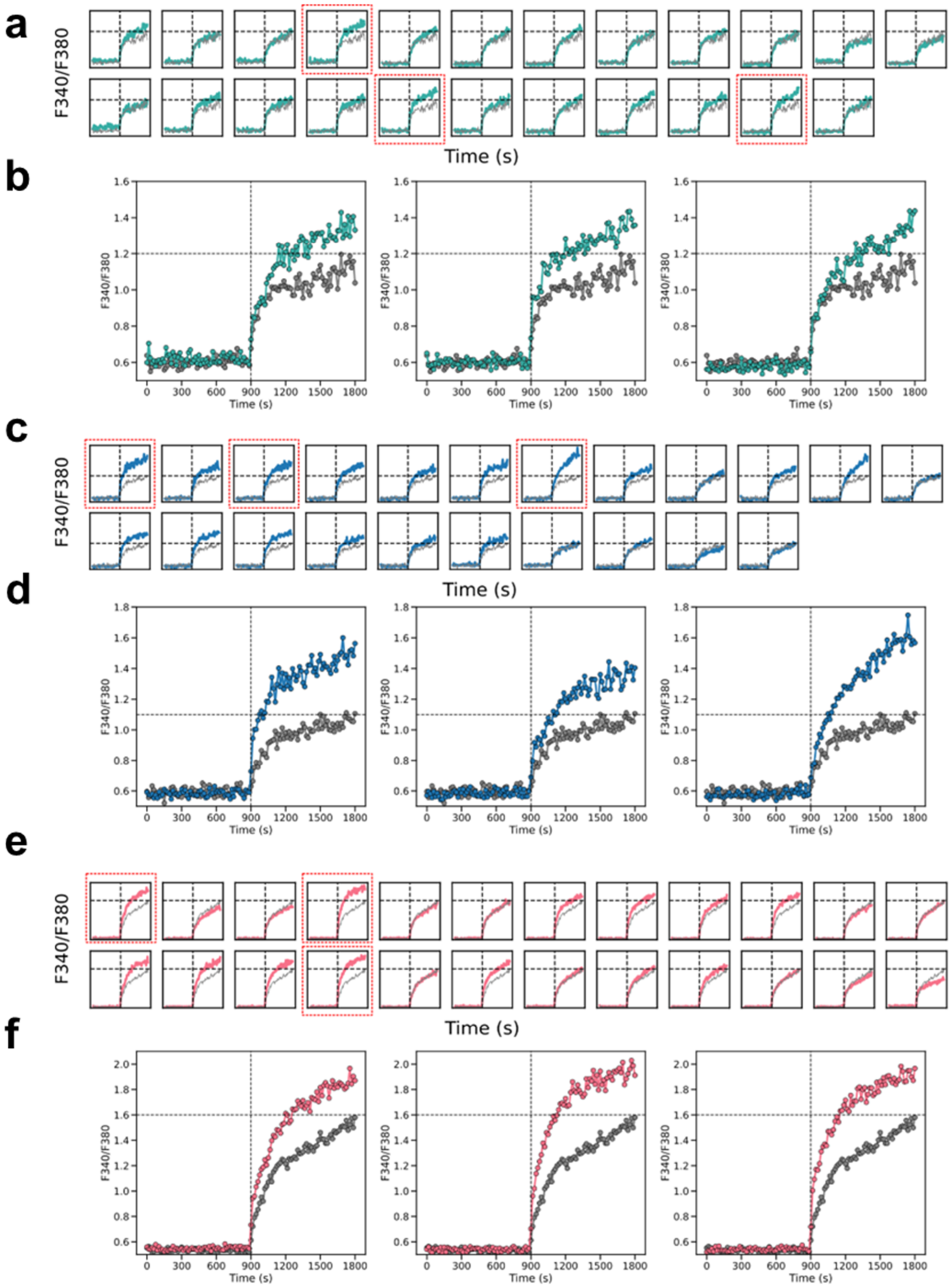
a
F340/F380
Time (s)
b
F340/F380
0.6
0.8
1.0
1.2
1.4
1.6
0
300
600
900
1200
1500
1800
Time (s)
c
F340/F380
Time (s)
d
F340/F380
0.6
0.8
1.0
1.2
1.4
1.6
1.8
0
300
600
900
1200
1500
1800
Time (s)
e
F340/F380
Time (s)
f
F340/F380
0.6
0.8
1.0
1.2
1.4
1.6
1.8
2.0
0
300
600
900
1200
1500
1800
Time (s)

Fig. 8: Flux assay in HEK293T cells using Fura-2 AM. a-b (cyan), **c-d** (blue), and **e-f** (red) were data for CalC4, CalC6, CalC6_H designs, respectively. Ba^{2+} ions were added at the 900-second time point indicated by the vertical dashed lines. The gray traces represented measurements from mock-transduced cells as the negative control and were overlaid with the colored traces representing the cells transduced with the designs in each plot for comparison. **b**, **d** and **f** were close-up views of the plots highlighted by the red dashed frames in **a**, **c** and **e,** respectively, which were examples that were identified as the putative designs manifesting divalent ion permeability.

3.3. Characterization of designed proteins in vitro

We expressed these designs in *Escherichia coli* (E. coli), purified them by nickel–nitrilotriacetic acid (Ni-NTA) affinity chromatography, and analyzed them by size exclusion chromatography (SEC) and negative-stain electron microscopy (ns-EM). Although this process is well-established in the lab and has been applied to several published studies, some modifications are needed to address the challenges of characterizing transmembrane proteins. First, the yield of transmembrane proteins is typically low, so in usual cases 500 mL of culture is used to express and purify one design for SEC and ns-EM analysis; more culture volume is required to obtain large amounts of proteins for structural determination such as cryogenic electron microscopy (cryo-EM). Second, sedimentation of membrane fractions is usually required to separate the transmembrane proteins from the abundant soluble endogenous proteins for protein purity. Most importantly, the choice of detergent is key to behaviors of transmembrane proteins in vitro; suboptimal detergent often results in protein aggregation or heterogeneous protein particles on the EM grid.

n-dodecyl-β-D-maltoside (DDM) and glyco-diosgenin (GDN) were the two detergents that were tried here as they have been successfully used for structural determination of transmembrane proteins in various publications. Their low critical micelle concentrations (CMC) also made them suitable for EM analysis by minimizing the formation of detergent micelles. Among the designs identified from the flux assay, CalC6_7 was used for optimizing the protein purification protocol. In addition, a designed transmembrane pore TMH4C4, which was previously published with a determined cryo-EM structure, was expressed, purified and characterized in parallel to CalC6_7 as a positive control (**Fig. 9**). Both DDM and GDN resulted in a protein aggregation peak on the SEC column, which was often unavoidable; however, the fraction eluting at the main peak (estimated to be at the desired oligomeric states based on the elution volume of ~12.5 mL on the S200 column) yielded homogeneous protein particles characterized by ns-EM. Proteins in the GDN detergent seemed to exhibit higher contrast and sharper contours on the ns-EM grid than in the DDM detergent (**Fig. 10**). Therefore, GDN was used in most cases throughout this study. When the ns-EM micrograph of CalC6_7 protein was compared to that of TMH4C4, both had a complex molecular weight of ~100 kDa and similar diameters across the protein model, their particles also looked similar in size, suggesting that CalC6_7 was folding and assembling correctly as designed (**Fig. 11**).

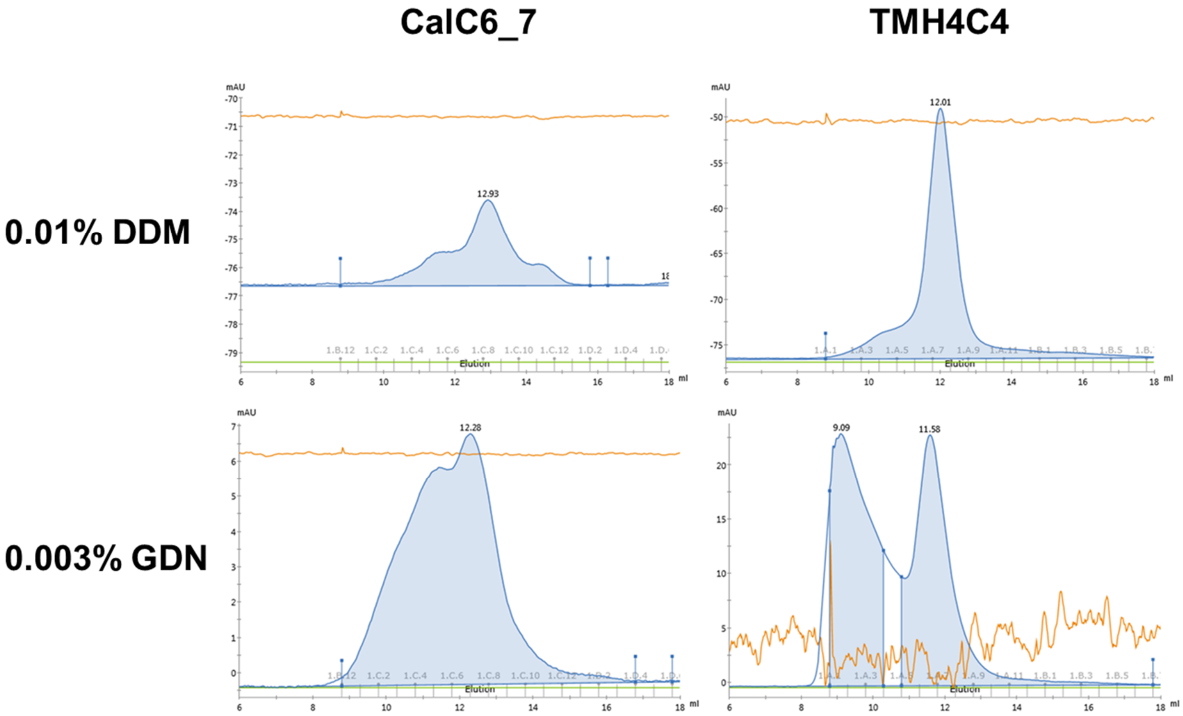

Fig. 9: SEC elution profiles on an S200 column of CalC6_7 and TMH4C4 in DDM and GDN detergents, respectively.

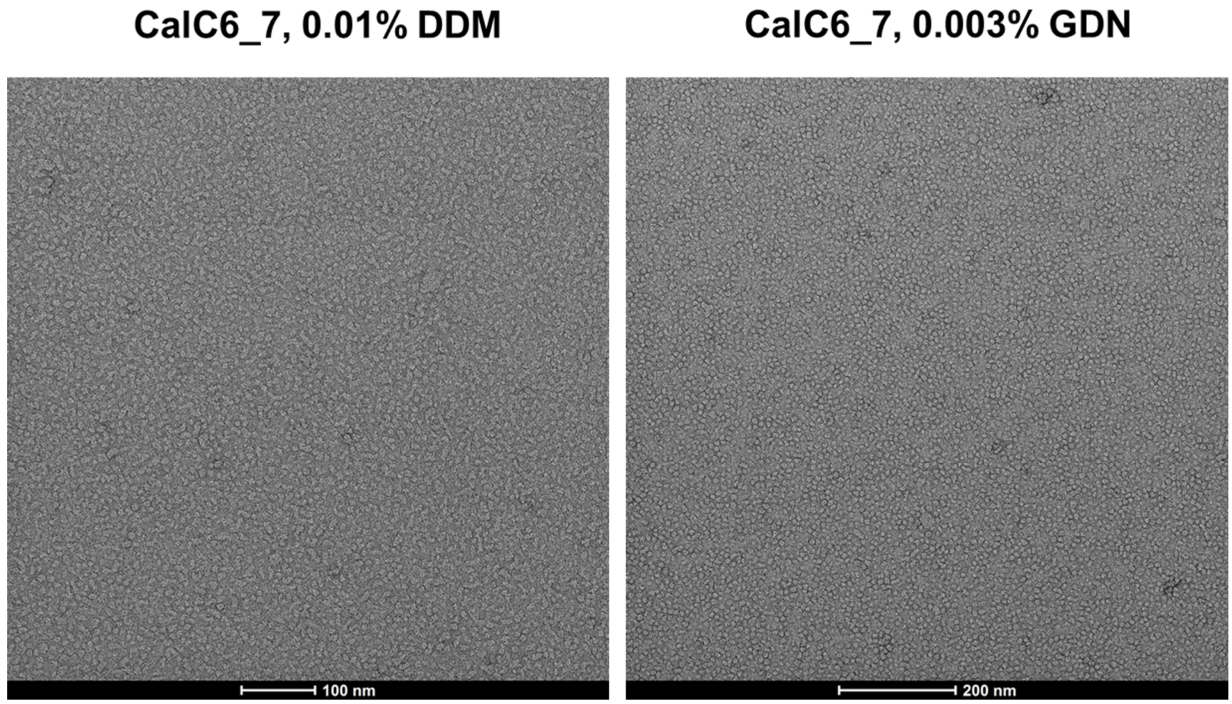

Fig. 10: ns-EM micrographs of the CalC6_7 design in different detergents (DDM and GDN).

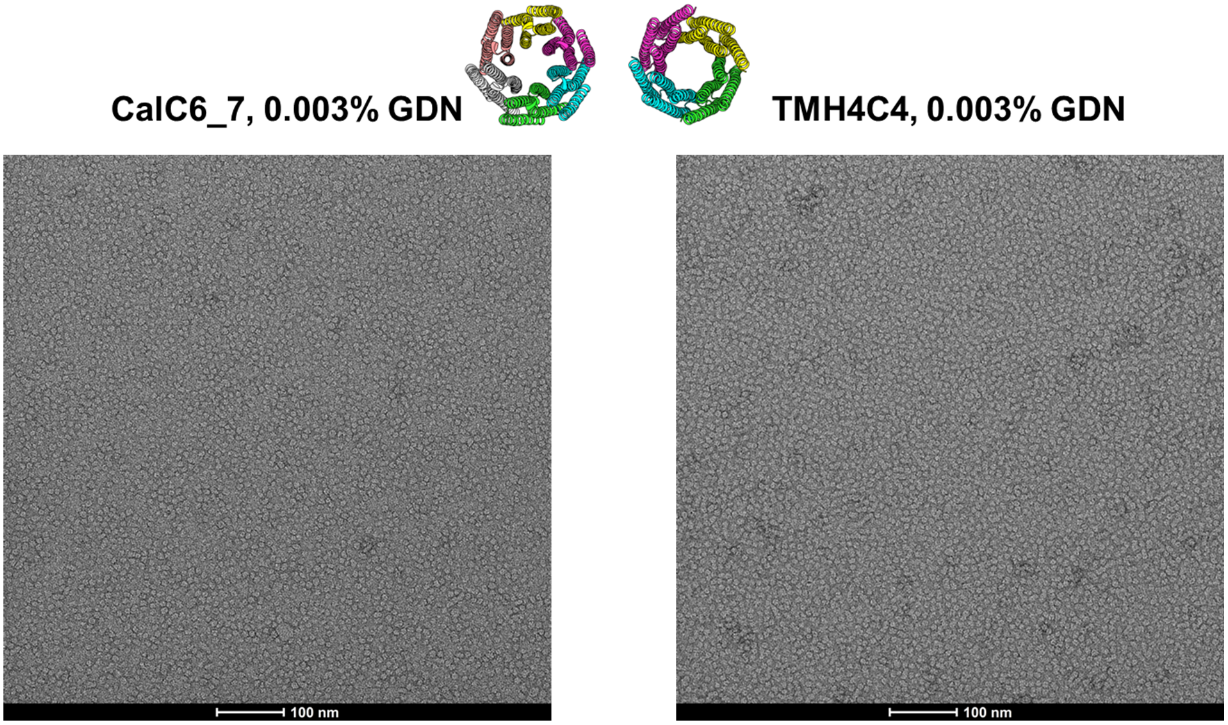

Fig. 11: ns-EM micrographs of CalC6_7 and TMHC4C4, with protein models displayed and compared in parallel.

We further proceeded with purifying and characterizing the other designs. Overall, 3, 2 and 4 designs in CalC4, CalC6 and CalC6_H series, respectively, were observed to elute as desired oligomeric states from SEC and form pore-containing particles on the ns-EM grids (**Fig. 12 and 13**). For these designs, the peak elution fraction on SEC (~ 12.5 mL) yielded homogeneous protein particles of ~8 nm in diameter evident in ns-EM micrographs and 2D class averages, consistent with the design models.

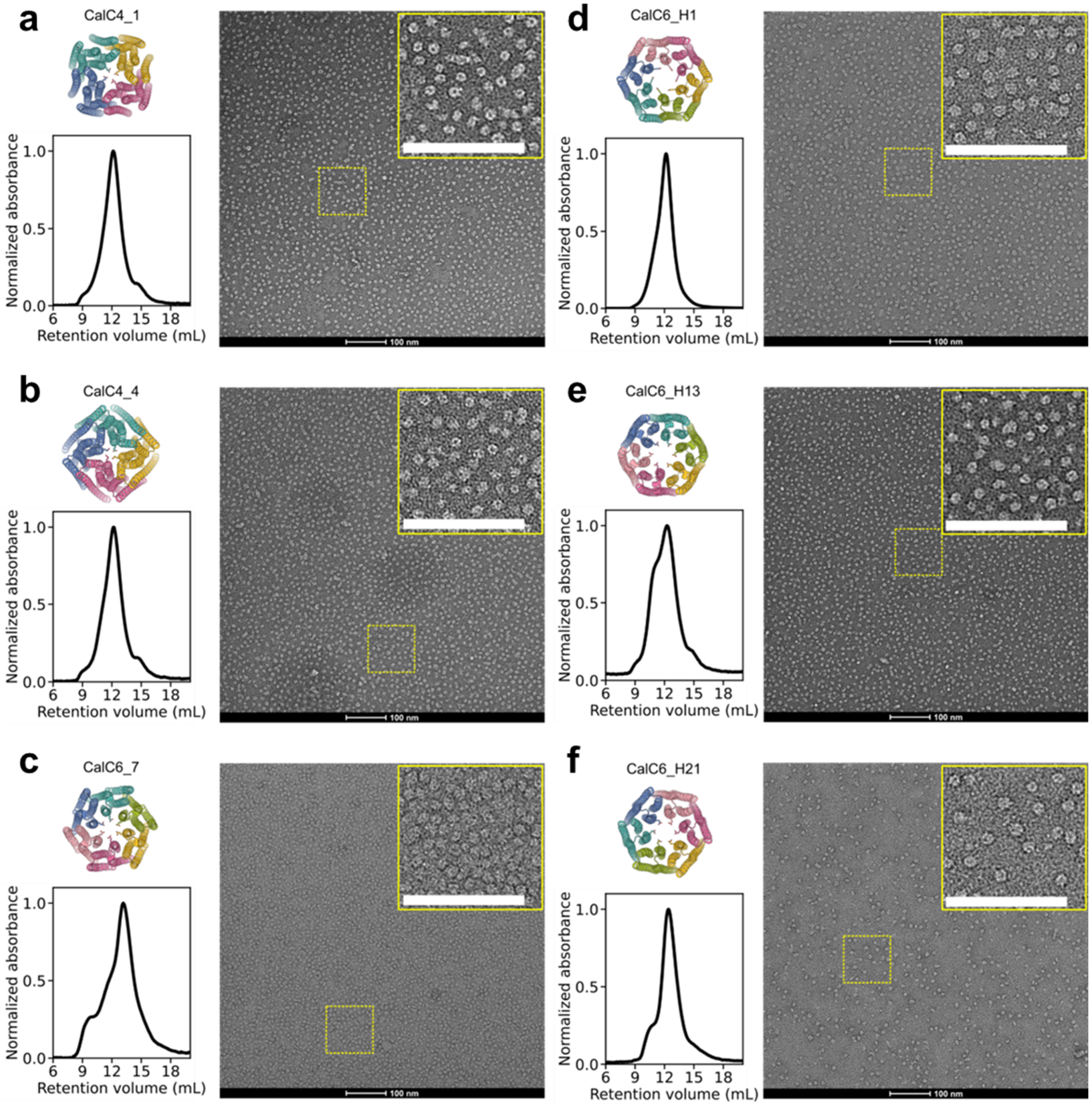

Fig. 12: Biophysical characterizations of additional designed channels. In addition to the designs shown in **Fig. 13** below, two CalC4 designs, CalC4_1 **(a)** and CalC4_4 **(b)**, one CalC6 design, CalC6_7 **(c)**, and three CalC6_H designs, CalC6_H1 **(d)**, CalC6_H13 **(e)**, and CalC6_H21 **(f)**, were observed to elute as desired oligomeric states from SEC and assemble into homogeneous pore-containing particles on the ns-EM grids. The close-up views shown on the upper right corners of the ns-EM micrographs corresponded to the regions highlighted by the dashed yellow frames. Scale bars, 100 nm.

Among these designs, CalC4_24, CalC6_3 and CalC6_H4 yielded the most homogeneous protein particles in each design group when imaged by electron microscopy (**Fig. 13**). CalC4_24 contains a constriction of ~1 Å in radius lined by four Glu residues, CalC6_3 contains a constriction of ~3 Å lined by six Glu residues, and in CalC6_H4, six Glu residues are placed at ~7 Å. These results demonstrated the general applicability of the design approach to generate transmembrane proteins upon pores with varying amino acid identities and selectivity filter geometries.

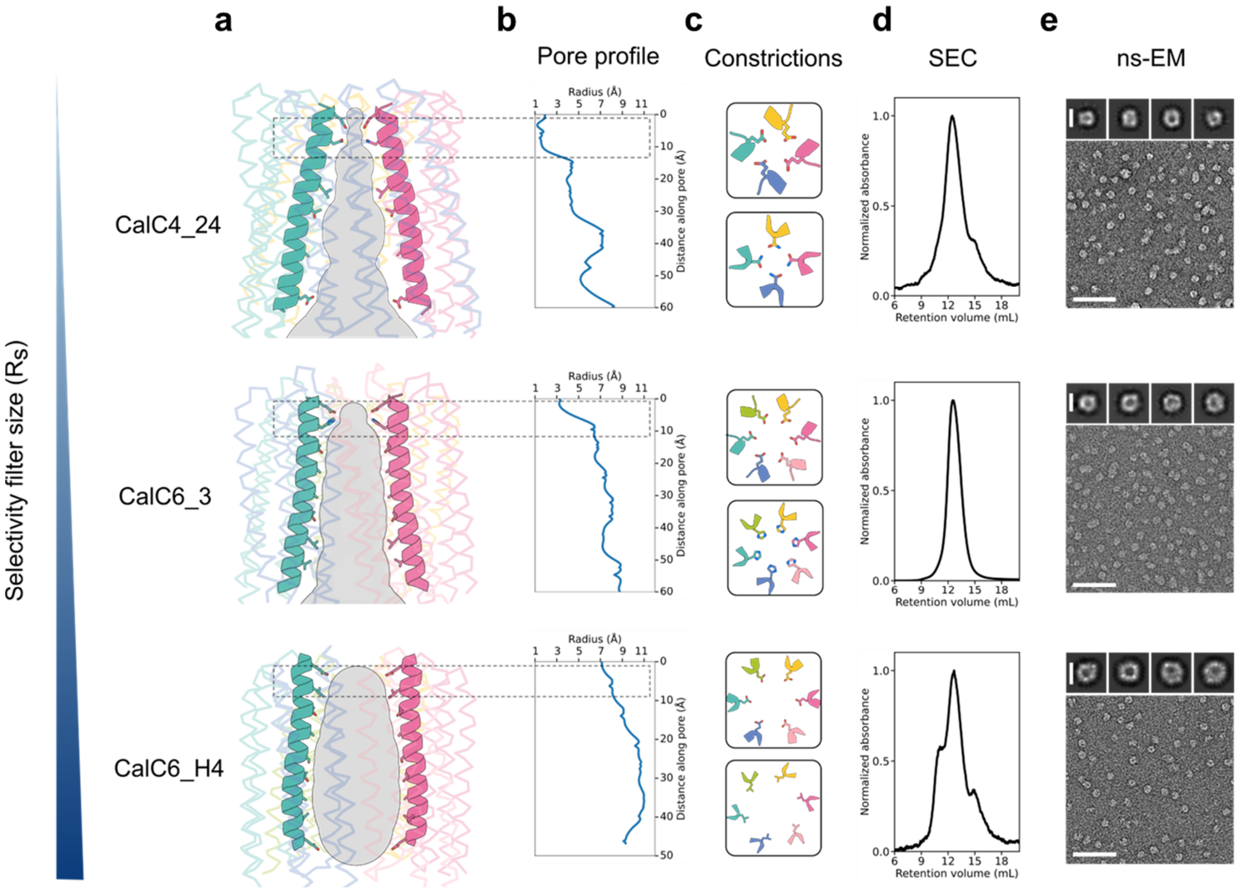

Fig. 13: Biophysical characterization of designed Ca^{2+} channels. a, Side views of the designed Ca^{2+} channels. Ion permeation pathway (calculated using MOLEonline) and the pore-lining helices on two opposing chains are highlighted, with the remainder of the channels rendered in transparency for clarity. **b,** Pore radius profiles representing the ion permeation pathways in **(a)**. **c,** Top views of the constrictions formed by the sidechains of the residues on two consecutive helical turns. The constrictions are located at the pore entrance, shown by the dashed frame in **(a)** and **(b)**. **d,** Size-exclusion chromatography traces of the purified Ca^{2+} channels. **e,** Representative ns-EM micrographs (scale bars, 50 nm) and 2D class averages (scale bars, 8 nm) of the designed channels.

Note that for almost all designs, an aggregation peak was present when the protein samples were first applied to the SEC column. This was not uncommon for transmembrane proteins and was largely due to the suboptimal choice of detergent.

Optimizing the detergent or even lipid nanodisc compositions for each individual design is practically too labor-intensive. We took a strategy to only take the later portion of the elution peak that was estimated to contain proteins in the desired oligomeric states and load on the SEC column for a second time. By doing this it allowed us to separate the target protein species from the aggregates for EM analysis as the second SEC profiles exhibited a much sharper elution peak (**Fig. 14**). In addition, since the elution peaks from the second SEC run for these proteins were largely monodisperse, this indicated that the fractions that were discarded in the first SEC run were more likely to be aggregates rather than off-target assemblies; otherwise these fractions eluting earlier than the main elution peak would have also appeared in the second SEC run as a result of equilibrium between different protein oligomeric states.

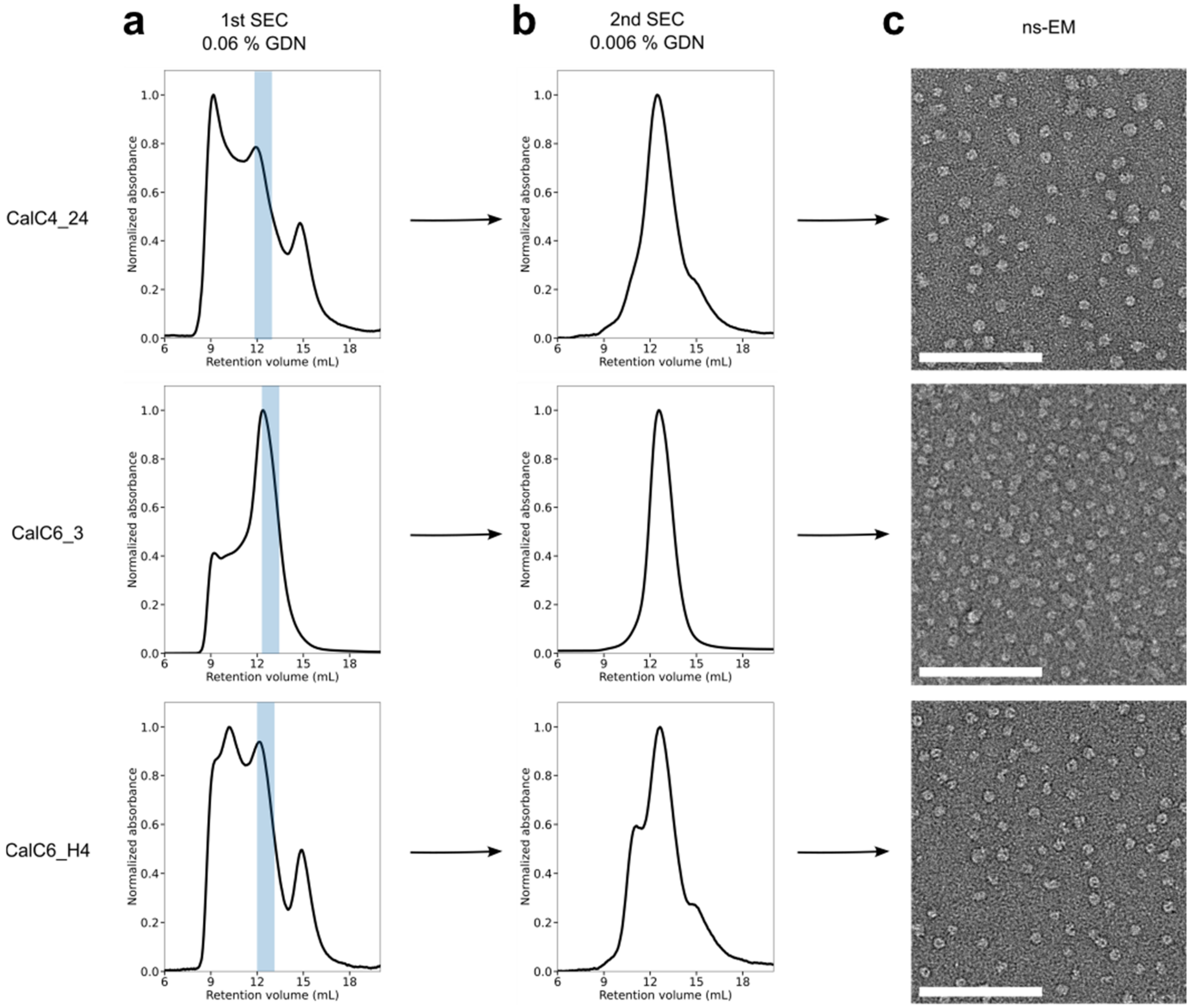

Fig. 14: Illustration of the purification strategy for separating the target protein species with the desired oligomeric states from aggregates. The three designs (CalC4_24, CalC6_3 and CalC6_H4), which were previously shown in Fig. 2, were presented here as examples (top, middle and bottom, respectively). From the first SEC run in the buffer containing 0.06% GDN **(a)**, only the latter portions (blue regions) were taken and were subject to the second SEC run in the buffer containing 0.006% GDN **(b,** also shown in **Fig. 13d)**. Protein samples taken from the more distinct elution peaks were observed to form homogeneous pore-containing particles on ns-EM grids **(c)**. Scale bars, 100 nm.

To characterize the stability of the designed proteins, circular dichroism (CD) spectroscopy and CD temperature melting experiments were performed on the purified proteins. For each design group, CalC4_24, CalC6_3, and CalC6_H4 were selected respectively as a representative design to characterize. The CD wavelength-scan spectra showed characteristic alpha-helix spectra for all three designs; CD melting experiments suggested these designs did not unfold at 95 °C (**Fig. 15**). These results indicated that the designed channels were highly stable; by comparison native ion channels were notoriously unstable in vitro. Therefore, these designs provide ideal protein scaffolds for further robust engineering toward specific and custom applications that are generally not achievable using naturally existing ion channels.

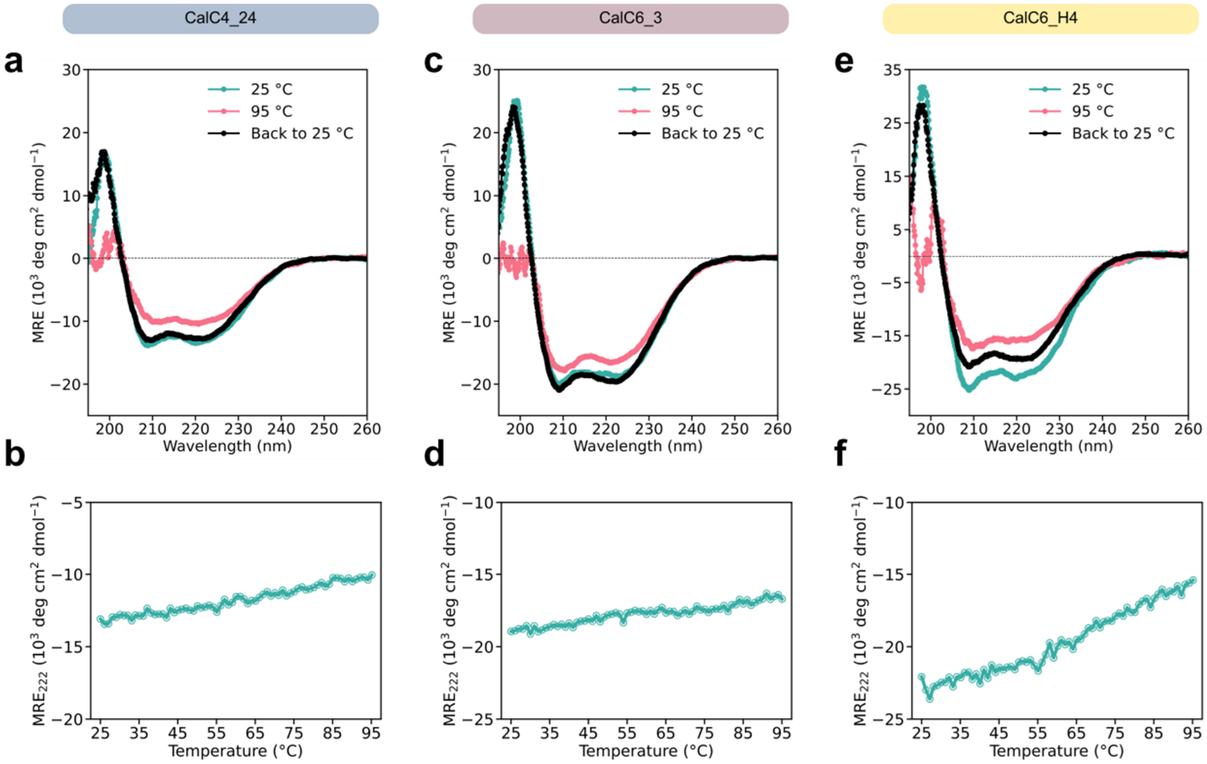

Fig. 15: Circular dichroism results of CalC4_24 (**a-b**), CalC6_3 (**c-d**), and CalC6_H4 (**e-f**). **a**, **c**, and **e**, CD spectra at 25 °C (cyan lines), 95 °C (red lines), and cooled back to 25 °C (black lines). **b**, **d**, and **f**, CD melting curves at 222 nm.

Another biophysical property of Ca^{2+} channels is to bind Ca^{2+} (and sometimes other multivalent ions such as Mg^{2+}) at the selectivity filter, with binding affinity ranging from nanomolar to micromolar ranges[31,62]. This was typically measured by titrating Ca^{2+} to block permeation of monovalent ions in cells using patch-clamp techniques. Experimental approaches for direct measurement of binding affinity using isothermal titration calorimetry (ITC) requires a large amount of protein, and the results might be influenced by the presence of other potential Ca^{2+}-binding sites on the proteins in addition to the Glu residues at the selectivity filter, as well as the detergent in the solution. We used AlphaFold3 (AF3)[45] to predict binding of divalent ions to the selectivity filter. The prediction results showed Ca^{2+} ions at the designed sites in CalC4_24 and CalC6_3, albeit with relatively low confidence levels (pLDDT less than 80, **Fig. 16**). The confidence level for Ca^{2+} in CalC4_24 was higher than that in CalC6_3, possibly due to the narrower size in the CalC4_24 selectivity filter. Mg^{2+} was also predicted to be present at the designed sites in both designs with a similar confidence level as Ca^{2+}. Multiple divalent ions were predicted to be present at the designed site of CalC6_3: this does not necessarily mean that these ions exist simultaneously but might suggest that binding of ions to CalC6_3 selectivity filter might happen in an asymmetrical manner via interactions with neighboring Glu residues where the ion was only partially dehydrated. We also noticed that the distance between the ion and the oxygen atom of the Glu sidechain reflected direct metal-ligand interactions (without consideration of water molecules). As a result, Mg^{2+} was predicted to be closer to the oxygen atoms than Ca^{2+}. This might suggest that AF3 is not aware of the role of water when it is predicting proteins binding to metal ions, which was somewhat expected given that the metal ions present in the protein structure files in the databases probably dominantly consist of proteins that tightly bind to metal ions through direct interactions.

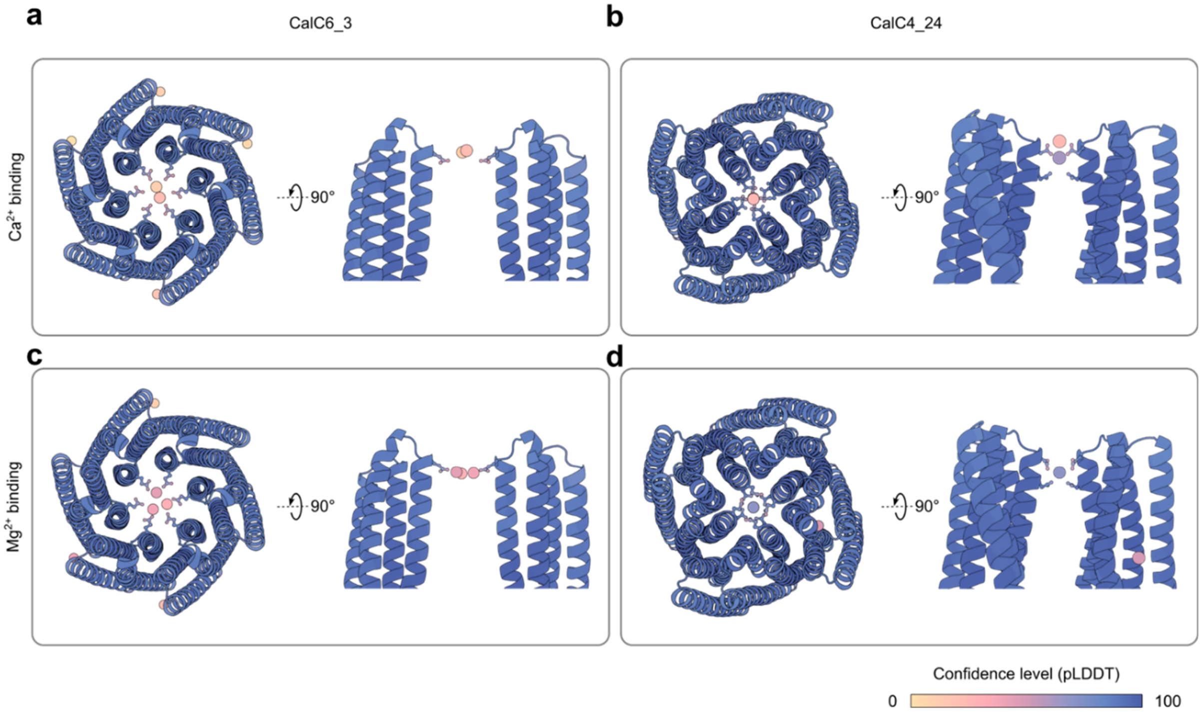

Fig. 16: AlphaFold3-predicted models of CalC6_3 and CalC4_24 binding divalent ions. a and **b**, Predicted binding of CalC6_3 and CalC4_24 to Ca^{2+}. **c** and **d**, Predicted binding of CalC6_3 and CalC4_24 to Mg^{2+}. The models were colored based on the confidence level (pLDDT) of the prediction results, with the color gradient shown on the bottom right.

3.4. Characterization of designed channel in cells by whole-cell patch-clamp experiments

Next we sought to investigate the conductance of the designed channels for Ca^{2+} by whole-cell patch-clamp recordings in the insect *Trichoplusia ni* cells (Hi5). This insect cell line was used together with the Bac-to-Bac baculovirus expression system due to the readiness of identifying infected cells based on the changes in the cell morphology (while this morphological change does not occur in another insect cell line, SF9 cells, that is used for generating the baculovirus). By comparison, the commonly used mammalian cell lines, such as HEK293T cells, require incorporation of a reporter protein, typically a fluorescent protein that is expressed bicistronically with or fused to the target protein, for locating the cell of interest to patch under the microscope. This needs further construct optimization to avoid impact of the reporter protein on the folding and function of the designed channel. After obtaining the viruses encoding the designed proteins, a western blot analysis was performed to examine the expression of proteins in the Hi5 cells, as well as to determine the optimal amount of virus to use for the patch-clamp experiment. This was because a balance between the protein expression level (more virus leads to higher protein expression levels) and the cell viability (too much virus leads to fragile cells easily detaching from the patch pipette) would need to be found in favor of reliable electrophysiological recordings. Cells harvested 48 hours post infection showed that CalC6_3 and CalC4_24 expressed at a similar level. Usually patch-clamp experiments were performed within 24 hours since infection, the protein expression levels of CalC6_3 and CalC4_24 were also compared by western blot using cell lysates harvested 24 hours post infection. At this point there was not much protein expression. As a result, a much longer exposure time was required when imaging the chemiluminescence on the membrane. The virus encoding CalC6_3 seemed to have a lower titer than that encoding CalC4_24, as the protein expression level of CalC6_3 using 100 µL virus was significantly higher than using 5 µL virus; by comparison, there was not much difference between using 5 µL virus and 100 µL virus for CalC4_24 (**Fig. 17**). Therefore, more viruses were used for CalC6_3 than for CalC4_24 when patch-clamp experiment is performed.

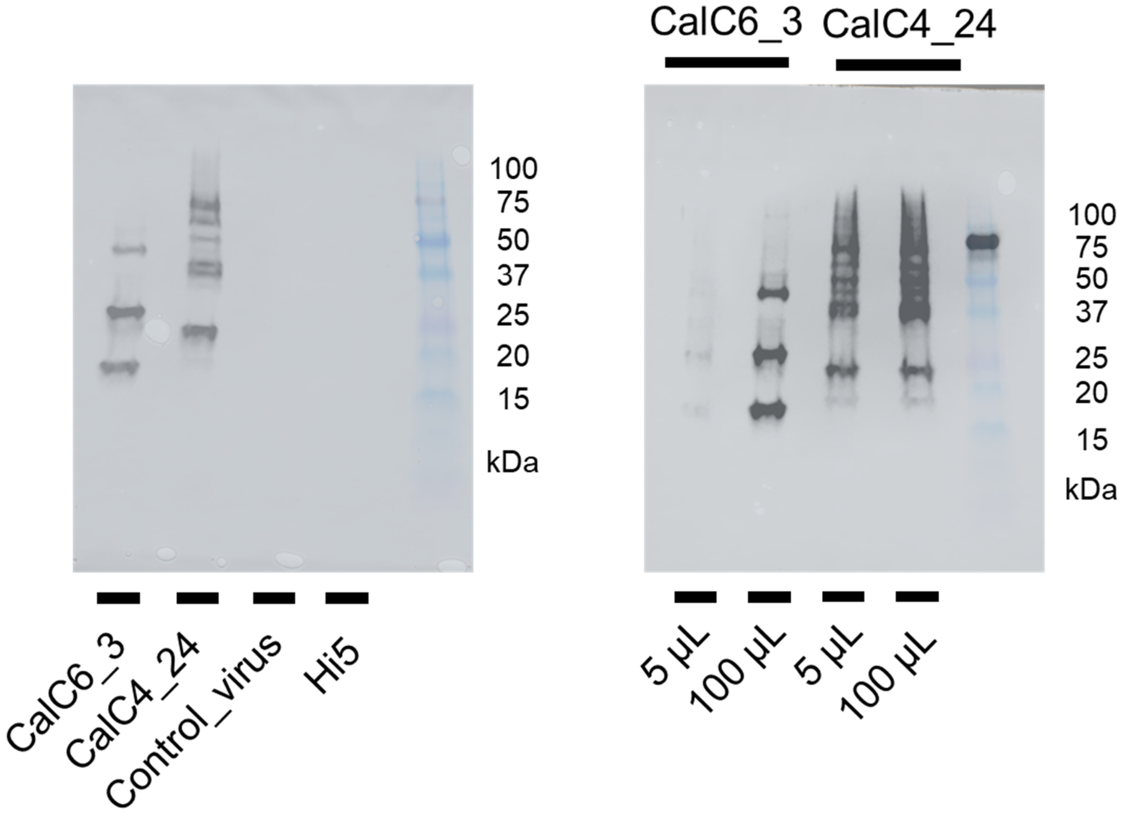

Fig. 17: Western blot analysis of Hi5 cell lysates after infection. The left blot showed the results using cells harvested 48 hours after infection. The right blot showed the results using cells harvested 24 hours after infection.

An experimental challenge is to subtract the background currents from the ionic currents for the designed (and constitutively open) channels. If a patched cell is treated as an electrical circuit as the Hodgkin-Huxley model does, the lipid bilayer and all ion-permeable pathways can be represented as a parallel circuit, where the lipid bilayer is represented as a capacitor and the ion-permeable pathways can be represented as resistors (**Fig. 18**). The cell membrane capacitive current can be compensated by the amplifier. However, when a voltage is applied across the membrane, any component (channels, pores, pumps, breach of cell membrane, etc.) that is permeable to any conducting species (both cations and anions) can contribute to the overall measured current. Two most significant current contaminations are (1) the leak between the glass patch pipette and the cell membrane (imperfect seals), and (2) all other channels present in the cells. For native ion channels, specific techniques can be used to separate the background currents because those channels are gated. For example, for voltage-gated ion channels it is known that the channel of interest is closed in specific voltage ranges, and thereby a series of voltages can be applied in that range to obtain the I-V relations of the background current that is subsequently subtracted from the measured current; and for ligand-gated ion channels, the background current can be defined by addition of agonist or antagonist that specifically acts on the channel. By comparison, it is challenging to distinguish the currents through the designed constitutively open channels from the background currents, as the status of the channels (i.e., open or closed) is unclear.

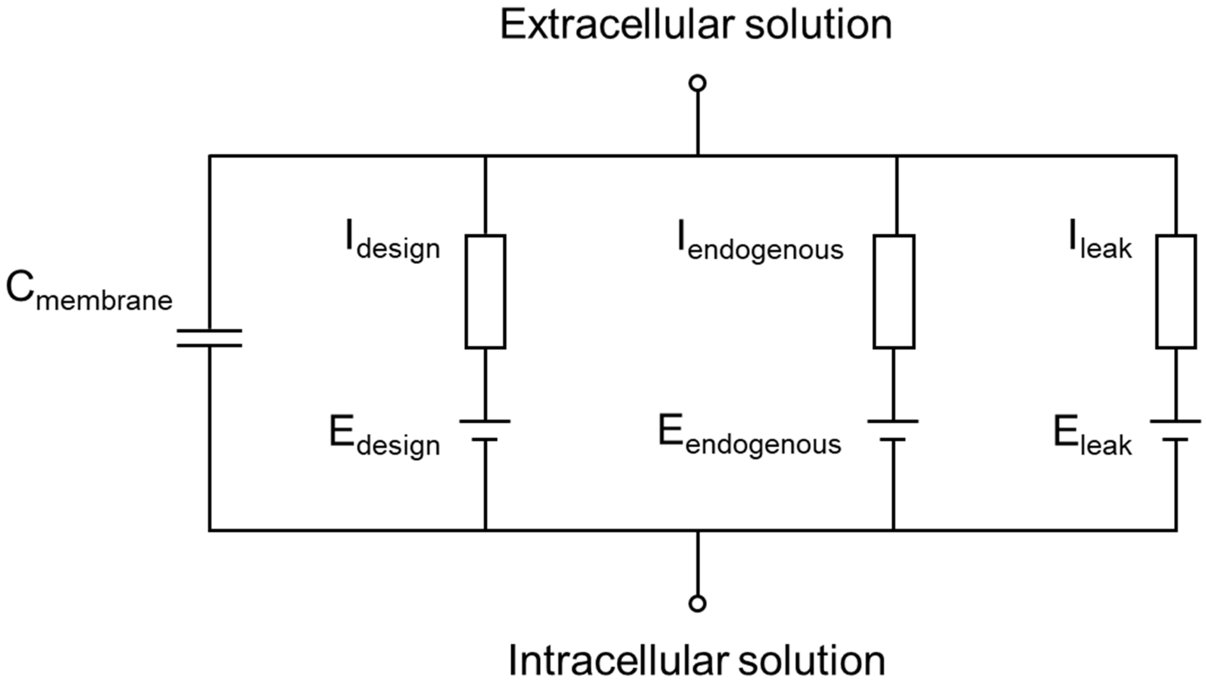

Fig. 18: A modified scheme of Hodgkin-Huxley model. I_{design}, $I_{endogenous}$, and I_{leak} represent the current conducted by the designed channel, the endogenous channel, and the leak from the cell membrane, respectively. E_{design}, $E_{endogenous}$, and E_{leak} represent the electrochemical driving force for the designed channel, the endogenous channel, and the leak, respectively. $C_{membrane}$ represents the lipid bilayer of the cell membrane as a capacitor.

To minimize the impact of these background currents that were not specific to the designed channels, we used N-methyl-D-glucamine ($NMDG^+$) to replace all inorganic cations in both extracellular and intracellular solutions and only added Ca^{2+} to the extracellular side. A voltage-step protocol was applied to record the whole-cell current in response to the voltage stimuli from –100 to +100 mV at 10 mV increments. The extracellular solution was changed from one with no Ca^{2+} (1 mM EGTA) to those with 0.2 mM, 2 mM and 10 mM Ca^{2+}, respectively, to investigate whether the measured currents were specific to Ca^{2+}. Indeed, the inward currents gradually increased with the concentration of Ca^{2+}. The current-voltage (I-V) relations obtained from the voltage step protocol showed that the current rectified in the inward direction (**Fig. 19**). This was expected based on the experimental settings because Ca^{2+} was only present in the extracellular side. It was also observed that the current at –100 mV did not increase in proportion to the fivefold increase in the Ca^{2+} concentration (from 2 mM to 10 mM); instead, there was only about a twofold increase in the measured current. This saturation effect has also been reported for some native Ca^{2+} channels and is thought to result from Ca^{2+} binding inside the channel, such that Ca^{2+} permeation through the channel could be viewed as reversible Ca^{2+} binding at the selectivity filter followed by rapid release through the pore, and therefore can be modelled using Michaelis-Menten (MM) equation. The saturation in current represents the saturation of Ca^{2+} binding (equivalent to the K_M value in the MM equation). Overall, these electrophysiological features indicated that the designed channels showed some typical features as would be expected for a Ca^{2+} channel. A leak current (as a result of a bad membrane seal) would not likely manifest in a similar manner.

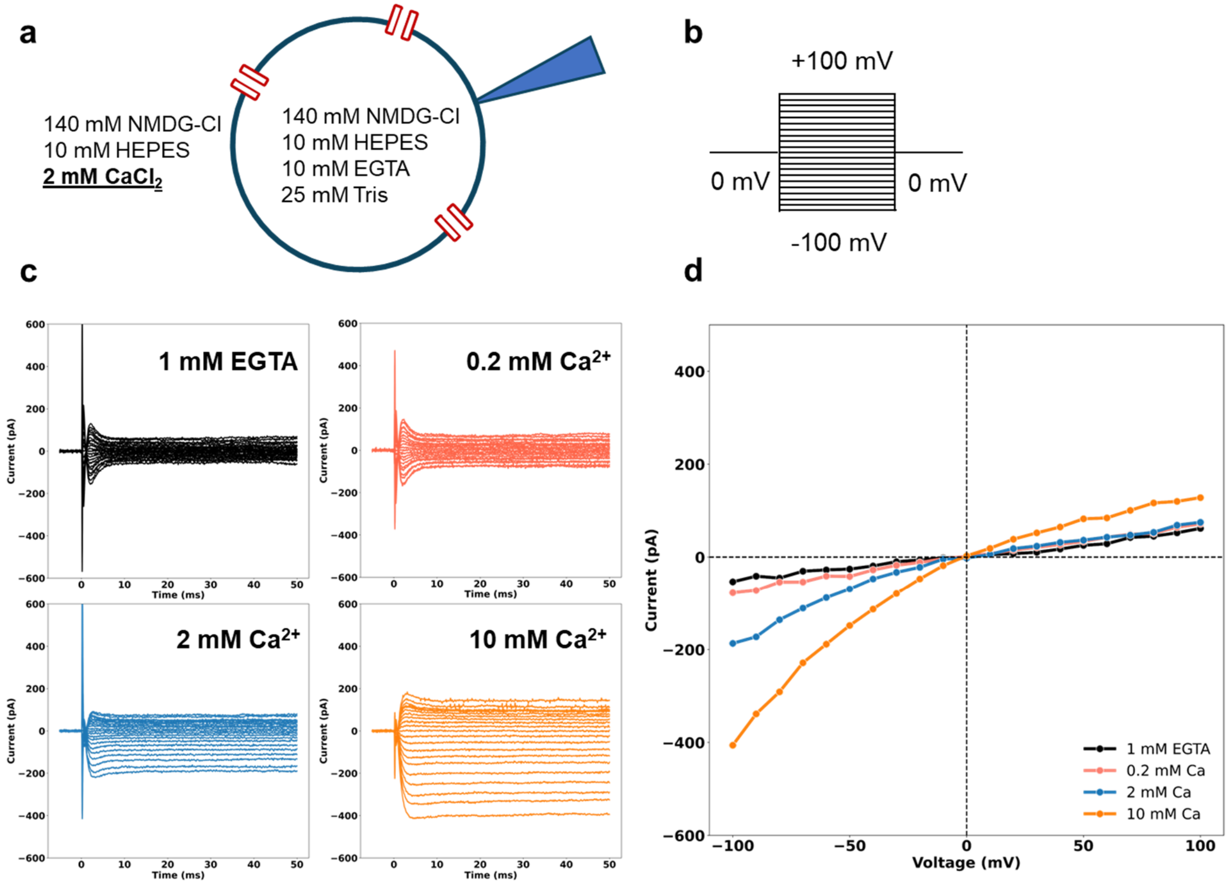

Fig. 19: Characterization of Ca^{2+} permeability of designed channels by whole-cell patch-clamp technique. a, Diagram showing the solutions used for whole-cell patch-clamp recordings. **b,** The schematic illustration of the voltage step protocol. **c,** Currents elicited by the voltage step protocol recorded on cells expressing the CalC6_3 design in solutions with 1 mM EGTA, 0.2 mM Ca^{2+}, 2 mM Ca^{2+}, and 10 mM Ca^{2+}, respectively. **d,** I-V relations obtained from **(c)**.

To further investigate the ion selectivity of the channels, the bath solution was changed to contain Na^+ for measuring conductance for Na^+ as Na^+ is the main competing ion against Ca^{2+} in physiological conditions. Ca^{2+} was also present in the solution since the mechanism of how Ca^{2+} channels achieve selectivity depends on binding of Ca^{2+} at the selectivity filter. Using the same voltage step protocol as that for measuring Ca^{2+} currents, the addition of Na^+ to the bath solution was found to result in an increase in the inward current (**Fig. 20**). Interestingly when 30 mM Na^+ was added to the 2 mM $[Ca^{2+}]$ solution, the current amplitude at –100 mV did not increase significantly, suggesting that Ca^{2+} was probably more permeable than Na^+ through the channel. When this Na^+ titration measurement was carried out with the 10 mM $[Ca^{2+}]$ solution (**Fig. 21**), the inward current even decreased after 30 mM Na^+ was added, and subsequently increased to the extent that was slightly higher than the current measured in 10 mM $[Ca^{2+}]$ alone. A similar phenomenon known as "anomalous mole fraction effect" might be related to the results observed here: the current measured for voltage-gated calcium channels in 10 mM $[Ba^{2+}]$ was higher than that measured in 10 mM $[Ca^{2+}]$, both higher than that measured in 3 mM $[Ca^{2+}]$ and 7 mM $[Ba^{2+}]$[63–65]. This effect could possibly be interpreted as preferential binding of ions inside the pore, also suggesting that the designed channel had a higher binding affinity for Ca^{2+} than for Na^+. This was expected because multiple carboxylates would bind Ca^{2+} with a much higher affinity than Na^+, consistent with the design principle.

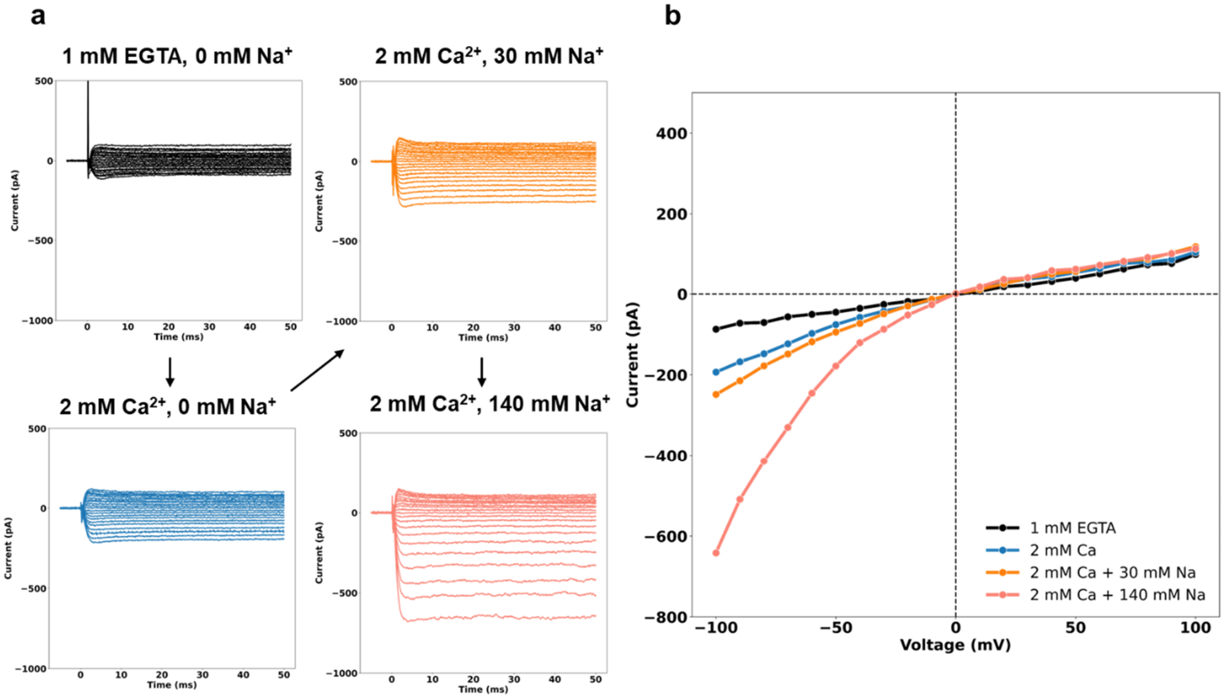

Fig. 20: Characterization of Ca^{2+} permeability versus Na^+ permeabilities of designed channels. a, Currents elicited by the voltage step protocol recorded on cells expressing the CalC6_3 design in solutions with 1 mM EGTA, 2 mM Ca^{2+}, 2 mM Ca^{2+}/30 mM Na^+, and 2 mM Ca^{2+}/140 mM Na^+, respectively. **b,** I-V relations obtained from **(a)**.

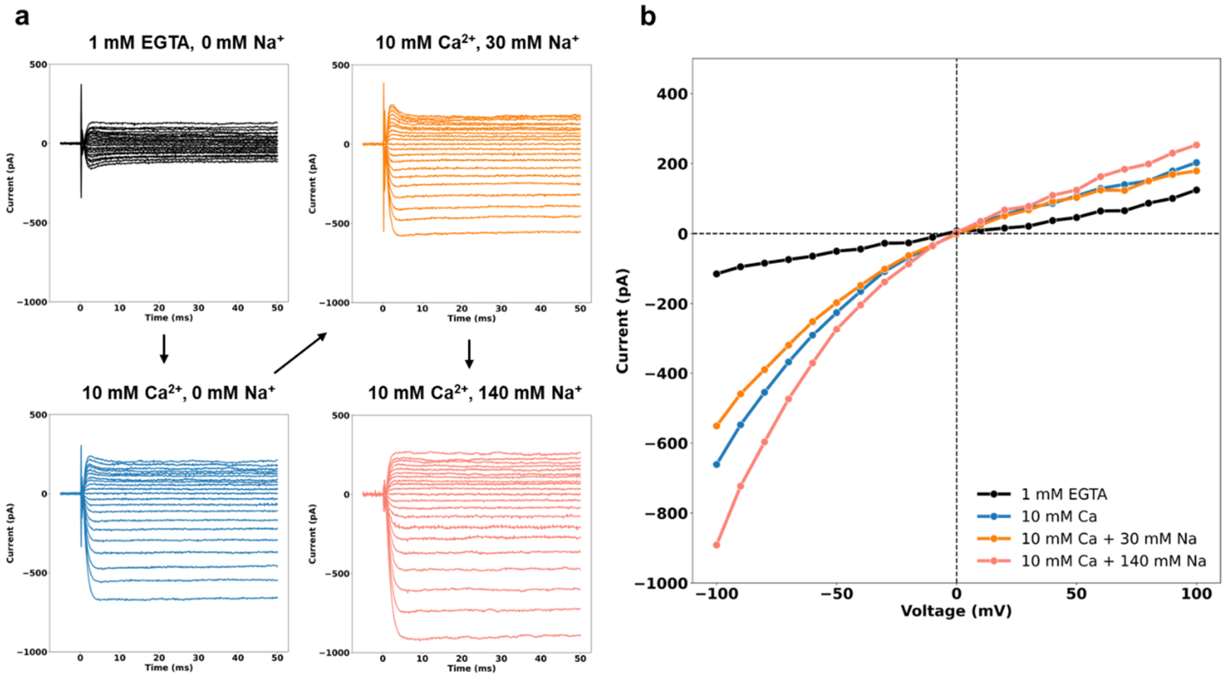

Fig. 21: Characterization of Ca^{2+} permeability versus Na^{+} permeabilities of designed channels with higher [Ca^{2+}] in the extracellular buffer. a, Currents elicited by the voltage step protocol recorded on cells expressing the CalC6_3 design in solutions with 1 mM EGTA, 10 mM Ca^{2+}, 10 mM Ca^{2+}/30 mM Na^{+}, and 10 mM Ca^{2+}/140 mM Na^{+}, respectively. **b,** I-V relations obtained from **(a)**.

Some questions arose despite these promising results. Why would there be outward currents since there was not conductive species in the intracellular solution? Was that related to the leak from the seal, or it was because some ions had already diffused along the concentration gradient through the channel into the cell? Given that it took about more than 30 seconds to conduct a complete voltage step protocol (2s interval time with 21 sweeps), could there be differences in the ion concentrations between the start and end voltage step protocol, resulting in a change in the measured currents? In the voltage step protocol by default currents evoked at different voltages were compared to that at 0 mV

– in real situations was it possible that current at 0 mV also changed given the huge concentration differences of ions of interest at both sides of the cells?

To address these questions, we replaced the Cl^- with methanesulfonate ($MeSO_3^-$) to minimize the effects of Cl^- on the experiments (5 – 10 mM Cl^- is still required for the electrode potential of the Ag/AgCl electrode to be stable), and changed the voltage step protocol to a voltage ramp protocol with the automatic zero-offset function turned off in PatchMaster Next software. Because the liquid junction potentials between the extracellular and intracellular solutions were calculated to be less than 1 mV (https://swharden.com/LJPcalc/), once the offsets between the electrodes were corrected when both electrodes were immersed in solutions, no additional voltage offset was required to compensate for the command voltage. Using the improved experimental methods, we could directly obtain the I-V relations within 1 second and observed the change in zero-current (reversal) potential during solution exchanges. When this was applied to recording the cells expressing two different designed channels, we could observe both increase of inward currents and a shift of reversal potential to the positive voltage direction when cations were added to the extracellular side (**Fig. 22**). When Ca^{2+} was removed from the solution, leaving 140 mM Na^+ as the only present cation, there was an additional shift of reversal potential to the positive direction, suggesting a role of Ca^{2+} binding during ion permeation: without Ca^{2+} binding that prevented Na^+ permeation to some extent, a more positive voltage was required to reverse the direction of the currents. Both tested designs showed this trend in a similar manner, while the increase of inward current and the extent of the positive shift of the reversal potential showed differences, suggesting different permeability ratio of Ca^{2+} versus Na^+.

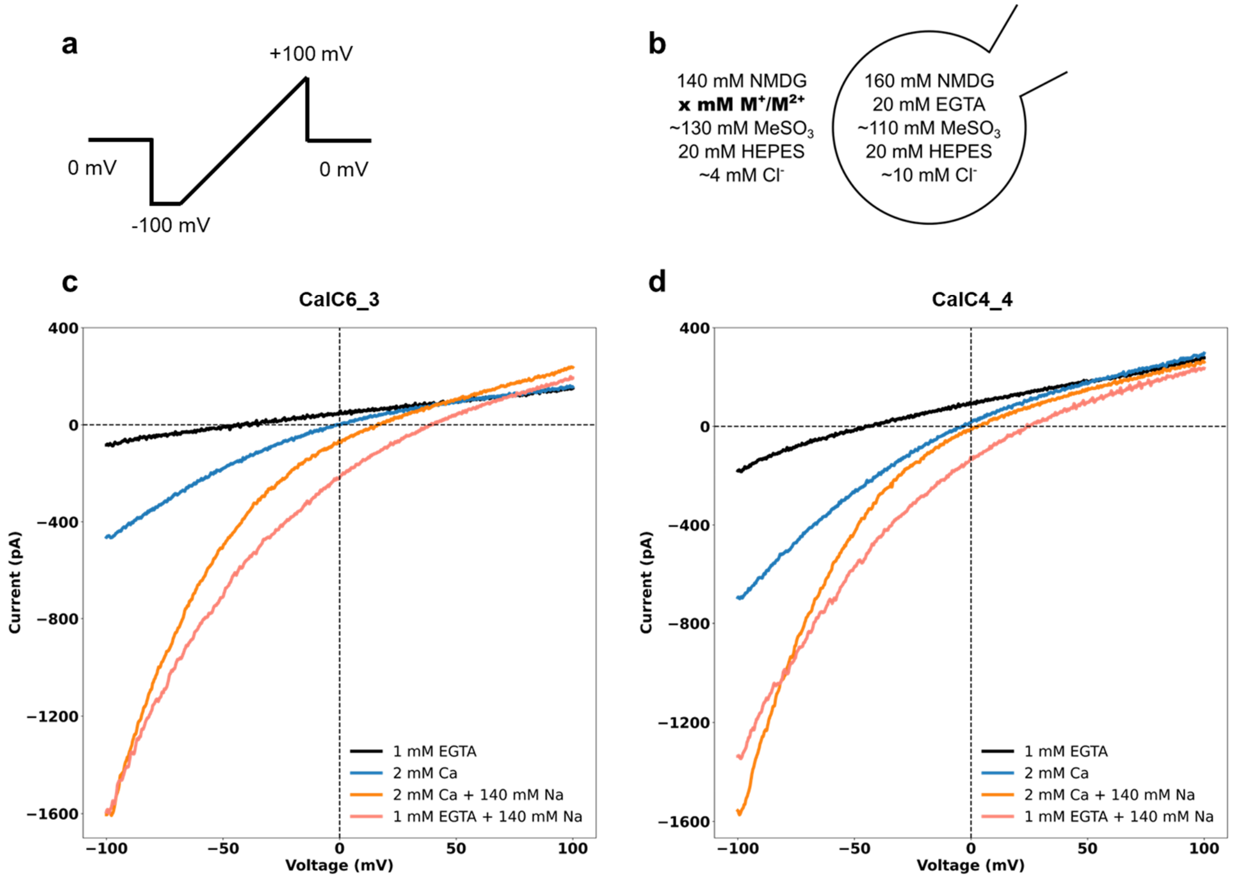

Fig. 22: Whole-cell patch-clamp experiments using the ramp protocol (a) and recording solutions with decreased $[Cl^-]$ (b). M^+/M^{2+} denoted cations with a valence of one and two, respectively. **c** and **d**, I-V relations obtained from the voltage ramp protocol in solutions with 1 mM EGTA, 2 mM Ca^{2+}, 2 mM Ca^{2+}/140 mM Na^+, and 1 mM EGTA/140 mM Na^+, respectively.

In native Ca^{2+} channels, removal of Ca^{2+} from the extracellular solution often resulted in a significant increase of inward current that was conducted by Na^+ as well[33]. Why was this not observed in our designed channels? Could there be another endogenous cation channel that was consistently contributing to the measured I-V relations? To investigate how the recording would appear for the Hi5 cells alone, we made an empty pFastBac Dual vector by removing the DNA sequences encoding the designs and prepared a control baculovirus from this empty construct as a negative control. Whole-cell patch-clamp experiment was conducted on cells infected with virus encoding the designs (two designs CalC6_3 and CalC4_24 were used) and the control virus in parallel. A Ca^{2+} titration experiment was conducted first to investigate the Ca^{2+} current of the endogenous channel (negative control). The cells infected with the control virus also exhibited Ca^{2+} conductance when Ca^{2+} was present in the bath solution (**Fig. 23**). Although the amplitude of inward currents of the negative control seemed significantly smaller than both designs, it would have a significant effect on the reversal potential. This is because the reversal potential is largely dependent on the concentrations of specific ions that are permeable across the cell membrane, and therefore the promiscuous endogenous channel would have a similar effect on the reversal potential as the designed channel. This existent activity of the endogenous channels made it even more impractical to quantify the relative permeabilities of ions for our designs using the Goldman-Hodgkin-Katz (GHK) voltage equation: typically, two ions with known concentrations were put on the extracellular and intracellular sides, respectively, and the permeability ratio of two different ions were calculated from the reversal potential upon the channel opening. As discussed above, in our case this is complicated by the concentration gradient-driven diffusion through the open channels, which results in variation in the ion concentrations, and the contribution of endogenous channels to the reversal potential is difficult to disentangle.

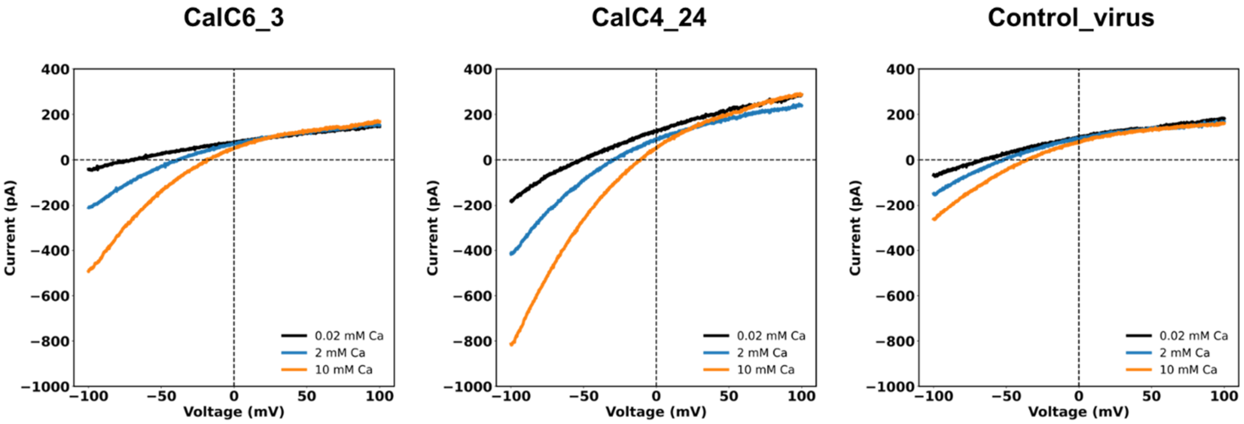

Fig. 23: I-V relations obtained from the –100 mV to +100 mV voltage ramp protocol. Recordings were obtained in solutions with 1 mM EGTA, 2 mM Ca^{2+} and 10 mM Ca^{2+} on cells infected with virus encoding the design CalC6_3, CalC4_24, and the control virus, respectively.

To further investigate the ion selectivity of the promiscuous endogenous channel and ultimately to answer whether it would affect the determination of ion selectivity of our designed channels, we measured the currents in solutions containing different ions on cells infected with the design virus and control virus in a back-to-back manner. Native Ca^{2+} channels often allow permeation of Ba^{2+}, Sr^{2+} but not Mg^{2+}, while this property is often not observed for K^+ or Na^+ channels. We conducted current measurement on cells in 10 mM [Ba^{2+}], 10 mM [Sr^{2+}], 10 mM [Ca^{2+}], and 10 mM [Mg^{2+}], respectively, and monitored the time courses during solution exchange. The background current was determined in a 0.02 mM [Ca^{2+}] solution instead of 1 mM [EGTA] to avoid damaging the cell membrane, facilitating prolonged recordings in different solutions on the same cell. Increase of inward currents was observed in all solutions containing the divalent ions of interest. Currents obtained in 10 mM [Ca^{2+}] were larger than in other divalent ions (**Fig. 24**). Interestingly, when the bath solution was changed to contain 10 mM Mg^{2+}, the increase of current was followed by a rapid decrease within several voltage sweeps (less than 30s). The perfusion of Mg^{2+} also seemed to cause an irreversible decrease of Ca currents as shown when the bath solution was changed to contain 10 mM Ca^{2+} at the end of the experiment. When this solution exchange experiment was conducted with 140 mM Na^+ using cells infected with the control virus, a significant increase in the inward current was observed (**Fig. 25**). This result was reproducible across different cells (thus not an artifact) regardless of the amplitude of the background leak current.

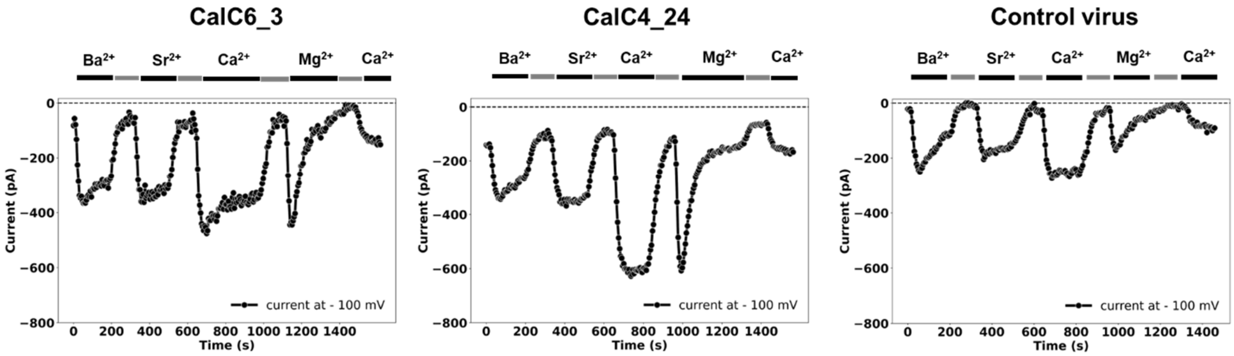

Fig. 24: Time courses of inward currents measured at –100 mV. Recordings were obtained in solutions with 10 mM Ba^{2+}, 10 mM Sr^{2+}, 10 mM Ca^{2+}, and 10 mM Mg^{2+} on cells infected with virus encoding the design CalC6_3, CalC4_24, and the control virus, respectively. Bath solution was switched to a 0.02 mM [Ca^{2+}] solution between exchanges into different divalent cations (indicated by gray bars).

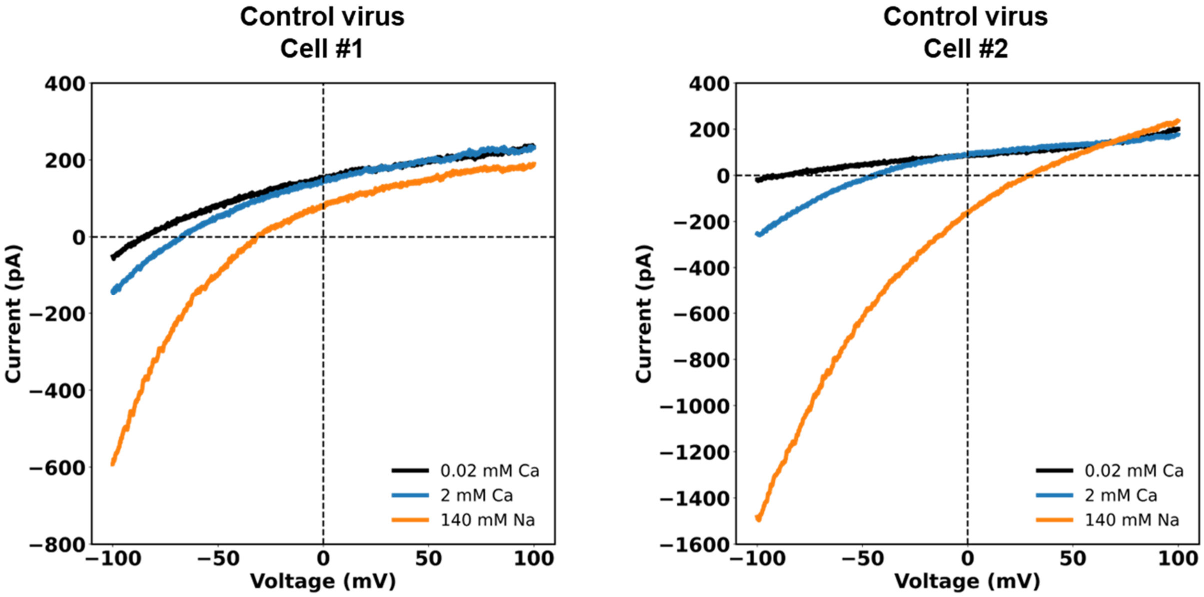

Fig. 25: I-V relations obtained from the –100 mV to +100 mV voltage ramp protocol on cells infected with control virus. Recordings were obtained in solutions with 0.02 mM Ca^{2+}, 2 mM Ca^{2+} and 140 mM Na^{+}, respectively. The results shown here were obtained from two different cells independently.

With the study of the electrophysiological properties of the designed channels and the promiscuous endogenous channels in parallel, what could we conclude so far? First, the contribution of this endogenous current was non-negligible, especially when the current was measured in solutions containing Na^+. This was a non-selective cation current. Additional experimental approaches would be needed to reduce this endogenous current component. Second, given that the apparent measured current was an addition of that conducted by the designed channel and the endogenous channel, the designed channels probably had higher selectivity for Ca^{2+} than was previously assumed, since the endogenous channel contributed significantly to non-Ca^{2+} currents. Third, this endogenous current component was probably inhibited by entry of Mg^{2+} into the cells. If the Mg^{2+} inhibition happened extracellularly, there would not have been a sharp increase in the inward current at the first several voltage sweeps when the bath solution was changed to contain 10 mM Mg^{2+}.

To reduce the impact of this endogenous current, we first tried a pharmacological approach by including commonly used drugs in the patch pipette. Since Cl^- was always present in the recording solution though the concentration of it was kept constant in all perfused solutions, a potent chloride channel inhibitor niflumic acid (NFA) was tried to examine if chloride channel was (partially) causing the trouble. With 50 µM NFA in the patch pipette, the I-V relations measured in solutions containing 2 mM Ca^{2+} and 140 mM Na^+ still demonstrated the same trend for negative controls as that in the absence of NFA. Next, we looked for drugs that could inhibit native Ca^{2+} channels, since Ca^{2+} permeability was observed in the experiment. Ca^{2+} was well known to be tightly regulated in cells, so a Ca^{2+}-permeable pathway could be significantly contributing to the endogenous current. The electrophysiological features of the endogenous currents suggested that it unlikely belonged to a voltage-gated calcium channel (Ca_v) because these channels were closed at very negative membrane potentials, so they could not contribute to the currents at –100 mV. We focused on the TRP channels that probably constituted the main cation entry pathways in electrically non-excitable cells. We included a potent inhibitor against a broad range of TRP channels, 2-Aminoethoxydiphenyl borate (2-APB), in the patch pipette and conducted the patch-clamp experiment again, but significant inward currents at –100 mV were still observed in both 10 mM [Ca^{2+}] and 140 mM [Na^+] solution, suggesting that 2-

APB was not inhibiting the endogenous cation current in this case (**Fig. 26**). Probably the TRP channels that were inhibited by 2-APB were not playing a role in the endogenous currents. Alternatively, since the studies involving the usage of 2-APB were mostly conducted in the context of mammalian cells, it was also likely that 2-APB was not acting in these insect Hi5 cells.

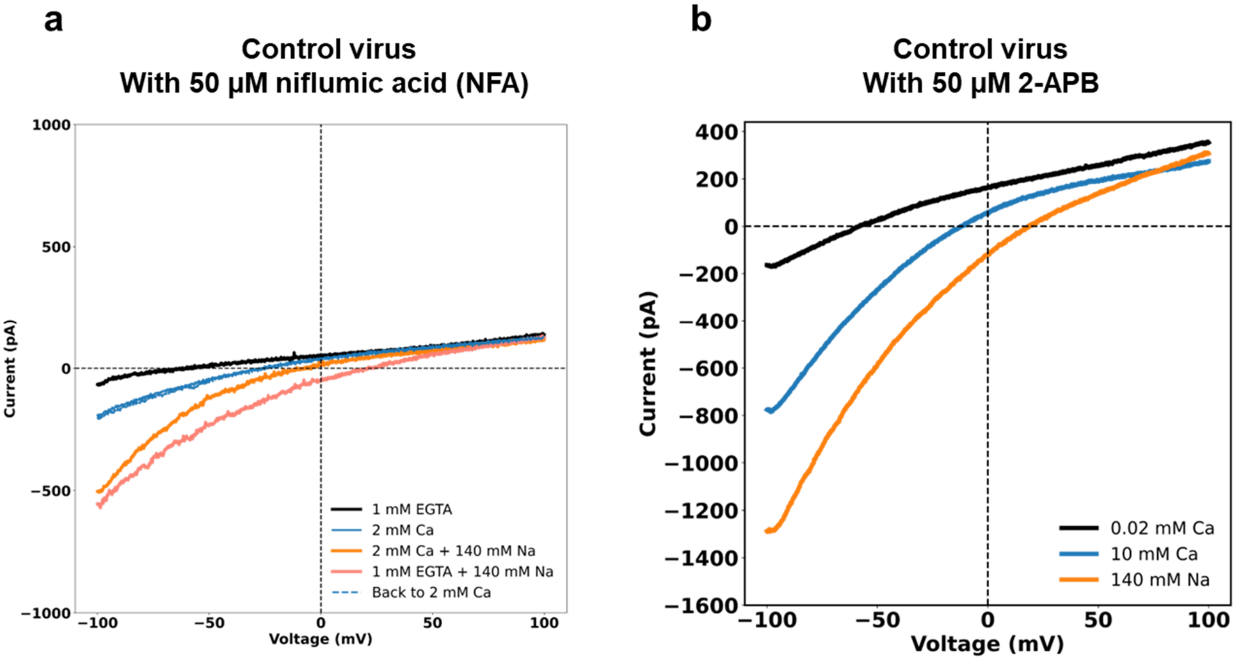

Fig. 26: I-V relations obtained from the –100 mV to +100 mV voltage ramp protocol on cells infected with control virus. a, Recordings obtained with 50 μM NFA included in the patch pipette. **b**, Recordings obtained with 50 μM 2-APB in the patch pipette.

Then do we have any clues on how to reduce the background? We have found previously that this endogenous current was an Mg^{2+}-sensitive non-selective cation current. Coincidently it has been reported in a few literature papers that a specific type of current, later referred to as a TRPM7-like current, was inhibited by inclusion of Mg^{2+} in the intracellular solution (effective with both MgATP and free Mg^{2+})[66–68]. Mg^{2+} was also found to block some Ca^{2+} channels[5,69], so the concentration of Mg^{2+} used in the intracellular solution was examined carefully, aiming at reducing the endogenous current and meanwhile still being able to record the designed channels. Using the MAX chelator program[70] to calculate the free [Mg^{2+}] in the solution, we tested different intracellular solutions containing EGTA/Mg or EGTA/MgATP, and it seemed like the appropriate free Mg^{2+} concentration ranged between 0.3 to 1 mM for our purpose. Therefore, we decided to include 4 mM MgATP (together with 20 mM EGTA that was for chelating Ca^{2+}) in our patch pipette, resulting in a final free [Mg^{2+}] of around 400 µM (**Fig. 27**). ATP is a better Mg buffer than EGTA, thereby facilitating a more precise control over the free Mg^{2+} concentration. Under this condition, both the current recorded on the cells infected with virus encoding the design and the virus decreased in 10 mM [Ca^{2+}] compared to that without 4 mM MgATP intracellularly. This was expected because the endogenous channel in the cells expressing the designs was inhibited to a similar extent as that in the cells infected with control virus. Although there was still observable Ca^{2+} permeability in the negative control cells, which might be due to other promiscuous Ca^{2+}-permeable channels, the increase of current, specifically in the negative voltage ranges, after the bath solution was changed from 0.02 mM [Ca^{2+}] to 10 mM [Ca^{2+}] of the design CalC6_3 was obviously larger than the negative control. Although there was not a dramatic difference in the fold of current increase between the design and the control, it was sufficiently notable for us to distinguish between the two instances.

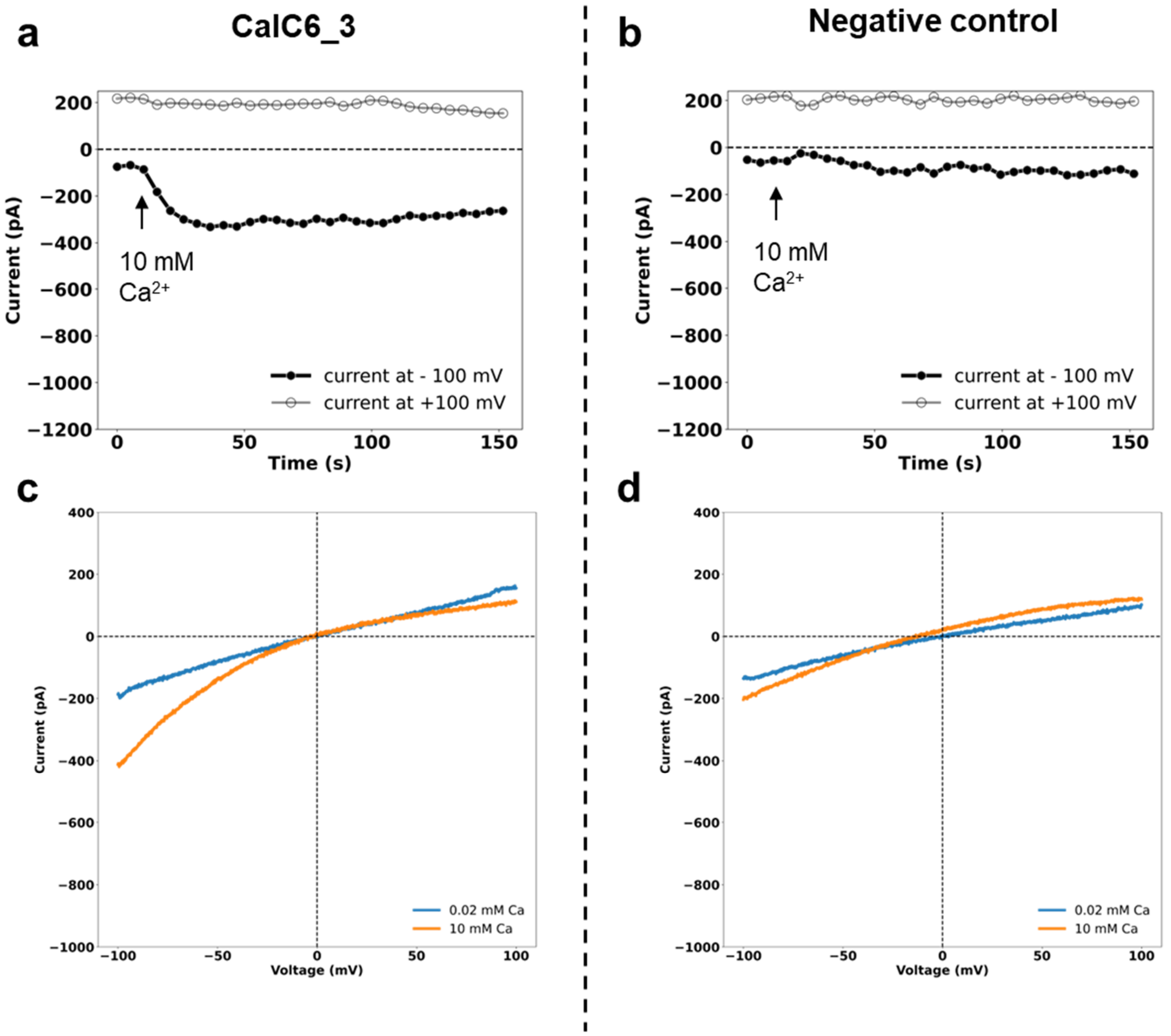

Fig. 27: Patch-clamp recordings with 4 mM MgATP included in the patch pipette. a and **b**, Time courses of currents measured at –100 mV and +100 mV on cells infected with CalC6_3 virus **(a)** and the control virus **(b)**, respectively. **c** and **d**, I-V relations obtained in bath solutions containing 0.02 mM [Ca^{2+}] and 10 mM [Ca^{2+}] on the cells infected with CalC6_3 virus **(c)** and the control virus **(d)**, respectively.

With the experimental protocols being improved in all aspects, we proceeded with characterizing the two most promising designs, CalC4_24 and CalC6_3. These two designs have distinct protein geometries and therefore different selectivity filter geometries (CalC4_24 is with four-fold symmetry whereas CalC6_3 is with six-fold symmetry), and have been characterized to assemble into homogeneous pore-forming particles on the ns-EM grids. Inward current at –100 mV was observed to increase for both CalC4_24 and CalC6_3 in 10 mM [Ca^{2+}] bath solution. This increase of inward currents was reversible and was diminished when the bath solution was changed back to 0.02 mM [Ca^{2+}] solution (**Fig. 28**).

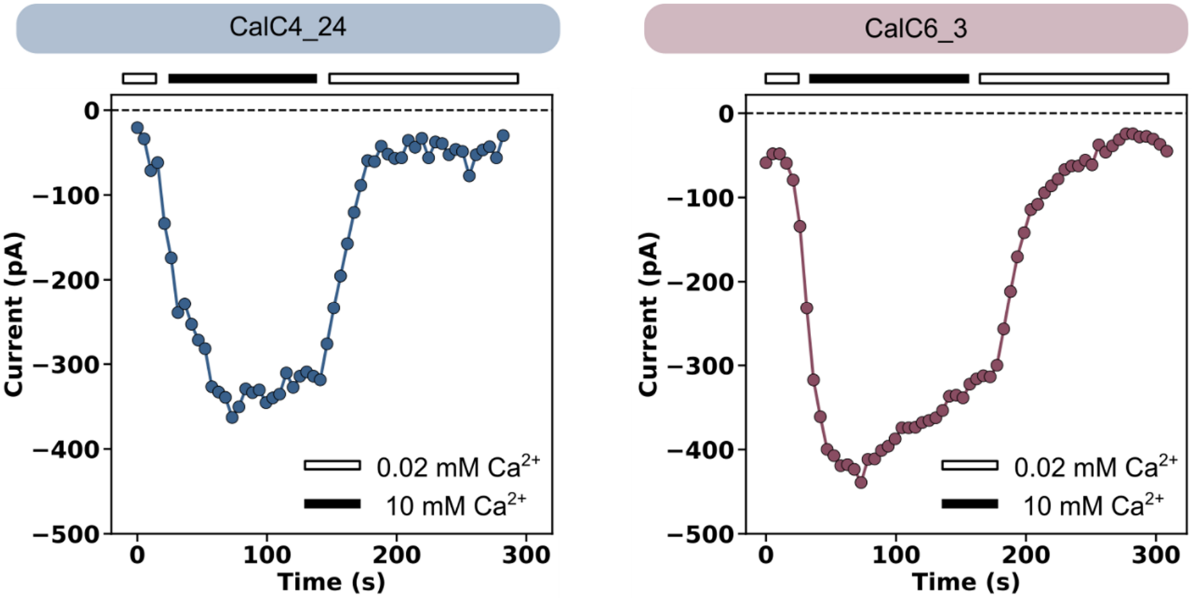

Fig. 28: Time courses of the inward whole-cell currents of CalC4_24 and CalC6_3 recorded at –100 mV in Hi5 cells. Cells were first bathed in 0.02 mM [Ca^{2+}] NMDG-based solution (the first unfilled bars). The extracellular solution was then changed to 10 mM [Ca^{2+}] solution (the black bars), and was finally changed back to 0.02 mM [Ca^{2+}] solution (the third unfilled bars).

Using both a voltage step protocol (with a holding potential of 0 mV) and a voltage ramp protocol to obtain the I-V relations of both channels from –100 mV to +100 mV, sharp inward rectifications were observed for both designs (**Fig. 29 and 30**), as expected based on our experimental design. This was because Ca^{2+} was only present extracellularly and hence could only give rise to inward currents. To systematically compare the relative magnitudes of the currents conducted by the designed channels in relation to the endogenous currents, the currents were normalized by cell capacitance to obtain current densities and then averaged over four cells. The endogenous current density was approximately 4 pA pF^{-1} at –100 mV in the 10 mM [Ca^{2+}] solution, while the current densities in cells expressing CalC4_24 and CalC6_3 were determined to be 7.5 pA pF^{-1} and 9.1 pA pF^{-1}, respectively, both evidently larger than the background current (**Fig. 30**).

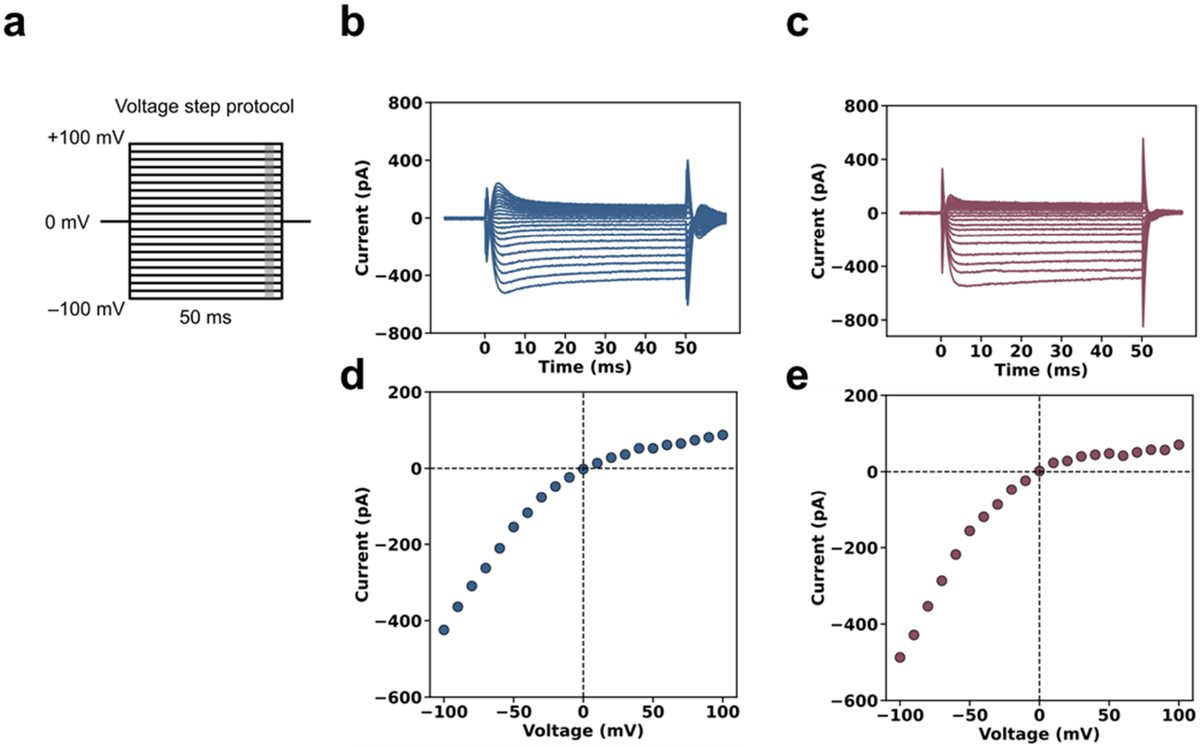

Fig. 29: Recording of currents of the designed channels using a voltage step protocol. a, The schematic illustration of the voltage step protocol. **b** and **c**, Ca^{2+} currents elicited by the voltage step protocol recorded on Hi5 cells expressing CalC4_24 (**b**) and CalC6_3 (**c**), respectively. **d** and **e**, the **I**-V relations obtained from **b** and **c**, respectively. Tail currents (shown as the gray region in **a**) were used to plot the **I**-V curves.

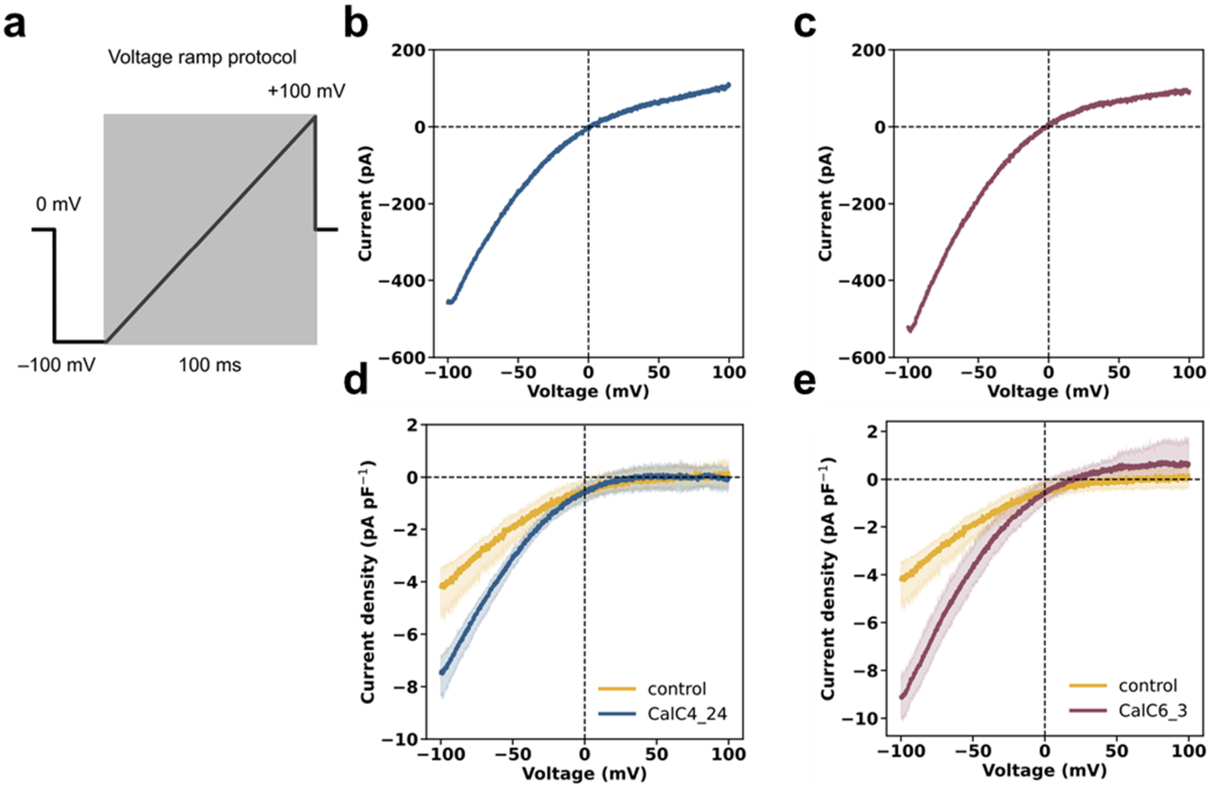

Fig. 30: Recording of currents of the designed channels using a voltage ramp protocol. a, The schematic illustration of the voltage ramp protocol. The gray region shows the range used for plotting the I-V curves. **b** and **c**, Ca^{2+} currents elicited by the voltage ramp protocol recorded on Hi5 cells expressing CalC4_24 (**b**) and CalC6_3 (**c**), respectively. **d** and **e**, Current densities from cells expressing CalC4_24 (**d**) and CalC6_3 (**e**) in 10 mM [Ca^{2+}] solution after background subtraction using currents recorded in 0.02 mM [Ca^{2+}] solution. The control curves (yellow) were obtained from cells infected with the baculovirus that did not encode recombinant proteins (made from an empty pFastBac-Dual plasmid), and were included in both **d** and **e** for comparison. Each I-V curve was obtained by averaging over four measurements on separate cells.

To examine the specificity of the channels for different cations under this experimental condition, the 10 mM Ca^{2+} in the extracellular solution was substituted with 40 mM Na^{+} ,10 mM Sr^{2+} or 10 mM Mg^{2+} (the Na^{+} concentration was four times that of the divalent ions as the current scales with the square of the ion valence). As discussed previously, in our case the relative permeabilities of ions through ion channels were difficult to derive from the reversal potential using the GHK voltage equation because this was complicated by the concentration gradient-driven diffusion through the open channels, and the contribution of endogenous currents to the reversal potential is difficult to disentangle. We instead compared conductances for each cation based on the inward current at –100 mV. Both CalC4_24 and CalC6_3 showed ~5 fold larger current in 10 mM [Ca^{2+}] than in 40 mM [Na^{+}] solution at –100 mV (**Fig. 31**). The Na^{+} current recorded on cells infected with the control virus was close to baseline (**Fig. 32**). The relative conductances of the divalent cations for both designs followed the order Ca^{2+} > Sr^{2+} > Mg^{2+}, displaying similar properties as several native Ca^{2+} channels (Ca_v, TRPV6, CRAC)[33,69,71–75]. Likewise, both channels were blocked by 10 µM La^{3+}, which blocks native Ca^{2+} channels.

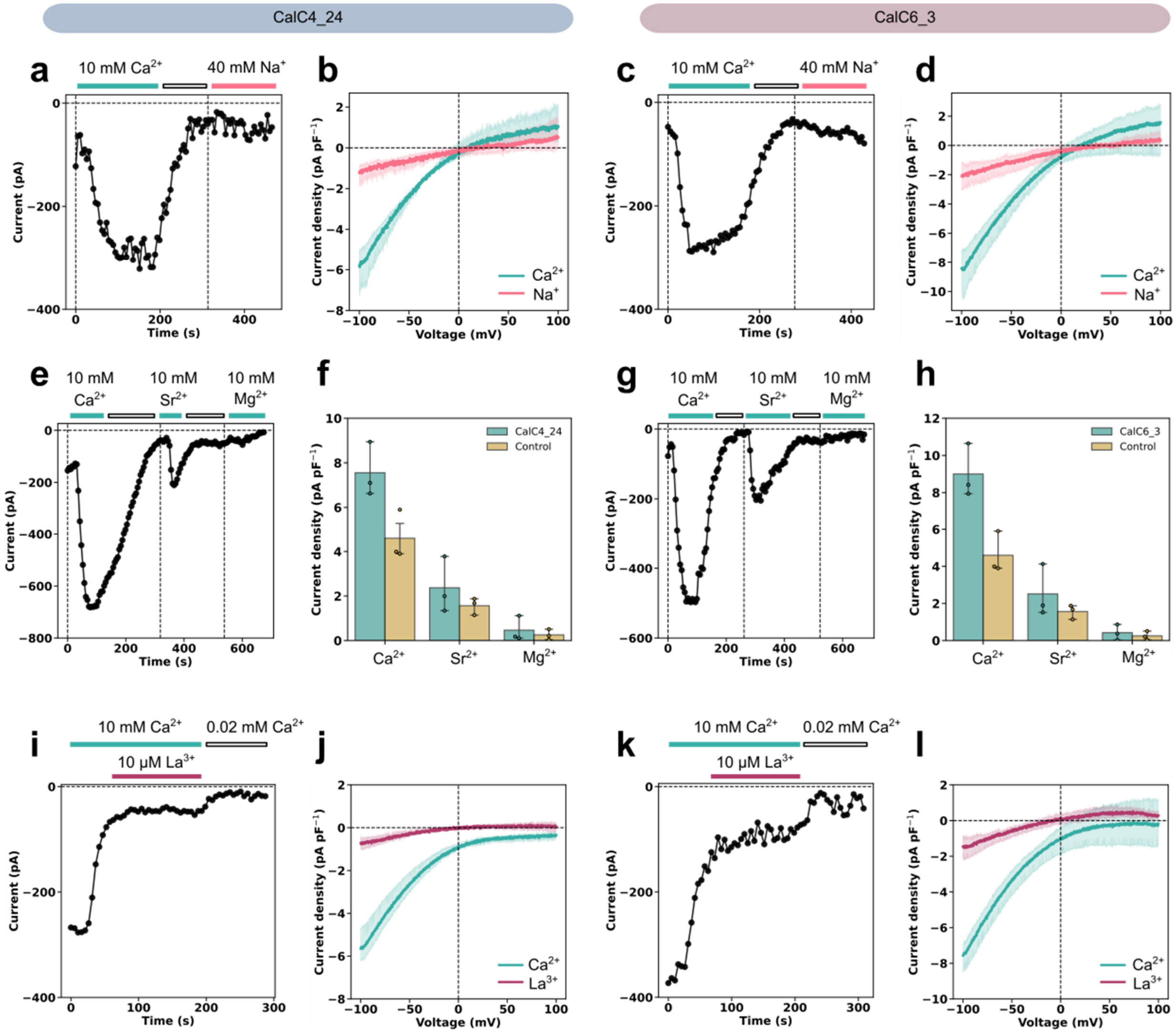

Fig. 31: Ion selectivity of designed Ca^{2+} channels. a-d, Relative conductances of CalC4_24 **(a-b)** and CalC6_3 **(c-d)** for Ca^{2+} and Na^{+}. **a** and **c**, Time courses of currents at –100 mV. Extracellular solution was exchanged from a solution containing 10 mM [Ca^{2+}] to 40 mM [Na^{+}] with 0.02 mM [Ca^{2+}] solution between the exchange. **b** and **d**, I-V relations obtained from a –100 mV to +100 mV ramp protocol (Ca^{2+} currents in cyan and Na^{+} currents in red). **e-h,** Relative conductances of CalC4_24 **(e-f)** and CalC6_3 **(g-h)** for Ca^{2+}, Sr^{2+} and Mg^{2+}. **e** and **g**, Time courses of currents at –100 mV. Extracellular solution was exchanged from a solution containing 10 mM [Ca^{2+}] to 10 mM [Sr^{2+}] and 10 mM [Mg^{2+}], with 0.02 mM [Ca^{2+}] solution between each exchange. **f** and **h**, Averaged peak current densities at –100 mV in each 10 mM divalent ion solution (n=3). The data obtained from cells infected by the control virus were presented in yellow (n=3) and were included in

both plots for comparison. **i-l,** Blockade of Ca^{2+} current of CalC4_24 **(i-j)** and CalC6_3 **(k-l)** by 10 μM La^{3+}. **i** and **k**, Time courses of currents at –100 mV recorded in 10 mM [Ca^{2+}] solution, followed by addition of 10 μM La^{3+}, and finally in 0.02 mM [Ca^{2+}] solution. **j** and **l**, I-V relations obtained from a –100 mV to +100 mV ramp protocol before (cyan) and after (purple) addition of 10 μM La^{3+} to the 10 mM [Ca^{2+}] solution. Each I-V curve was averaged over three measurements on separate cells, with the baseline current measured in 0.02 mM [Ca^{2+}] subtracted.

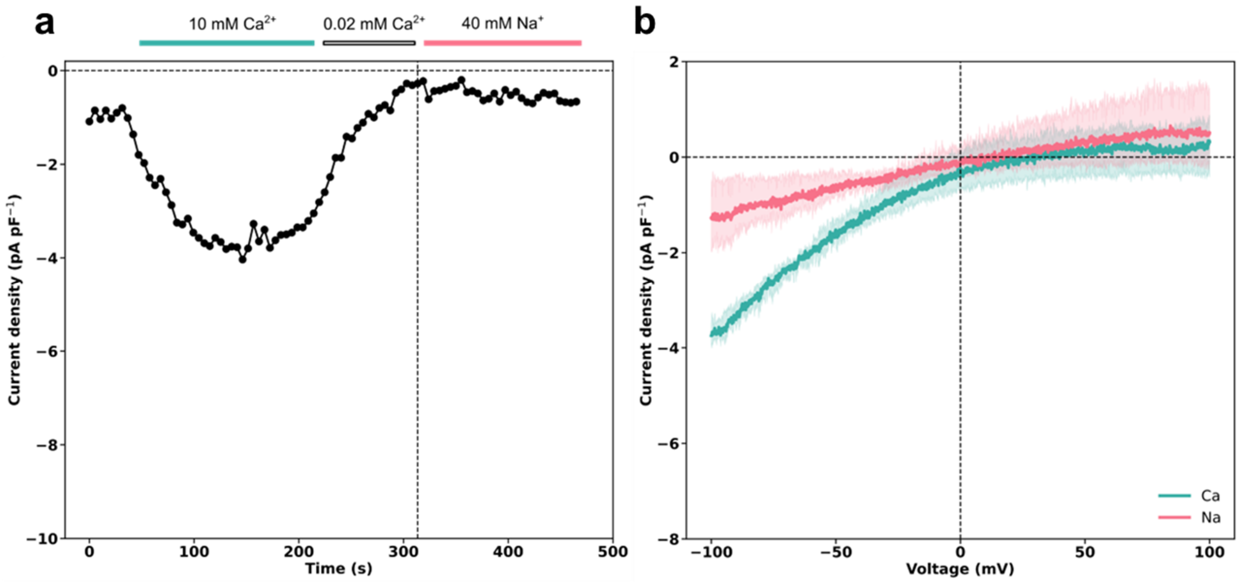

Fig. 32: Characterization of Ca^{2+} permeability versus Na^{+} permeabilities on cells infected with the control virus. a, Time courses of currents at –100 mV. **b,** I-V relations obtained from a –100 mV to +100 mV ramp protocol averaged over three measurements on separate cells.

Both CalC4_24 and CalC6_3 exhibit electrophysiological properties expected for Ca^{2+} channels: inward rectification in presence of extracellular Ca^{2+}, higher relative conductances to Ca^{2+} than to other cations, and block by lanthanum. Thus, our approach of arranging Glu/Asp carboxylate residues around a central pore generates Ca^{2+} dependent channels as intended. Although the selectivity filter of CalC6_3 (6.4 Å) is much wider than that in CalC4_24 (2.5 Å), the electric field strength near the filter is probably stronger in CalC6_3 due to the presence of two extra Glu residues, likely facilitates recruitment of Ca^{2+} ions. The adjacent Glu residues could interact and partially dehydrate the Ca^{2+} ion in an asymmetric manner as predicted by AlphaFold3, as in the selectivity filter configuration observed in the crystal structure of the $Ca_{V}ab$ channel in complex with dihydropyridine compounds[76]. In our experiments 4 mM MgATP (free [Mg^{2+}] estimated to be approximately 400 µM in the presence of 20 mM EGTA by MAX Chelator program) was included in the patch pipette, and this could also reduce the currents observed for Na^{+} and other divalent ions, as AF3 also predicts some binding of Mg^{2+} to the selectivity filter (shown previously in **Fig. 16**), consistent with observations that Mg^{2+} can bind to selectivity filters but not readily permeate in some native Ca^{2+} channels[5,69,77]. The relative conductances order $Ca^{2+} > Sr^{2+} > Na^{+}$ of the designs probably reflected a preferential binding of ions at the selectivity filter with a high field strength.

3.5. Cryo-EM structure determination

To assess the design accuracy, we sought to determine the structure of CalC6_3 using cryo-electron microscopy (cryo-EM). CalC6_3 in detergent particles appeared homogeneous after being frozen on the grid and 4,644 movies were collected (**Fig. 33**); however, top views of the particles could not readily be separated from side views during 2D classification due to the spherical shape of the detergent-bound membrane protein, a well-known challenge for structural determination of relatively small membrane proteins without obvious soluble domains[78].

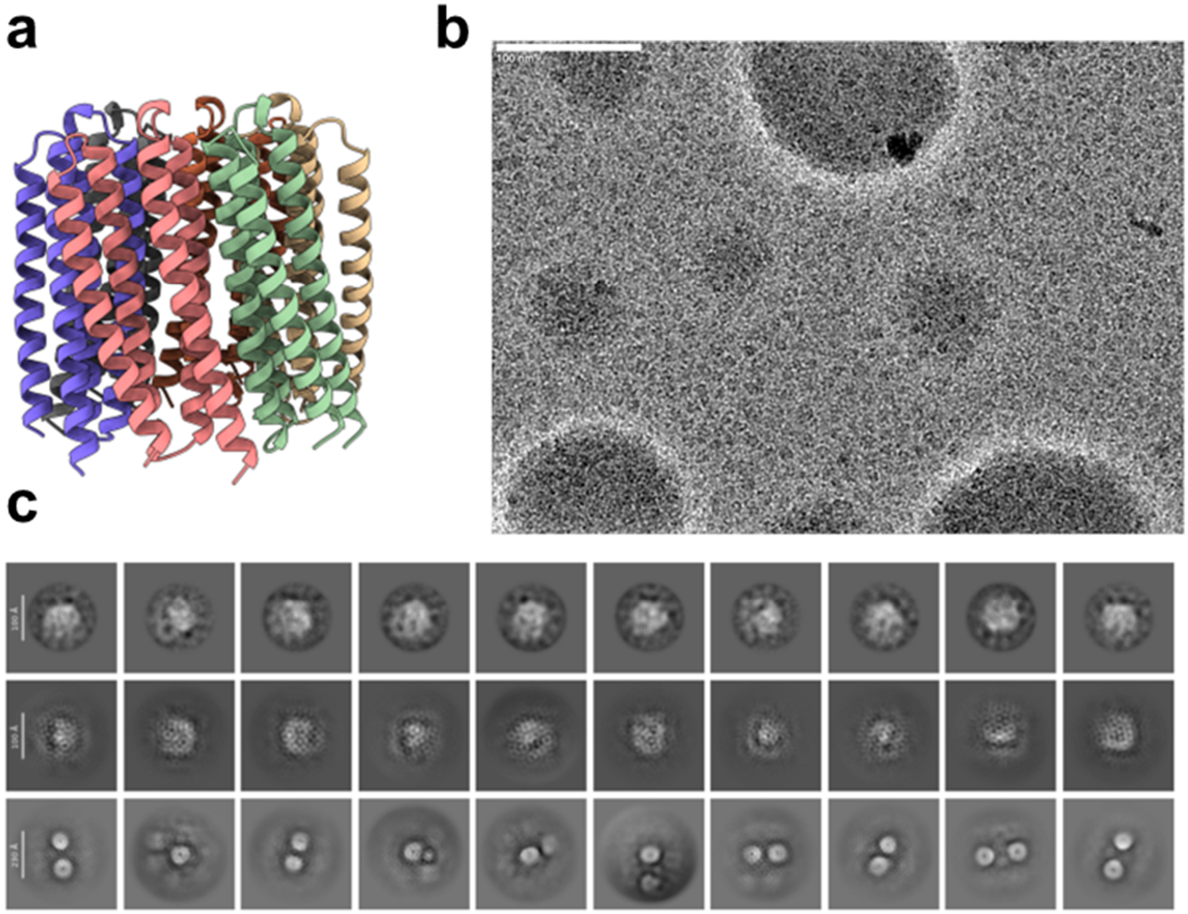

Fig. 33: Cryo-EM characterizations on the design CalC6_3. a, The design model of CalC6_3. **b,** A representative cryo-EM micrograph of protein particles on a lacey carbon grid. Scale bar, 100 nm. **c,** 2D class averages from three different 2D classification settings, with an extraction box size of 300 pixels used in the top two rows and an extraction box size of 680 pixels (pixel size 0.4135 Å) used in the bottom row.

To facilitate structural determination, we applied a fusion protein strategy: we connected structurally-validated designed helical repeat (DHR) proteins[79] to the C-terminus of CalC6_3 via straight helices, with linker helices generated using RFdiffusion and sequences designed using ProteinMPNN. Six designs were ordered and purified as was done for the original CalC6_3 construct, except that a Superose 6 increase 10/300 column was used for SEC. Among the six tested channel-DHR fusion proteins, one showed quite homogeneous particles on the ns-EM grid (**Fig. 34 and 35**; note that although the SEC elution profiles looked quite similar for all six tested designs, only one was found to form homogenous pore-containing on the ns-EM grid). Interestingly, the extended DHR arms, in both the top view and the side view, were visible after 2D classification directly from an image dataset collected on the ns-EM grid.

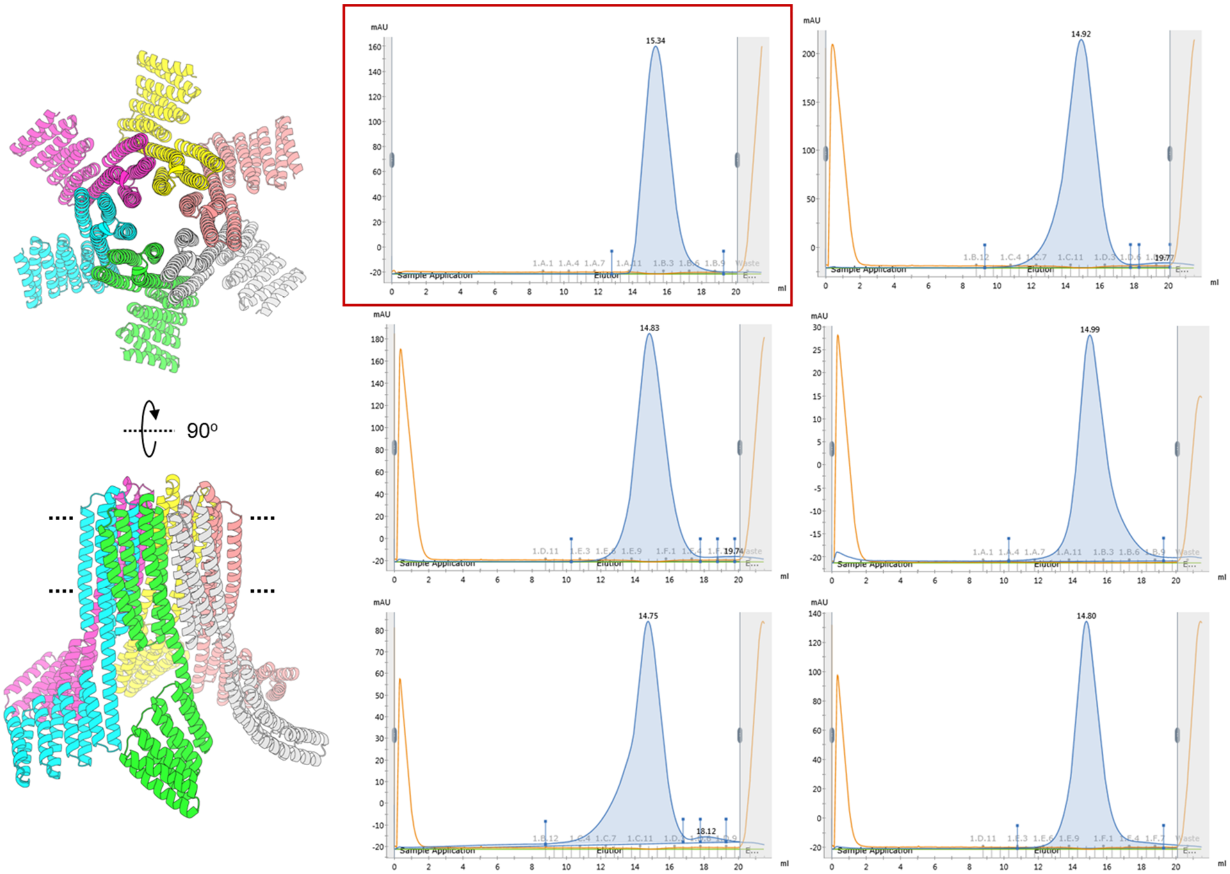

Fig. 34: A representative design model of CalC6_3 after fusion with DHR proteins and SEC elution profiles of all tested CalC6_3-DHR constructs. The red square highlights the SEC profile of the construct that was chosen for further electron microscopy analysis.

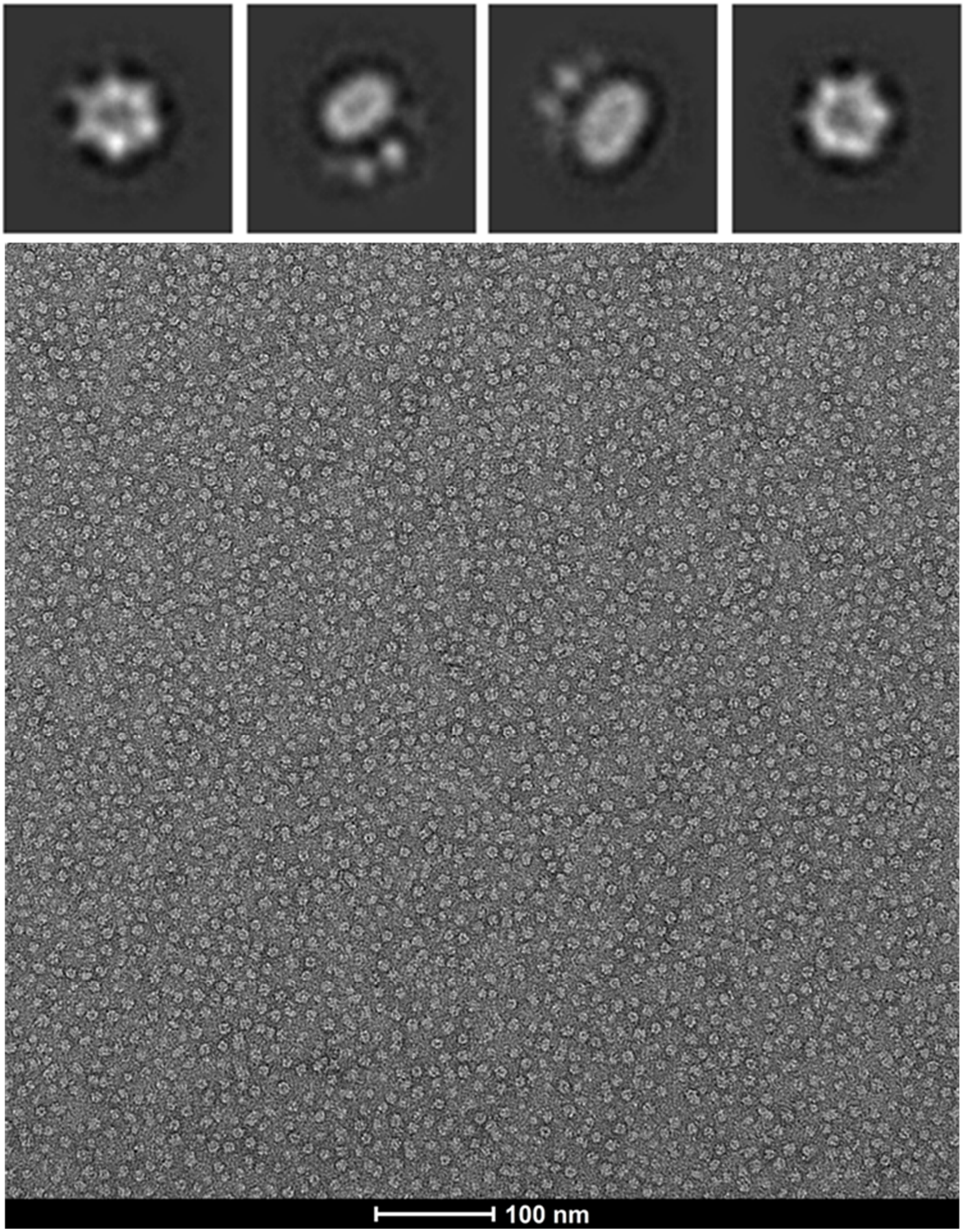

Fig. 35: The ns-EM micrograph and four representative 2D classes of the CalC6_3 design fused with DHR.

We proceeded with cryo-EM data collection with this construct. Two types of grids were tried (thin carbon grid and holey carbon grid). Protein particles on both grids were homogenous. The thin carbon grid seemed to result in a clearer top view during 2D classification, while the holey carbon grid seemed to favor more particles in the side view (**Fig. 36**).

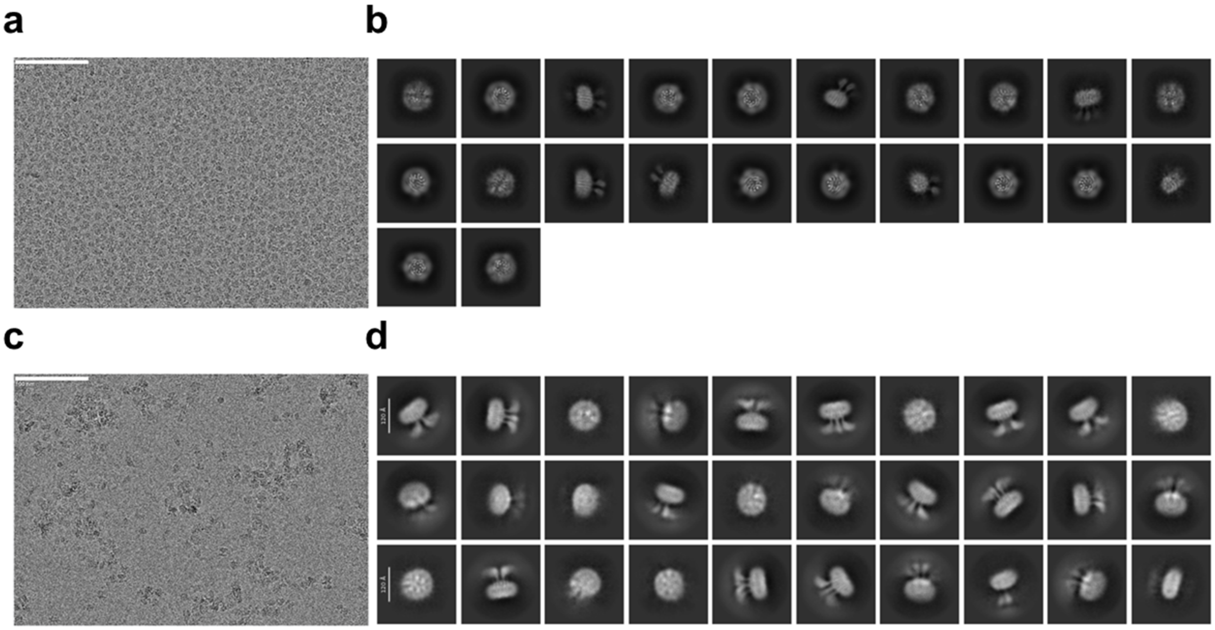

Fig. 36: Cryo-EM analysis of the CalC6_3-DHR protein. a and **c**, Representative cryo-EM micrographs of CalC6_3-DHR protein particles on a thin carbon grid **(a)** and a holey carbon grid **(c)**, respectively. **b** and **d**, 2D class averages from the thin carbon grid **(b)** and from the holey carbon grid **(d)**, respectively. Scale bars in the micrographs, 100 nm. Scale bars in d, 12 nm.

We proceeded with the dataset collected on the thin carbon grid and obtained a three-dimensional reconstruction to a global resolution of 3.75 Å with C6 symmetry and were able to build a structure model based on the density map (**Fig. 37**). The density for the DHR extension domains were not well resolved possibly due to structural flexibility. In this cryo-EM structure, the density for the Glu-ring selectivity filter density and the His-ring below the filter was clearly evident when contoured at and below 4 σ level, suggesting pre-organization of Glu-ring by the His-ring via potential hydrogen bond interactions. Other than a slight swelling of the cryo-EM complex structure compared to the design model (backbone RMSDs of 1.04 Å and 1.26 Å for monomer and complex alignment, respectively), the geometry of the selectivity filter was almost exactly as designed.

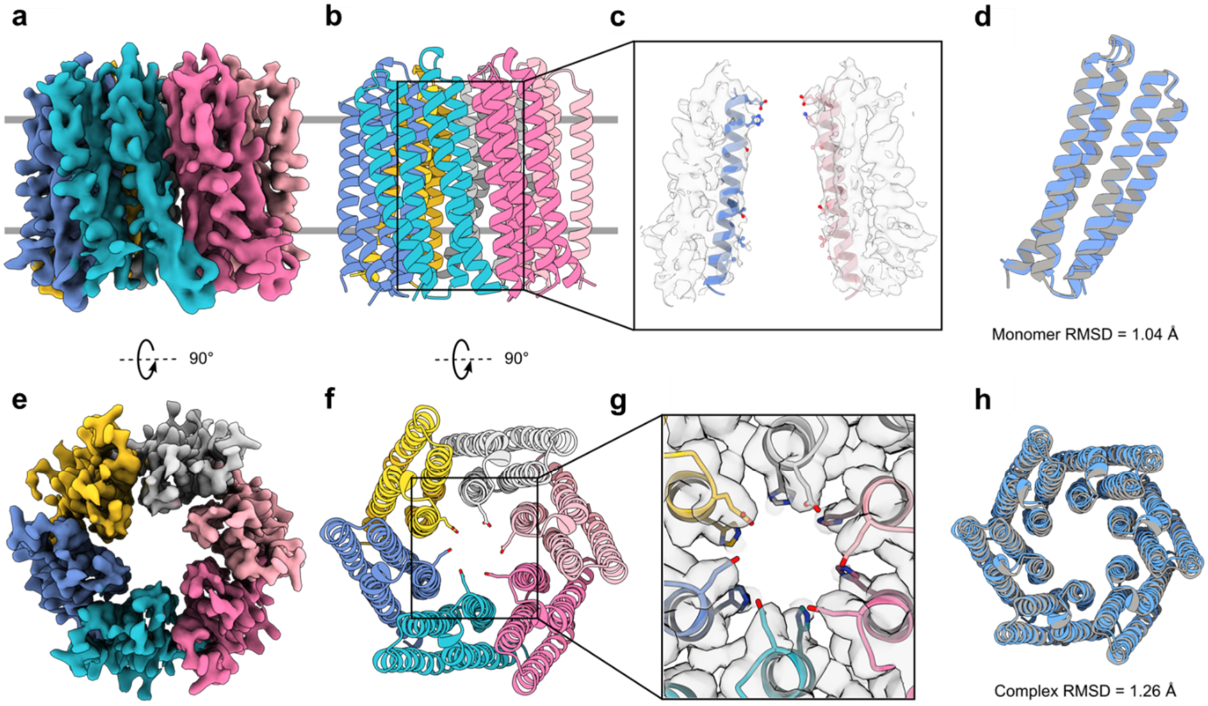

Fig. 37: Cryo-EM structure of CalC6_3. a and e, Side **(a)** and top **(e)** views of sharpened cryo-EM density map of CalC6_3. **b and f**, Structural model of CalC6_3, with the same colors and orientations as the density map in **(a)** and **(e)**, respectively. **c and g,** Close-up views of the pore-lining helices **(c)** and the selectivity filter **(g)**, with the densities shown as gray surfaces contoured at 4 σ. For the side view of pore helices in **(c)** only the opposing monomers were shown for clarity. **d and h,** Structural alignment of the monomer **(d)** and the hexamer **(h)** of the CalC6_3 design model (gray) to the cryo-EM structure (blue), with backbone RMSDs of 1.04 Å and 1.26 Å for the monomer and complex alignment, respectively.

We were also able to identify some minor heptamer and octamer species from the 2D classification, and were able to further perform 3D reconstructions for the heptamer to a overall resolution of 4.62 Å with C7 symmetry (**Fig. 38**). The existence of additional oligomeric states is not unexpected. This phenomenon has also been observed in naturally-existing proteins, most notably the calcium homeostasis modulator (CALHM) family members[80,81].

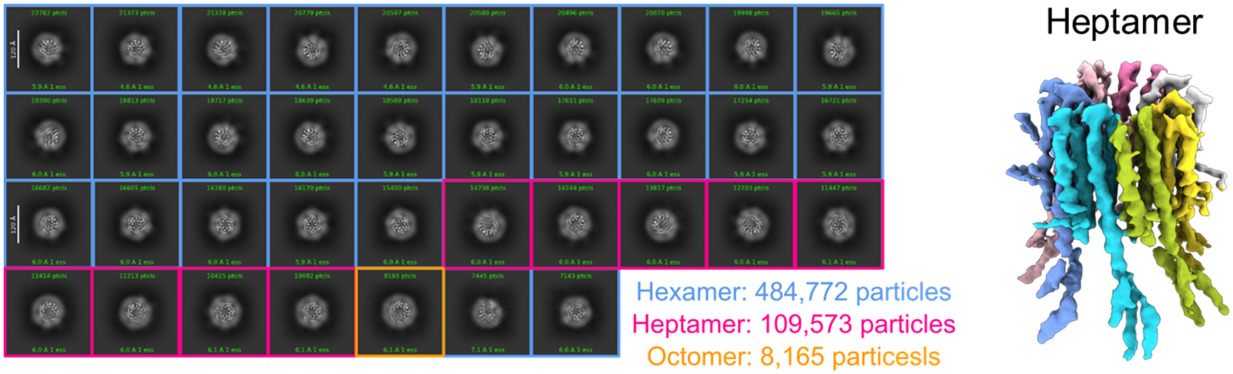

Fig. 38: Off-target oligomeric states observed for CalC6_3-DHR. 2D classes obtained from the cryo-EM thin carbon grid showed roughly 81% particles assembled as hexamer, 18% assembled as heptamer, and 1% assembled as octamer. A 3D reconstruction was obtained for the heptamer to a final global resolution of 4.62 Å with C7 symmetry.

4. Discussions and future directions

De novo design of ion channels is in principle a powerful approach to study ion channel biophysics and to develop new biological tools, but the ability to tune ion selectivity has been limited by lack of an approach to install selectivity filters with specified composition and geometry into designed channels. We demonstrate that using RFdiffusion symmetric motif scaffolding, protein topologies can be built from scratch to optimally scaffold selectivity filters with pre-defined geometries. In contrast, previously design efforts sought to change conductances by altering the number of alpha helices or beta strands surrounding the pore, and as a result a Ca^{2+} channel was not designable given the challenge of selectively recognize Ca^{2+} ions while maintaining a rapid Ca^{2+} ion flow, which requires precise placement of selectivity filter residues with atomic level precision. The designed CalC4_24 and CalC6_3 channels have different designed selectivity filter geometries, and both exhibited higher conductances to Ca^{2+} than to other cations. The high degree of agreement between the cryo-EM structure and the design model of CalC6_3 demonstrates the accuracy of our design method.

Our approach enables the exploration of diverse selectivity filter geometries and chemical compositions for optimal ion channel conductance and selectivity, which are difficult to probe through classical native ion channel mutagenesis experiments: for example, it will be very interesting to explore how increasing selectivity filter complexity, and incorporating additional filter layers, impacts channel selectivity. Building up channels around defined selectivity filter geometries should both enable rigorous testing of our understanding of the determinants of native ion channel selectivity, and the construction of a wide array of new channels with selectivities that go beyond those observed in nature. For example, our design approach developed in this study can be foreseeably extended to designing channels to selectively permeate an ion that naturally existing ion channels are not conducting, such as iron, copper and zinc. These channels can be used for investigating the molecular determinants of selectivity for those transition metal ions and the biological effects of the influx of those ions.

We anticipate that incorporation of molecular switches into our designed channels that would convert the constitutively open channels into gated ion channels would be the next significant advancement in this field of ion channel design. This would provide many advantages. First, it would allow quantification of relative ion permeability experimentally based on reversal potentials as has been traditionally done for native ligand-gated ion channels. Second, it would facilitate the expression of channels in cells at a high level, which was not feasible for constitutively open channels because they were causing the cells to be unhealthy, and thereby would enable more evident experimental outcomes (and potentially a higher screening throughput because higher signal-to-noise ratios would allow a coarse-grained yet rapid screening method as opposed to making lentivirus for each individual construct). The above two aspects together would in turn facilitate experimental characterizations of a much more diverse sampling space of selectivity filter geometries and chemical properties, which has not been achieved so far due to the great challenge of characterizing leaky channels. Furthermore, the ability to customize the response of designed ion channels to a given ligand would provide robust sensing modalities. It would also enable direct modulation of ion flux in particular cell types conditionally, thereby providing a biorthogonal toolbox that would be useful for numerous biological studies including apoptosis, cell communication, and neuronal firing and inhibition.

5. Acknowledgements

First and foremost, I would like to express my deepest gratitude to my advisors, Prof. David Baker and Prof. Bill Catterall. Their support and guidance have been invaluable throughout my PhD journey, without which I would not have been able to complete my study. Their mentorship has shaped my research, sculpted my scientific preferences, and fueled my passion for the fields of *de novo* protein design and ion channel research. I am incredibly fortunate to have the opportunity to learn and am still actively learning to conduct interesting science, to solve important scientific problems (which David is always emphasizing), and to be a good mentor.

I wish to dedicate this work to the memory of Prof. Bill Catterall, whose sudden passing in February 2024 was a shock to me and a profound loss to the entire field of ion channel research. I am forever grateful for the guidance and inspiration he provided me. I still remember the story he told in a small group meeting about his early career on how he and his colleague were attempting to isolate batrachotoxin from tree frogs and study its role on voltage-gated sodium channels, while he was finally able to visualize this interaction in the cryo-EM structure almost 40 years after those early attempts. I will carry his legacy and spirit with me throughout my career.

I would also like to extend my thanks to Prof. Frank DiMaio, Prof. Tamer M. Gamal El-Din and Prof. Jens Gundlach for kindly serving as my committee members. Their support and feedback on my projects have also been extremely helpful in clarifying my research objectives and identifying potential problems. I thank them for taking the time to attend my coming thesis defense and my General Exam last year.

Many lab members in the Baker lab and the Catterall lab, as well as scientists at other institutions, have provided helpful suggestions, support and joy throughout my PhD. Among them are:

- Tim Huddy, Chunfu Xu and Samuel Berhanu – for early mentorship.

- Connor Weidle, Ljubica Mihaljević, Ryan Kibler, Joseph Watson, Zhe Li, Tracy Yu, Sagardip Majumder, Andrew Borst, Kenneth Carr – for direct contributions to this research.
- Gyu Rie Lee, Nikita Hanikel, David Juergens, David Lee, David Feldman, Justas Dauparas, Kejia Wu, Wei Yang, Xinru Wang, Andy Yeh, Thomas Schlichthaerle, Adam Broerman, Dane Zambrano, Dan Humphrys, Xiangli Qu, George Wisedchaisri, Mike Lenaeus, Lige Tonggu, Lipeng Wang, Ruth Westenbroek, Tim Lantin – for helpful discussions and inspirations.
- David Clapham, Raymond Hulse and Stephan Pless – for advice on improving experimental conditions and comments on manuscript writing.
- Kandise VanWormer, Luki Goldschmidt, Lynda Stuart, Zari Magness, Justin Decarreau, Maggie Ahlrichs, Suna Cheng, Craig Dobbins, Jin Li, Edelmar Navaluna – for general technical, administrative, and computational support.

Special thanks to my friend Jinhang Chen (and his wife Le Yu as well as their cat Momo) for emotional support and companionship over the years, which keeps encouraging me to pursue higher goals. Without their encouragement I fear that I would have quit along the way.

Finally, to my parents, your love, support and understanding have always been a strong source of strength and motivation for me. Thank you for supporting me in my pursuit of higher education and scientific goals. I look forward to being reunited with you soon.

6. References

1. Magnus, C. J. *et al.* Ultrapotent chemogenetics for research and potential clinical applications. *Science* **364**, eaav5282 (2019).

2. Jing, M. *et al.* A genetically encoded fluorescent acetylcholine indicator for in vitro and in vivo studies. *Nat. Biotechnol.* **36**, 726–737 (2018).

3. Yue, L., Navarro, B., Ren, D., Ramos, A. & Clapham, D. E. The Cation Selectivity Filter of the Bacterial Sodium Channel, NaChBac. *J. Gen. Physiol.* **120**, 845–853 (2002).

4. Tang, L. *et al.* Structural basis for Ca^{2+} selectivity of a voltage-gated calcium channel. *Nature* **505**, 56–61 (2014).

5. Nilius, B. *et al.* The Single Pore Residue Asp542 Determines Ca^{2+} Permeation and Mg^{2+} Block of the Epithelial Ca^{2+} Channel*. *J. Biol. Chem.* **276**, 1020–1025 (2001).

6. Ellinor, P. T., Yang, J., Sather, W. A., Zhang, J.-F. & Tsien, R. W. Ca^{2+} channel selectivity at a single locus for high-affinity Ca^{2+} interactions. *Neuron* **15**, 1121–1132 (1995).

7. Yang, J., Elllnor, P. T., Sather, W. A., Zhang, J.-F. & Tsien, R. W. Molecular determinants of Ca^{2+} selectivity and ion permeation in L-type Ca^{2+} channels. *Nature* **366**, 158–161 (1993).

8. Meyer, J. O. *et al.* Disruption of the Key Ca^{2+} Binding Site in the Selectivity Filter of Neuronal Voltage-Gated Calcium Channels Inhibits Channel Trafficking. *Cell Rep.* **29**, 22-33.e5 (2019).

9. Long, S. B., Tao, X., Campbell, E. B. & MacKinnon, R. Atomic structure of a voltage-dependent K+ channel in a lipid membrane-like environment. *Nature* **450**, 376–382 (2007).

10. Derebe, M. G., Zeng, W., Li, Y., Alam, A. & Jiang, Y. Structural studies of ion permeation and Ca^{2+} blockage of a bacterial channel mimicking the cyclic nucleotide-gated channel pore. *Proc. Natl. Acad. Sci.* **108**, 592–597 (2011).

11. Shen, P. S. *et al.* The Structure of the Polycystic Kidney Disease Channel PKD2 in Lipid Nanodiscs. *Cell* **167**, 763-773.e11 (2016).

12. Yu, F. H. & Catterall, W. A. The VGL-Chanome: A Protein Superfamily Specialized for Electrical Signaling and Ionic Homeostasis. *Sci. STKE* **2004**, re15 (2004).

13. Tikhonov, D. B. & Zhorov, B. S. P-Loop Channels: Experimental Structures, and Physics-Based and Neural Networks-Based Models. *Membranes* **12**, 229 (2022).

14. Connolly, C. N. & Wafford, K. A. The Cys-loop superfamily of ligand-gated ion channels: the impact of receptor structure on function. *Biochem. Soc. Trans.* **32**, 529–534 (2004).

15. Huang, P.-S., Boyken, S. E. & Baker, D. The coming of age of de novo protein design. *Nature* **537**, 320–327 (2016).

16. Baker, D. What has de novo protein design taught us about protein folding and biophysics? *Protein Sci.* **28**, 678–683 (2019).

17. Joh, N. H. *et al.* De novo design of a transmembrane Zn^{2+}-transporting four-helix bundle. *Science* **346**, 1520–1524 (2014).

18. Mravic, M. *et al.* Packing of apolar side chains enables accurate design of highly stable membrane proteins. *Science* **363**, 1418–1423 (2019).

19. Mahendran, K. R. *et al.* A monodisperse transmembrane α-helical peptide barrel. *Nat. Chem.* **9**, 411–419 (2017).

20. Krishnan R, S. *et al.* Assembly of transmembrane pores from mirror-image peptides. *Nat. Commun.* **13**, 5377 (2022).

21. Lear, J. D., Wasserman, Z. R. & DeGrado, W. F. Synthetic Amphiphilic Peptide Models for Protein Ion Channels. *Science* (1988) doi:10.1126/science.2453923.

22. Xu, C. *et al.* Computational design of transmembrane pores. *Nature* **585**, 129–134 (2020).

23. Scott, A. J. *et al.* Constructing ion channels from water-soluble α-helical barrels. *Nat. Chem.* **13**, 643–650 (2021).

24. Berhanu, S. *et al.* Sculpting conducting nanopore size and shape through de novo protein design. *Science* **385**, 282–288 (2024).

25. Vorobieva, A. A. *et al.* De novo design of transmembrane β barrels. *Science* **371**, eabc8182 (2021).

26. Gouaux, E. & MacKinnon, R. Principles of Selective Ion Transport in Channels and Pumps. *Science* **310**, 1461–1465 (2005).

27. Harding, M. M. The geometry of metal–ligand interactions relevant to proteins. *Acta Crystallogr. D Biol. Crystallogr.* **55**, 1432–1443 (1999).

28. Harding, M. M. The geometry of metal–ligand interactions relevant to proteins. II. Angles at the metal atom, additional weak metal–donor interactions. *Acta Crystallogr. D Biol. Crystallogr.* **56**, 857–867 (2000).

29. Elinder, F. & Århem, P. Metal ion effects on ion channel gating. *Q. Rev. Biophys.* **36**, 373–427 (2003).

30. Corry, B., Allen, T. W., Kuyucak, S. & Chung, S.-H. Mechanisms of Permeation and Selectivity in Calcium Channels. *Biophys. J.* **80**, 195–214 (2001).

31. Hess, P. & Tsien, R. W. Mechanism of ion permeation through calcium channels. *Nature* **309**, 453–456 (1984).

32. Sather, W. A. & McCleskey, E. W. Permeation and Selectivity in Calcium Channels. *Annu. Rev. Physiol.* **65**, 133–159 (2003).

33. Almers, W., McCleskey, E. W. & Palade, P. T. A non-selective cation conductance in frog muscle membrane blocked by micromolar external calcium ions. *J. Physiol.* **353**, 565–583 (1984).

34. Cibulsky, S. M. & Sather, W. A. The Eeee Locus Is the Sole High-Affinity Ca^{2+} Binding Structure in the Pore of a Voltage-Gated Ca^{2+} Channel: Block by Ca^{2+} Entering from the Intracellular Pore Entrance. *J. Gen. Physiol.* **116**, 349–362 (2000).

35. Hille, B. *Ion Channels of Excitable Membranes*. (Sinauer Assoc, Sunderland, Mass, 2001).

36. Watson, J. L. *et al.* De novo design of protein structure and function with RFdiffusion. *Nature* **620**, 1089–1100 (2023).

37. Dauparas, J. *et al.* Robust deep learning–based protein sequence design using ProteinMPNN. *Science* **378**, 49–56 (2022).

38. Jumper, J. *et al.* Highly accurate protein structure prediction with AlphaFold. *Nature* **596**, 583–589 (2021).

39. Magnus, C. J. *et al.* Chemical and Genetic Engineering of Selective Ion Channel–Ligand Interactions. *Science* **333**, 1292–1296 (2011).

40. Wu, Z. *et al.* A sensitive GRAB sensor for detecting extracellular ATP in vitro and in vivo. *Neuron* **110**, 770-782.e5 (2022).

41. Zhu, Y. *et al.* A chemogenetic screen reveals that Trpv1-expressing neurons control regulatory T cells in the gut. *Science* **385**, eadk1679 (2024).

42. Sharpe, H. J., Stevens, T. J. & Munro, S. A Comprehensive Comparison of Transmembrane Domains Reveals Organelle-Specific Properties. *Cell* **142**, 158–169 (2010).

43. Levental, I. & Lyman, E. Regulation of membrane protein structure and function by their lipid nano-environment. *Nat. Rev. Mol. Cell Biol.* **24**, 107–122 (2023).

44. Dauparas, J. *et al.* Atomic context-conditioned protein sequence design using LigandMPNN. 2023.12.22.573103 Preprint at https://doi.org/10.1101/2023.12.22.573103 (2023).

45. Abramson, J. *et al.* Accurate structure prediction of biomolecular interactions with AlphaFold 3. *Nature* **630**, 493–500 (2024).

46. Feldman, D. *et al.* Optical Pooled Screens in Human Cells. *Cell* **179**, 787-799.e17 (2019).

47. Jiang, D., Gamal El-Din, T., Zheng, N. & Catterall, W. A. Chapter Five - Expression and purification of the cardiac sodium channel NaV1.5 for cryo-EM structure determination. in *Methods in Enzymology* (eds. Minor, D. L. & Colecraft, H. M.) vol. 653 89–101 (Academic Press, 2021).

48. Jiang, D. *et al.* Open-state structure and pore gating mechanism of the cardiac sodium channel. *Cell* **184**, 5151-5162.e11 (2021).

49. Jiang, D. *et al.* Structure of the Cardiac Sodium Channel. *Cell* **180**, 122-134.e10 (2020).

50. Lenaeus, M., Gamal El-Din, T. M., Tonggu, L., Zheng, N. & Catterall, W. A. Structural basis for inhibition of the cardiac sodium channel by the atypical antiarrhythmic drug ranolazine. *Nat. Cardiovasc. Res.* **2**, 587–594 (2023).

51. Tonggu, L. *et al.* Dual receptor-sites reveal the structural basis for hyperactivation of sodium channels by poison-dart toxin batrachotoxin. *Nat. Commun.* **15**, 2306 (2024).

52. Croll, T. I. ISOLDE: a physically realistic environment for model building into low-resolution electron-density maps. *Acta Crystallogr. Sect. Struct. Biol.* **74**, 519–530 (2018).

53. Emsley, P. & Cowtan, K. Coot: model-building tools for molecular graphics. *Acta Crystallogr. D Biol. Crystallogr.* **60**, 2126–2132 (2004).

54. Liebschner, D. *et al.* Macromolecular structure determination using X-rays, neutrons and electrons: recent developments in Phenix. *Acta Crystallogr. Sect. Struct. Biol.* **75**, 861–877 (2019).

55. Williams, C. J. *et al.* MolProbity: More and better reference data for improved all-atom structure validation. *Protein Sci.* **27**, 293–315 (2018).

56. Wu, J. *et al.* Structure of the voltage-gated calcium channel Cav1.1 at 3.6 Å resolution. *Nature* **537**, 191–196 (2016).

57. Saotome, K., Singh, A. K., Yelshanskaya, M. V. & Sobolevsky, A. I. Crystal structure of the epithelial calcium channel TRPV6. *Nature* **534**, 506–511 (2016).

58. Hou, X., Outhwaite, I. R., Pedi, L. & Long, S. B. Cryo-EM structure of the calcium release-activated calcium channel Orai in an open conformation. *eLife* **9**, e62772 (2020).

59. Zhu, W., Shenoy, A., Kundrotas, P. & Elofsson, A. Evaluation of AlphaFold-Multimer prediction on multi-chain protein complexes. *Bioinformatics* **39**, btad424 (2023).

60. Grynkiewicz, G., Poenie, M. & Tsien, R. Y. A new generation of Ca^{2+} indicators with greatly improved fluorescence properties. *J. Biol. Chem.* **260**, 3440–3450 (1985).

61. Chin, D. & Means, A. R. Calmodulin: a prototypical calcium sensor. *Trends Cell Biol.* **10**, 322–328 (2000).

62. Kirichok, Y., Krapivinsky, G. & Clapham, D. E. The mitochondrial calcium uniporter is a highly selective ion channel. *Nature* **427**, 360–364 (2004).

63. Voltage-gated calcium channels: direct observation of the anomalous mole fraction effect at the single-channel level. https://www.pnas.org/doi/10.1073/pnas.86.13.5207 doi:10.1073/pnas.86.13.5207.

64. Gillespie, D. & Boda, D. The Anomalous Mole Fraction Effect in Calcium Channels: A Measure of Preferential Selectivity. *Biophys. J.* **95**, 2658–2672 (2008).

65. Nonner, W., Chen, D. P. & Eisenberg, B. Anomalous Mole Fraction Effect, Electrostatics, and Binding in Ionic Channels. *Biophys. J.* **74**, 2327–2334 (1998).

66. Prakriya, M. & Lewis, R. S. Separation and Characterization of Currents through Store-operated CRAC Channels and Mg^{2+}-inhibited Cation (MIC) Channels. *J. Gen. Physiol.* **119**, 487–508 (2002).

67. Mishra, R., Rao, V., Ta, R., Shobeiri, N. & Hill, C. E. Mg^{2+}- and MgATP-inhibited and Ca^{2+}/calmodulin-sensitive TRPM7-like current in hepatoma and hepatocytes. *Am. J. Physiol.-Gastrointest. Liver Physiol.* **297**, G687–G694 (2009).

68. Jin, J. *et al.* Deletion of Trpm7 Disrupts Embryonic Development and Thymopoiesis Without Altering Mg^{2+} Homeostasis. *Science* **322**, 756–760 (2008).

69. Lansman, J. B., Hess, P. & Tsien, R. W. Blockade of current through single calcium channels by Cd^{2+}, Mg^{2+}, and Ca^{2+}. Voltage and concentration dependence of calcium entry into the pore. *J. Gen. Physiol.* **88**, 321–347 (1986).

70. Bers, D. M., Patton, C. W. & Nuccitelli, R. A Practical Guide to the Preparation of Ca^{2+} Buffers. in *Methods in Cell Biology* (ed. Whitaker, M.) vol. 99 1–26 (Academic Press, 2010).

71. Voets, T. *et al.* CaT1 and the Calcium Release-activated Calcium Channel Manifest Distinct Pore Properties*. *J. Biol. Chem.* **276**, 47767–47770 (2001).

72. Yue, L., Peng, J.-B., Hediger, M. A. & Clapham, D. E. CaT1 manifests the pore properties of the calcium-release-activated calcium channel. *Nature* **410**, 705–709 (2001).

73. McNally, B. A., Somasundaram, A., Yamashita, M. & Prakriya, M. Gated regulation of CRAC channel ion selectivity by STIM1. *Nature* **482**, 241–245 (2012).

74. Prakriya, M. The molecular physiology of CRAC channels. *Immunol. Rev.* **231**, 88–98 (2009).

75. Hoth, M. & Penner, R. Depletion of intracellular calcium stores activates a calcium current in mast cells. *Nature* **355**, 353–356 (1992).

76. Tang, L. *et al.* Structural basis for inhibition of a voltage-gated Ca^{2+} channel by Ca^{2+} antagonist drugs. *Nature* **537**, 117–121 (2016).

77. Hou, X., Burstein, S. R. & Long, S. B. Structures reveal opening of the store-operated calcium channel Orai. *eLife* **7**, e36758 (2018).

78. Zhang, K., Wu, H., Hoppe, N., Manglik, A. & Cheng, Y. Fusion protein strategies for cryo-EM study of G protein-coupled receptors. *Nat. Commun.* **13**, 4366 (2022).

79. Brunette, T. J. *et al.* Exploring the repeat protein universe through computational protein design. *Nature* **528**, 580–584 (2015).

80. Drożdżyk, K. *et al.* Cryo-EM structures and functional properties of CALHM channels of the human placenta. *eLife* **9**, e55853 (2020).

81. Demura, K. *et al.* Cryo-EM structures of calcium homeostasis modulator channels in diverse oligomeric assemblies. *Sci. Adv.* **6**, eaba8105 (2020).